Dynamics and Performance of Tethered Airborne Wind Energy Systems

Amar Fayyad K. Akberali

A Thesis
in
The Department
of
Mechanical, Industrial and Aerospace Engineering

Presented in Partial Fulfillment of the Requirements
For the Degree of Master of Applied Science (Mechanical Engineering)
Concordia University
Montréal, Québec, Canada

November 2022

CONCORDIA UNIVERSITY

School of Graduate Studies

This is to certify that the thesis prepared

By: **Amar Fayyad K. Akberali**

Entitled: **Dynamics and Performance of Tethered Airborne Wind Energy Systems**

and submitted in partial fulfillment of the requirements for the degree of

Master of Applied Science (Mechanical Engineering)

complies with the regulations of this University and meets the accepted standards with respect to originality and quality.

Signed by the final examining committee:

____________________________ Dr. Marius Paraschivoiu, Chair and Internal Examiner

____________________________ Dr. Theodore Stathopoulos, External Examiner

____________________________ Dr. Mojtaba Kheiri, Supervisor

Approved by ____

Dr. Martin D. Pugh, Chair

Department of Mechanical, Industrial and Aerospace Engineering

_________ 2022 ____

Dr. Mourad Debbabi, Dean

Gina Cody School of Engineering and Computer Science

Abstract

Dynamics and Performance of Tethered Airborne Wind Energy Systems

Amar Fayyad K. Akberali

This research work presents the dynamics and performance of tethered airborne wind energy systems. To this end, aerodynamic theories for crosswind kite power systems (CKPSs) and an aerostatic power system (APS) have been developed along with the tether models for the respective systems. Two semi-analytical aerodynamic models based on the blade element momentum (BEM) theory considering the effects of induction factor, reel-out ratio, solidity factor, rotor incidence angle, side slip and tether drag are developed for CKPSs. Aerodynamic model 1 is for lift mode CKPSs while Aerodynamic model 2 is for lift mode or drag mode CKPSs or a combination of both. Verification and parametric studies proved the accuracy of the models and gave insights into the combined effects of the operational and geometric parameters. In addition, a semi-analytical aerodynamic model is developed to predict the quasi-steady aerodynamic performance of APS using BEM considerations. The theory which assumes a variable inflow is validated against an autogyro and yawed wind turbine. Variation of aerodynamic performance parameters and optimum rotational speed for the rotor of a 300 kW APS is studied. Moreover, two tether models based on lumped mass modelling approach, one rigid and the other elastic, accounting for reel-in/reel-out had been developed to analyze the coupled dynamics of the tether and airborne modules. The results from the elastic and rigid tether models for a kite power system and an APS show the shortcomings and advantages of one model over the other.

Acknowledgments

The title page mentions one author but this work had been the effort of many. This chapter would become the longest among all if I had to mention everyone I owe. However, I would like to acknowledge of few of them. I would like to express my sincere gratitude to Dr Mojtaba Kheiri who understood my motivation and offered me a research position. The trust he placed and the opportunity he presented had been a source of encouragement throughout the work. I am eternally grateful for his support and guidance at professional and personal levels. I am also thankful to all the teaching and non-teaching staff at Concordia University who have helped me during this thesis. Special thanks to Dr Frédéric Bourgault for his guidance throughout my internship at New Leaf Leaf Management Ltd., Mr Samson Victor for the CFD simulations and my friend Mahdi Riazat who had been available to help with my doubts. It goes without saying that, how much I would like to appreciate the funding received from NSERC, Concordia University, New Leaf Management Ltd and Mitacs. I would also like to thank the two selfless souls who unconditionally supported me through this journey, my wife Farhana P.K and my dad Akberali K.M. Without their kindness even being in Canada might have been a dream. This page will be incomplete if I don't mention my friends Vijesh, Aswathy, Kp, Nithya, Levy, Akhil, Kavya, Rosh, Bibin, Nancy, Sujith, Akash, Abhinand, Vineeth, Arunjith, Rishin among others and the adventures we had which helped me to stay positive and think straight. Thank God I had all of you!

Contents

List of Figures

List of Tables

Chapter 1

Introduction

1.1 Background

There has been an ever-increasing demand for energy in the past few decades to satisfy human needs. For sustainable growth, it is important to replace the non-renewable sources of energy which caters to most energy requirement at present with renewable sources. The unequal concentration of resources required for producing non-renewable energy also caused an energy crisis in certain parts of the world in the past decades.

This background leads to increased research and development of renewable sources of energy. Several advancements have been made in solar energy, wind energy and geothermal energy among others in the last few decades. One of the prominent ideas in wind energy is airborne wind energy (AWE).

Miles Loyd proposed the idea of harvesting energy from high altitudes using the tethered airborne module [10]. Numerous types of airborne wind energy systems (AWES) have been proposed since then. Each of these systems has its airborne module connected to the ground via a tether. The electricity is either generated on-board by converting wind energy into mechanical energy and transmitted to the ground via the tether or the motion of the airborne module is transmitted mechanically via the tether to generate electricity at the ground. Airborne wind energy (AWE) which concerns accessing and harnessing high-altitude wind energy via either stationary or flying devices may be considered as the most recent, active research and technological innovation in the wind energy industry [11]. In fact, AWE is considered as one of “100 radical innovation breakthroughs for the future” according to a recent report prepared by the European Commission [12].

The central premise of AWE, which makes it competitive with the existing wind energy technologies, is to produce more energy using significantly less amount of material (or mass); for example, Diehl [13] projected that a single 30 MW AWE system could be approximately 300 times lighter than four 7.5 MW wind turbines combined. Although such an amount of mass saving may seem highly optimistic, mass savings of approximately 90% may be attainable [14]. This is achieved by reaching higher altitudes of above 1300 m [15], where winds are naturally stronger (because of the well-known logarithmic velocity profile within the earth's boundary layer) and steadier, via very light structures, such as high-molecular-density synthetic tethers (instead of very heavy towers used in conventional wind turbines). Today, there are dozens of enterprises and research institutions around the world, which are pursuing a variety of AWE concepts, such as aerostatic systems, inflatable soft kites, and aeroplane-like rigid kites; please refer to Ref. [7] for a list of the AWE major players; also, see Ref. [16] for a review of AWE technologies. These concepts normally differ in how they extract wind power and how they are deployed and retracted.

Crosswind kite power systems (CKPSs) are a type of AWE system, where one or multiple tethered wings (or kites) fly trajectories which for most part are oriented perpendicularly to the oncoming wind. Compared to non-flying AWE systems, crosswind systems have the advantage of producing much larger aerodynamic forces (and thus much more power) due

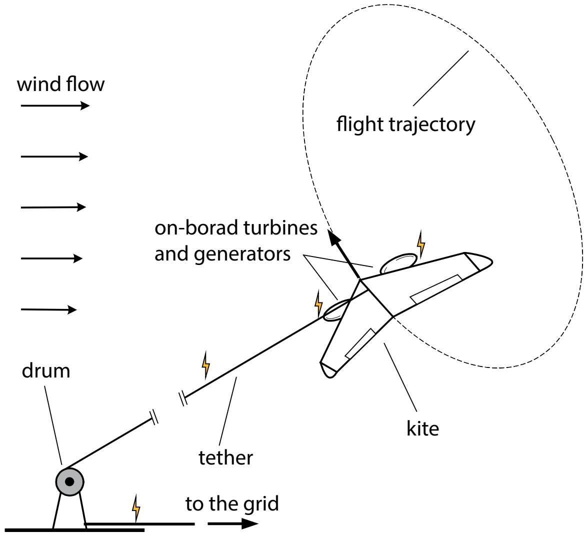

Figure 1.1: A schematic drawing showing the drag mode or on-board power generation. The image was reproduced from Ref. [1].

to the fact that they can fly crosswind at many times the wind speed. Another advantage of CKPSs is that they can sweep a very large area in the sky compared to aerostatic and non-flying traction systems which harness wind energy from a very limited projected area. These two advantages make CKPSs very attractive compared to other AWE concepts. Nevertheless, high-speed flying kite systems come at the cost of being, in principle, more complex, perhaps, more costly and less reliable. Thus, what makes a concept eventually superior is having a lower levelized cost of energy.

One way of classifying different AWESs, and particularly CKPSs, is through the way they generate power – the power generation mode. The two main classes are (1) ground-based (or pumping-mode) power generation, and (2) on-board power generation. This type of classification was made by Loyd [10] for the first time, who proposed the crosswind kite power concept and also coined the words ‘drag mode’ (Figure 1.1) and ‘lift mode’ (Figure 1.2) and for the on-board generation and ground-based, respectively. Today, there are several

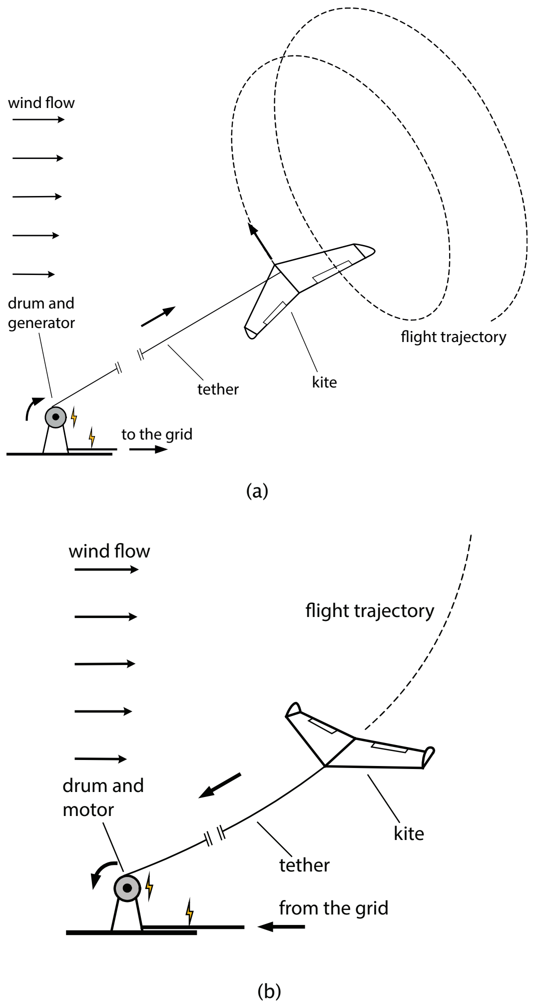

Figure 1.2: Schematic drawings showing the lift mode or ground-based power generation: (a) reel-out or power generation phase, and (b) reel in or power consumption phase. The images were reproduced from Ref. [1].

companies, such as Makani (Figure 1.3)[1] Windlift, and KiteX are pursuing the on-board generation concept while others, such as Ampyx Power, Twingtec and Kitemill (Figure 1.4) are seeking ground-based generation. Like the wind turbines, the operational altitude of these prototypes are within earth's atmospheric boundary layer and can vary between 150 m to 1300 m [2, 17]. of these Loyd [10] theoretically showed that the two power generation modes are equivalent in terms of power output although some recent studies indicate the

---

[1] This Google X project was discontinued in September 2020.

Figure 1.3: Figure showing the drag mode kite Makani M600. The image was reproduced from Ref. [2].

Figure 1.4: Figure showing the lift mode kite from Kitemill. The image was reproduced from Ref. [3].

superiority of one or the other; for example, see Refs. [1, 18]. The two modes are different in the way they harness wind power: in the ground-based generation, strong tether tension (produced as a result of aerodynamic forces acting on the kite) is transferred to the ground, which is usually used to spin a drum (and a generator) by unrolling the tether; in the on-board generation, on the other hand, electricity is generated on-board via turbines mounted on the flying kite and is transmitted to the ground via a conductive tether. The two modes thus differ over several practical aspects, such as hardware, systems, and mechanisms. After all, it is still unclear which one of the two modes of power generation would be superior in practice.

Aerostatic power systems (APSs) shown in Figure 1.5 are tethered statically suspended AWESs with rotating wings like an autogyro proposed by Roberts et al. [19]. The high speed and persistent upper atmospheric winds often called jet streams are attractive to researchers in wind energy. Extending for thousands of meters, they have velocities of up to 500 km/h at their centres. However, this speed reduces radially from the core [20]. To utilise of wind of such high power density, a suitable AWES has to be carefully placed and APS is one of the most promising concepts. For an APS, since the tether and the airborne module are not flying (not moving around in the air), the system is relatively dynamically stable and has the

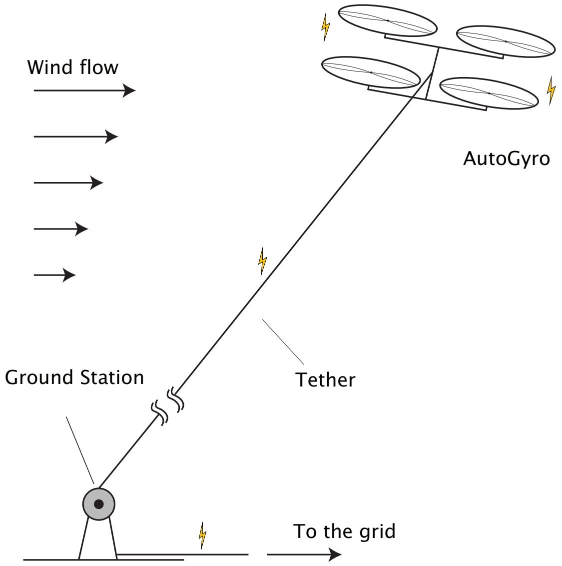

Figure 1.5: Figure showing the aerostatic power system (APS).

advantage to operate safely at higher altitudes with longer tethers. The lack of reel-in/reel-out dynamics and crosswind motion reduces fatigue on the system and vibrations associated with the change of acceleration during the transition from reel-in to reel-out and vice versa. These aspects make APSs an attractive reliable AWE concept.

The APS generally contain an even number of rotors with some or all pairs executing counter-rotation to balance the torque. The rotors mounted on the airframe are coupled with generators to generate electricity onboard, which is then transmitted to the ground via a tether. To the author's best knowledge, the only companies pursuing this idea are Sky Windpower shown in Figure 1.6 and Velocity Cubed [21].

Any airborne wind energy system (AWES) is essentially composed of (i) an airborne module, (ii) a tether, and (iii) a base station. The generation system can be on-board or on the ground. In either case, the tether mechanically holds the airborne module in the desired place so that it does not drift away with the wind. It also mechanically transmits power to the ground for a ground-based generation. The tether being a flexible member is prone to vibrations which can be from the overall dynamics of the system or can be flow-induced.

Figure 1.6: Figure showing the APS from Sky Windpower. The image was reproduced from Ref. [4].

The tether in AWESs is very flexible/elastic as its typical diameter is only a few millimetres while it has a length of a few hundred meters. This makes the tether prone to vibrations in transverse and longitudinal directions during the operation of AWES, which can cause fatigue damage, wear and even potentially lead to a catastrophic failure. Under tension, the tether acts like a rod in tension and it will not take the compressive load. This results in cases of sudden re-tensioning of the tether after zero tension during operations leading to snap loads. The snap loads can be detrimental to the tether as well as to the airborne module and the base station [22]. In short, it is important to understand and predict the behaviour of tether dynamics to overcome the major barrier in AWE, which is reliability [23].

The AWES in which the dynamics of the airborne module is coupled with that of the tether and the base station pose several open questions in aerodynamics, structural dynamics, optimization and control systems. The crosswind motion makes the crosswind kite power system (CKPS) [11] attractive for lower altitudes and the aerostatic nature makes an autogyro-like aerostatic power system (APS) [19] is compelling for a higher altitude. An accurate analytical aerodynamic theory is needed to carry out parametric studies in the preliminary design phase. A robust tether dynamic model is required to predict the complex dynamics of the overall system in real-time.

1.2 Motivation

Horizontal axis wind turbines (HAWTs) and vertical axis wind turbines (VAWTs) are the predominant technologies used for wind energy extraction. In the past few decades, the rated power of these devices has gone up which resulted in larger diameter rotors and taller towers. The wind power is proportional to the cube (the third power) of the freestream velocity and a taller tower provides access to the more consistent and higher velocity at higher altitudes. The increased rotor diameter improves the tip speed as well as tap energy from a much larger area. However, wind turbines may be limited to a few hundred meters of height due to the requirement of long tower and blades which will make them not practical due to manufacturing constraints and high cost. This means much of the available wind energy remains not utilised.

However, a tethered kite is not limited by the requirement of a tower or larger blades, e.g. CKPS, to reach higher altitudes and to tap energy from a larger area. The AWESs have the potential to be cheaper, lighter and easier to set up when compared to conventional wind turbines. For these reasons, it seems like a promising technological transition for wind energy devices.

1.3 Objectives

The main objective of this research work is to develop robust aerodynamic and tether dynamic models for the CKPS and APS. The goals are achieved in the steps described below.

1. Develop a steady-state aerodynamic theory for the CKPS.
2. Develop a quasi-steady aerodynamic theory for the APS.
3. Develop a dynamic tether model capable of accounting for reel-in/reel-out motion.
4. Analyse the stability and dynamics of the coupled system composed of the tether and airborne module.

1.4 Literature Review

1.4.1 Crosswind kite power system

Although AWE is a relatively new field for research, the body of literature on some subjects, such as trajectory optimization and control is already extensive; some examples are [24–26] with some recent ones, such as [27–29]. This is, however, not true for other subjects, such as aerodynamic performance analysis of single or multiple kites, which has remained underdeveloped virtually since Loyd's [10] original contribution. Most studies either explicitly or implicitly neglected interactions between a kite flying crosswind and the wind flow as well as the aerodynamic interactions between multiple kites in a kite farm. More precisely, they neglected the kite induction (or interference) factor and the wake flow dynamics. This is due to the general perception that the kite would sweep an infinitely large area in the sky and thus it would disturb the flow imperceptibly; please refer to Ref. [30] for more details.

However, neglecting the aerodynamic interactions has some important implications, one of which, as shown, for example, by Zanon et al. [31] and Kheiri et al. [30], is the overestimation of the power output or the energy harvesting efficiency. Some recent studies, such as Refs. [18, 32–34] have taken into account the effects of the kite induction. More studies appeared recently, where the effects of the induction factor on the aerodynamic performance of AWE systems have been incorporated. Pfister et al. [35] compared thrust and power coefficients obtained from the blade element momentum (BEM) theory with those from the free vortex model for an inclined/yawed tethered rotorcraft. They showed that the results from the BEM model with numerical integration and tabulated aerodynamic coefficients are in "reasonably good agreement" with those from the vortex model. Gaunaa et al. [36] used the vortex theory to obtain the induction factor for a CKPS. The circulation distribution and thus the wing planform was assumed to be elliptical. They showed that the induction factor values are overpredicted by the classic momentum model compared to the vortex model. However, the results for the axial force (which is the driving force for power generation in the ground-based generation mode) from the two models were found to be in a generally good agreement with each other and with those from the actuator line-based CFD simulations for a wide range of the kite-to-wind speed ratio and several values of the kite-span-to-gyration-radius ratio.

Moreover, some studies have attempted to examine wake flow of a single or multiple kites. Some notable computational studies are those by Haas et al. [37], Kheiri et al. [38], Kheiri et al. [39], Haas et al. [33], and Haas et al. [40]. These studies employed Reynolds-Averaged Navier-Stokes and Large-Eddy Simulation flow solvers and showed how the shape and the velocity of the wake changes as a function of the downstream distance from the kites. Most recently, two analytical models, one by Kaufman-Martin et al. [41] and one by Karakouzian et al. [42], have also been developed. These models were developed based on mass and momentum conservation equations, and using them one can quickly obtain the shape and the velocity of the wake. Such models are instrumental in designing and optimising kite farms since they can provide power output estimation also including kite-kite aerodynamic interactions.

1.4.2 Aerostatic power system

Compared to CKPS, the amount of literature on APS is small because of the potential of CKPSs for harvesting lower-altitude wind energy. Most works on APS focus on modelling the steady-state aerodynamics of the rotor, statics of the rotor coupled with that of the tether and system-level studies; some examples are Refs. [19, 21, 43, 44]. To the best of the author's knowledge, the dynamic models in the existing literature consider a single-element tether model while ignoring the actual geometry of the airfoil.

Roberts et al. [19] may be the first to propose the idea of using an APS for harnessing high-altitude winds. The steady-state aerodynamics, electrics, control of the APS while describing the tether dynamics and energy storage is presented in [43]. Even though a steady-state aerodynamic model based on the blade element momentum (BEM) theory is sufficient for preliminary performance calculations, it cannot be employed for the dynamic analysis of the APS. The aerodynamic theory also ignores the actual geometry of the airfoil by approximating the force coefficients. The steady-state BEM presented assumes a uniform inflow and also is not suitable for accommodating a wind profile. The validation of the aerodynamic theory is presented in [19], and even though the analytical results are in agreement with the experiment at high tip speed ratios, the results deviates at low tip speed ratios where the flow is highly turbulent and features separation. The tether dynamics is briefly described but the dynamical equations and analysis is not presented.

Rong et al. [44] presented results for a tethered yawed wind turbine which is essentially an APS in its energy harvesting mode. The paper obtained the optimum operating parameters of the system using momentum theory. However, like Roberts et al. [43], the paper assumes steady-state aerodynamic theory with uniform inflow ignoring the airfoil geometry thus making it unfit for a sheared wind profile or dynamic model of APS. An attempt was made to consider tether weight to estimate optimum operational conditions at the preliminary level but it is insufficient for dynamic analysis.

Rancourt et al. [21] performed a design space exploration and optimisation of the APS and provided guidelines for the future development of the concept. This could also be considered as the first paper to study the concept at a system level. The rotor aerodynamics is modelled using AeroDyn from National Renewable Energy Laboratory (NREL), and the static analysis of the APS is presented considering the rigid tether. The focus of the paper remains on the system-level study at steady state conditions, and dynamic analysis of the system is missing. Even though verification of the aerodynamic package was presented, validation for operational conditions of APS was not presented. The aerodynamic model implemented for the analysis is quasi-steady. The rigid tether model used in the study neglects the tether extension and thus the extra height and the higher wind velocity that could have been accessed by the APS.

1.4.3 Tether modelling

A number of works have been done on tether modelling, some even considering all the major aspects, such as Refs. [24, 26, 45–47], among others. However, the existing models are mostly being used for optimization and control purposes rather than dynamic and aeroelastic stability analyses. Most studies employ a lumped mass model (LMM) where the tether is modelled as a series of point/lumped masses that are connected by mass-less links. The links can be assumed to be rigid or elastic using linear springs and dampers. LMM has been widely used in AWES modelling and space elevator concepts [48]. Most works in the existing literature do not consider or give secondary importance to vibration studies. The experiments conducted by Dunker [49] suggested that lock-in and galloping can occur in static tethers and lock-in may be relevant in moving tethers. Modelling of aerodynamic forces on tether also needs some improvements. Most studies have neglected the forces altogether or only considered the forces acting normal to the tether. The aerodynamic force in the tangential direction and apparent mass effects were neglected altogether.

Williams et al. [50] presented the modelling of a tethered crosswind kite system using the LMM, where the tether is considered to be rigid. The tether modelling is done in the Newtonian framework resulting in constraint forces. The reel-in/reel-out is facilitated by adding and removing elements. The tether drag in the normal and tangential directions is modelled in this work. The focus of the research remained on the analysis of the controller designed for the crosswind kite to maintain tension at the desired level. The verification/validation of the tether model was not presented and the dynamic analysis of the system from an aeroelastic perspective is also missing. The paper also presented only a rigid tether model and thus longitudinal vibrations and effects of elasticity were neglected. A rigid tether model will fail to capture the high-frequency oscillations which could be a major cause of fatigue and the snap loads from longitudinal vibrations.

Milutinović et al. [46] introduced the modelling of a tethered rotating cylindrical balloon that produces lift by the Magnus effect employing the lumped mass model (LMM). The tether was modelled as elastic by considering a linear spring and damper in each element. In contrast to most models, the dynamics of the winch is incorporated into the modelling. The reel-in/reel-out was modelled by adding and removing elements similar to Williams et al.[24]. The reason for the choice of a much more complex elastic tether model over the rigid tether model is not presented. Even though verification of the static shape is presented, an attempt to verify/validate the dynamics of the tether is missing. To avoid compressive loading, the tether is assumed to be rigid during negative extensions. This will introduce anomalies in the prediction of dynamics.

Fechner et al. [47] propose a modelling framework for tethered pumping kite employing LMM. The elastic tether is modelled using linear springs and linear dampers and the reel-in/reel-out is modelled by dynamically changing the tether length. The kite has been modelled in two ways: one using a point mass model and the other using a four-point mass model. The dynamics of the ground station is also included. The reel-in/reel-out implemented through the quasi-steady approach underpredicts the kinetic energy from the reel-out. Even though this is a simpler algorithm for reel-in/reel-out, a verification/validation with the dynamical reel-in/reel-out models/measured data is required to justify the adaptation of this method. The non-physical variable damping coefficient dependent on tether length might underpredict the dynamics. The wind gradient for the kite system is modelled using power law and incorporates turbulence. It is observed that the wind turbulence did not significantly affect the annual energy production of the investigated system [51]. The focus of the work has been on developing a framework suitable for an optimum control system and thus ignores aeroelastic and vibration analysis.

Sánchez-Arriaga and his colleagues have published many works on tether modelling of kites. Sánchez et al. [52] present modelling and stability analysis of a tethered kite. The rigid tether model presented is modelled as a series of N-Bars like in LMM and a continuous elastic model is also introduced. The kite neither harvests wind energy nor does reel-in/reel-out. Sánchez et al. [29] performed the dynamic modelling and analysis of tethered AWESs operating in pumping and drag modes. The tether was modelled as a series of rigid rods, and the reel-in/reel-out was modelled by dynamically changing the tether length. In [53], Sánchez et al. introduced two models for the dynamic analysis of AWESs based on a multi-aircraft configuration. The first model approximates the tethers involved to be massless, inelastic, straight and of constant length. The aerodynamic drag acting on the tether is neglected. In the second model, the tether is assumed to be elastic, has inertia, has aerodynamic drag effects and follows the LMM approach for modelling.

Sánchez-Arriaga and his colleagues have extensively contributed to the rigid and elastic tether modelling while including kite dynamics at different levels of complexity. However, to the best of the author's knowledge, a systematic comparison between rigid and elastic tether models for both statically suspended systems and systems undergoing reel-in/reel-out is yet to be done. The statics and dynamics of the tether have to be verified/validated for both of these approaches. The comparison of models while treating the rigid models to be massless and without aerodynamic drag also makes it difficult to understand the contribution of elasticity. Although extensive research has produced robust models for control systems, a systematic study to address aeroelastic vibrations is still missing.

1.5 Main contributions

The main contributions of this thesis are (i) two simplified steady-state aerodynamic theories accounting for induction which are instrumental for design and optimization of CKPSs, (ii) a quasi-steady aerodynamic theory to analyze the dynamics and performance of tethered APS and (iii) a comparative study about the short comings and advantages of the rigid and elastic tether models for statically suspended and reel-in/reel-out AWESs. The main research results were summarised in the following publications.

Journal paper:

- K. Akberali, A. F., Kheiri, M., Bourgault, F. (2021). Generalized aerodynamic models for Crosswind Kite Power Systems. Journal of Wind Engineering and Industrial Aerodynamics, 215, 104664. https://doi.org/10.1016/j.jweia.2021.104664.

Conference poster:

- K. Akberali, A. F., Kheiri, M., Bourgault, F. (2022). Dynamics of tethered airborne wind energy systems, AWEC 2021, June 2022, Milan, Italy.

Conference paper:

- K. Akberali, A. F., Kheiri, M., Bourgault, F. (2021). Dynamics of a tethered kite used for harnessing high-altitude winds, AERO 2021- CASI (virtual event).

Working paper:

- K. Akberali, A. F., Kheiri, M., Bourgault, F. (2023). Dynamics of tethered aerostatic and kite power systems.

1.6 Road map

This section explains in brief how the thesis is structured. In addition to this introductory chapter, there are four other chapters in this thesis. In Chapter 2, the two steady-state aerodynamic models developed for the crosswind kite power system are explained. Chapter 3 presents the quasi-steady aerodynamic theory for the APS. The modelling and the results from rigid as well as elastic tether models coupled with the outputs of the aerodynamic models of a kite power system (KPS) and APS are presented in Chapter 4. Chapter 5 presents the concluding remarks and suggests future works.

Chapter 2

Generalized aerodynamic models for crosswind kite power systems

This chapter presents two novel semi-analytical models for predicting the aerodynamic performance of crosswind kite power systems (CKPSs), where the kite induction effects on the oncoming flow are taken into account. The blade element momentum theory forms the backbone of the models. The effects of reel-out ratio, solidity factor, rotor incidence angle, side-slip angle and tether drag are included in the formulation for the axial induction factor and power output. For simplicity, the wake rotation and the tangential induction factor are neglected. Aerodynamic model 1 is developed for predicting the reel-out power with uniform inflow assumption, and it is suitable for CKPSs with ground-based power generation. Aerodynamic model 2, on the other hand, can predict both the reel-out and torque powers with either uniform or non-uniform inflow assumption, and the model can be used for CKPSs with ground-based, or on-board power generation, or with the combination of the two. Some parametric studies have been conducted for a generic kite system with predefined aerodynamic efficiency parameters to highlight the effects of incidence and side-slip angles. In addition, a particular CKPS and its variants are examined to show the individual and combined effects of incidence angle, side-slip angle, tether drag and airfoil shape on the induction factor and power output.

2.1 Definitions and preliminaries

The system under consideration is a rigid wing which rotates about a fixed point in space, as shown in Figure 2.1.[1] The wing may also reel-out while rotating. The imaginary axis that passes through this point and is perpendicular to the plane of rotation will be referred to as the rotation axis. The area swept by the kite, that lies on the plane of rotation, would be annulus in shape. The pressure side of the wing will face the wind flow. The position of the kite in space can be fixed in the spherical coordinate system as shown in Figure 2.1. The freestream velocity, V_∞, is assumed to be uniform in space and time and to be in the X-direction; the rotation plane has an angle β with respect to the X-axis, which is commonly called the side-slip angle, and an inclination of i with respect to the Z-axis, known as the incidence angle (which is complementary to the elevation angle defined as the angle between the rotation axis and the ground surface). The relative wind speed vector at the centre of the rotation plane thus becomes

$$W = \big(V_\infty \sin i \cos\beta - v - V_d\big)\hat{e}_r + \big(V_\infty \cos i \cos\beta\big)\hat{e}_i - V_\infty \sin\beta \hat{e}_\beta, \tag{2.1}$$

where $\hat{e}_r$, $\hat{e}_i$, and $\hat{e}_\beta$ are, respectively, the unit vectors in the spherical coordinate system (r, i, β); v is the induced flow velocity perpendicular to the plane of rotation, and V_d is the kite reel-out speed, which is in the same direction as $\hat{e}_r$.

---

[1] In the present paper, the words 'wing' and 'kite' are used interchangeably.

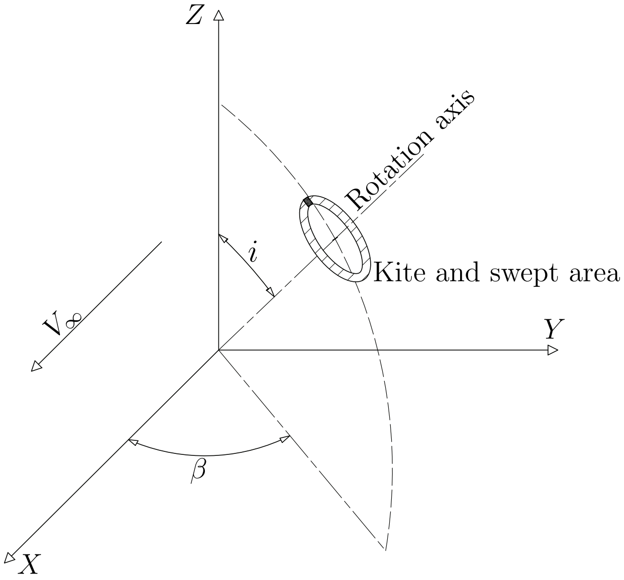

Figure 2.1: A schematic drawing representing a crosswind kite in the spherical coordinate system, where i and β are the incidence and side-slip angles, respectively; also, V_∞ is the undisturbed freestream/wind velocity.

2.2 Theory

Here, the performance and loading of CKPSs are obtained using the blade element momentum (BEM) theory, which, in principle, lets the axial force (i.e. the force normal to the rotation plane) and torque experienced by the flow in independent streamtubes, which are predicted by the momentum theory, equal to those experienced by the elements of the kite/wing, which are predicted by the blade element theory. The momentum theory is based on Newton's second law of motion and considers the thrust developed by the *actuator disc* to be equal to the rate of change of momentum of fluid particles passing through the disc. The blade element theory, on the other hand, formulates equations for the thrust and torque generated by the kite based on the strip flow theory which uses aerodynamic coefficients and the relative flow velocity at a finite number of elements along the span; for details regarding the momentum, blade element and BEM theories, the reader is referred to [54, 55].

2.2.1 Momentum considerations

The induced flow velocity perpendicular to the rotation plane (or the axial induced velocity), v, is often expressed in the dimensionless form when obtaining power and thrust for a wind energy extracting device. The dimensionless counterpart of v is called the induction or interference factor which, for example, for a conventional wind turbine is defined as $a = v/V_\infty$. Since a CKPS is normally inclined with respect to the freestream, and it may also reel-out while spiraling in the sky, an alternative definition for the induction factor may also be proposed as

$$\tilde{a} = \frac{v}{V_\infty \sin i \cos\beta - V_d} = \frac{a}{\sin i \cos\beta - e}, \tag{2.2}$$

where $V_\infty \sin i \cos\beta - V_d$ is the relative flow velocity normal to the rotation plane, $e = V_d/V_\infty$ being the ratio of the reel-out speed to the freestream velocity or the reel-out ratio, for short.

In the formulation presented in the main body of this paper, a and, in general, dimensionless variables that are obtained through normalization with respect to constant configuration-independent parameters, are used. A similar practice is commonly adopted for yawed wind turbines, where the axial induction factor is defined as the ratio of induced velocity (normal to the rotor plane) to the undisturbed freestream velocity; please see, for example, [54, 56–58]. Nevertheless, one may favour the use of alternative dimensionless variables, such as $\widetilde{a}$. Appendix A provides the key formulae of the paper expressed in terms of an alternative set of dimensionless variables.

From the momentum theory perspective, the axial induced flow velocity may be interpreted as the effect of the 'solidity' (i.e. the physical presence) of an actuator disc or energy extracting device on slowing down the oncoming fluid flow [54]. Thus, one may think of an energy device as an intermediate system between a fully permeable disc (when no induction is applied on the flow) and a complete blockage (when the induction is at maximum). This is actually the physical basis for experimental studies which use porous discs (usually built by assembling layers of metal mesh) to emulate the wake flow generated behind wind turbines; for example, see [59–62].

Glauert [63] proposed the following expression for obtaining v over the rotor area of an autogyro

$$v = \frac{T}{2\pi R^2 \rho_\infty V_{res}}, \tag{2.3}$$

where T is the thrust, R is the radius of the rotor (or disc), ρ_∞ is the airflow density, and V_{res} is the *resultant* flow velocity at the disc.

For a wind energy extracting device, such as a conventional wind turbine, with the rotor area of $A = \pi R^2$, and $V_{res} = V_\infty - v$, equation (2.3) may be rewritten as

$$T = 2\rho_\infty A v (V_\infty - v) = 2\dot{m} v, \tag{2.4}$$

that can be easily confirmed from the classical actuator disc theory; $\dot{m}$ being the mass flow rate through the disc.

On the other hand, if the rotor area is thought as a wing of the span $2R$ and the average chord length R (and thus the aspect ratio $= 2$ and planform area $S = 2R^2$) and assuming that the departure from the elliptical planform is negligible, then the induced angle of attack may be obtained as

$$\alpha_i = \frac{C_L}{\pi} = \frac{L}{(1/2)\rho_\infty V_\infty^2 S \pi}, \tag{2.5}$$

By letting = 2 and $S = 2R^2$, equation (2.5) may be simplified to

$$v = \frac{L}{2\pi R^2 \rho_\infty V_\infty}, \tag{2.6}$$

in which the fact that $\alpha_i = v/V_\infty$ (provided that $v \ll V_\infty$) has been used.

As seen, equation (2.6) is identical to the Glauert's equation considering the fact that for the wing, the force acting normal to the planform is almost equivalent to the lift L, i.e. $T \simeq L$, and $V_{res} \simeq V_\infty$.

From the above discussions, one may view the appearance of the induced flow velocities for the two limiting configurations (i.e. wind energy extracting device and wing flying on a rectilinear trajectory) as a result of two seemingly independent physical mechanisms: (i) the effective solidity of an energy device, and (ii) the generation of a vortex sheet trailing from the wing trailing edge. Thus, for an intermediate configuration, such as a finite-aspect-ratio wing flying on a circular or a figure-of-eight trajectory, it may be reasonable to assume both mechanisms of induced flow velocity generation to be active. Nevertheless, it should be noted that for an energy extracting device with multiplicity of rotating blades the appearance of induced flow velocities may also be linked to the generation of vortex rings from the tips of rotating blades, forming a 'vortex cylinder' [54].

One reasonable interpretation of equation (2.4) can be made using the well-known concept of the streamtube. A streamtube may be considered as a hypothetical control volume enclosing the actuator disc and extending axially between two control surfaces located far upstream (i.e. inlet) and far downstream (i.e. outlet) from the disc. Equation (2.4) may then be explained as the axial flow momentum change between the inlet and the outlet of the streamtube. Since the mass flow rate through the disc and thus through the streamtube is $\dot{m}$, then the change in the axial component of the flow velocity between the inlet and the outlet is equal to $2v$ [64]. Since the relative axial flow velocity at the inlet of the streamtube around the kite is $V_\infty \sin i \cos\beta - V_d$, then using the definition of a, the relative flow velocity at the outlet (or the relative wake velocity), $V_{w,rel}$, may be obtained as

$$V_{w,rel} = (V_\infty \sin i \cos\beta - V_d) - 2v = V_\infty(\sin i \cos\beta - e - 2a). \tag{2.7}$$

A constraint can be made on the numerical values of a (or on the maximum value of e) by considering the fact that $V_{w,rel} \geq 0$, meaning that there should not be a reverse flow at the outlet. This leads to

$$0 \leq a \leq \frac{(\sin i \cos\beta - e)}{2}. \tag{2.8}$$

Glauert's [63] equation may be re-written in the differential form which gives the thrust over an annular element of the width dr as

$$\mathrm{d}T = 4\pi\rho_\infty V_{res} v r \mathrm{d}r, \tag{2.9}$$

where r is the local radial distance from the centre of rotation.

For the configuration shown in Figure 2.1, the resultant flow velocity at the rotor plane (or disc) may be written as

$$V_{res}^2 = (V_\infty \sin i \cos\beta - v - V_d)^2 + (V_\infty \cos i \cos\beta)^2 + (V_\infty \sin\beta)^2. \tag{2.10}$$

Using equations (2.9) and (2.10), and the definition of the induction factor and the reel-out ratio, one can write

$$\mathrm{d}T = \frac{1}{2}\rho_\infty V_\infty^2 8\pi r a \Big[(\sin i \cos\beta - a - e)^2 + (\cos i \cos\beta)^2 + \sin^2\beta\Big]^{\frac{1}{2}} \mathrm{d}r. \tag{2.11}$$

2.2.2 Blade element considerations

Figure 2.2 shows the velocity components on the plane of rotation for a kite at the azimuth angle ψ, which is measured counterclockwise from the lowest kite position on the flight trajectory. The component of the relative flow velocity tangential to the rotation plane at the kite position is given by $V_T = r\Omega + V_\infty \cos i \cos\beta \sin\psi + V_\infty \sin\beta \cos\psi$, Ω being the rotational speed of the kite. As seen from the velocity triangle shown in Figure 2.3, the relative flow velocity at the kite element is $V_{rel}^2 = V_P^2 + V_T^2$, where $V_P = V_\infty \sin i \cos\beta - v - V_d$ is the component of the velocity perpendicular to the plane of rotation. The time-averaged value of V_{rel}^2 over one cycle of rotation, i.e. ${V_{rel}}^2$, may be written as

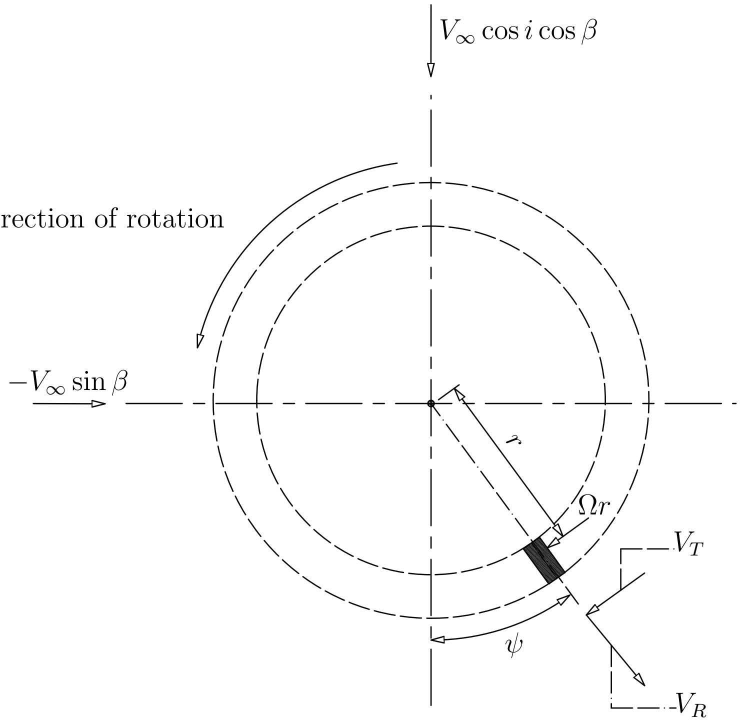

Figure 2.2: A schematic drawing showing the kite in the rotation plane; V_T and V_R are the tangential and radial components of the in-plane relative flow velocity; V_∞ is the freestream velocity, β and i are the side-slip and incidence angles, respectively; also, Ω is the rotational speed, r the radial distance, and ψ the azimuth angle.

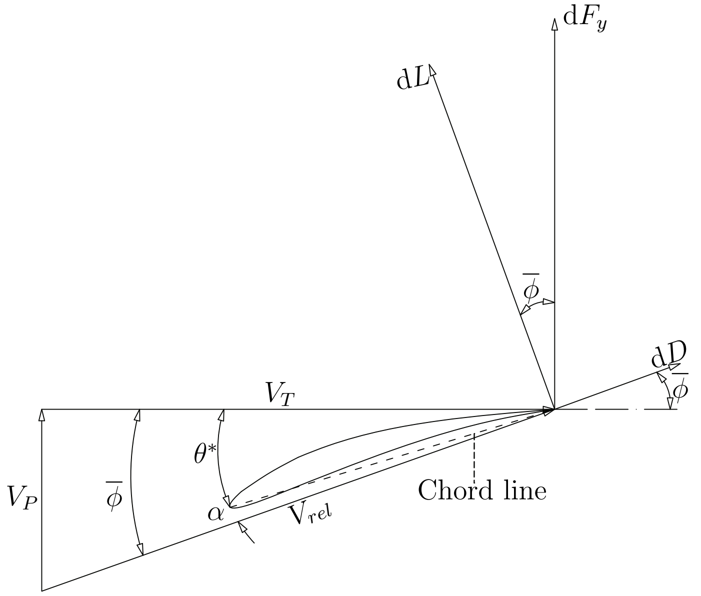

Figure 2.3: A schematic drawing showing the velocity triangle for an airfoil element of the kite. In the figure, V_{rel} is the relative flow velocity, and V_T and V_P are the components of V_{rel}, tangential and perpendicular to the rotation plane, respectively; $\overline{\phi}$, α and θ^* are the (time-averaged) inflow angle, the angle of attack, and the effective pitch angle, respectively; also, $\mathrm{d}L$, and $\mathrm{d}D$ are the differential aerodynamic lift and drag, respectively, and $\mathrm{d}F_y$ is the resultant aerodynamic force normal to the rotation plane.

$$\overline{V_{rel}}^2 = \frac{1}{2\pi}\int_0^{2\pi} V_{rel}^2\, d\psi = V_\infty^2\Big[(\sin i \cos\beta - a - e)^2 + \lambda_r^2 + \frac{1}{2}(\cos i \cos\beta)^2 + \frac{1}{2}\sin^2\beta\Big], \quad (2.12)$$

where $\lambda_r = (r\Omega/V_\infty)$ is the local crosswind speed ratio; also, the fact that $\int_0^{2\pi}\sin^2\psi\ \mathrm{d}\psi = \int_0^{2\pi}\cos^2\psi\ \mathrm{d}\psi = \pi$, and $\int_0^{2\pi}\sin\psi\ \mathrm{d}\psi = \int_0^{2\pi}\cos\psi\ \mathrm{d}\psi = \int_0^{2\pi}\sin 2\psi\ \mathrm{d}\psi = 0$ have been used.

From the velocity triangle shown in Figure 2.3, the time-averaged, local inflow angle $\overline{\phi}$ may be obtained as (refer to Appendix B for the detailed derivation)

$$\tan\overline{\phi} = \frac{\sin i \cos\beta - e - a}{\lambda_r}. \quad (2.13)$$

The pitch angle θ is commonly defined as the angle between the plane of rotation and the zero-lift line of the airfoil section, that is measured positive in the counterclockwise direction from the rotational plane [54]. If $\alpha_{L=0}$ represents the zero-lift angle of attack, which is negative for a positive-cambered airfoil and vice versa, then for the convenience of application, let us define $\theta^* = \theta - \alpha_{L=0}$, where θ^* may be called as the effective pitch angle measured with respect to the chord line. If α is the effective angle of attack of the airfoil/wing, then

$$\alpha = \overline{\phi} - \theta^* - \alpha_i, \tag{2.14}$$

where α_i is the induced angle from tip vortex considerations and becomes relevant only when airfoil data (not modified for three-dimensionality effects) is used and the analysis considers a non-uniform inflow. When wing data is used, this is already incorporated in the data and need to be substituted as zero.

The axial force acting on a differential element of the kite can be obtained by adding differential components of lift and drag, dL and dD, respectively, along the rotation axis as (see Figure 2.3):

$$\mathrm{d}F_y = \mathrm{d}L \cos\overline{\phi} + \mathrm{d}D \sin\overline{\phi}. \tag{2.15}$$

It should be noted that dL, dD, and ϕ and thus dF_y, and in general, all the aerodynamic variables involved in the blade element model are time-averaged over one cycle of rotation, i.e. $0 \leq \psi \leq 2\pi$, and the *overbar* is removed starting from here for the sake of clarity of the formulation.

Using the definition of lift and drag and equation (2.12), dF_y may be expressed as

$$\mathrm{d}F_y = \frac{1}{2}\rho_\infty V_\infty^2 c\mathrm{d}r\big(c_l\cos\phi + \widehat{c}_d\sin\phi\big)\Big[(\sin i\cos\beta - a - e)^2 + \lambda_r^2 + \frac{1}{2}(\cos i\cos\beta)^2 + \frac{1}{2}\sin^2\beta\Big], \tag{2.16}$$

where c_l is the lift coefficient of the airfoil section of the kite, and $\widehat{c}_d = c_d + C_{D_T}$ is the total drag coefficient which is the sum of the kite airfoil drag coefficient, c_d, and the tether equivalent drag coefficient, C_{D_T}, respectively; also, c is the chord length.

The local axial force coefficient may also be defined as

$$c_y = \big(c_l \cos\phi + \widehat{c}_d \sin\phi\big) \Big[(\sin i \cos\beta - a - e)^2 + \lambda_r^2 + \frac{1}{2}(\cos i \cos\beta)^2 + \frac{1}{2}\sin^2\beta\Big]. \qquad (2.17)$$

As shown, for example, by [65, 66], the equivalent tether drag is obtained by finding the moment due to the distributed drag, which acts in the same direction as that of the kite, with respect to the ground station:

$$F_{D_T} = \frac{1}{8}\rho_\infty {V_{rel}}^2 A_T C_{D_S}, \qquad (2.18)$$

where A_T is the projected area of the tether to the relative flow and C_{D_S} is the drag coefficient for the flow normal to the tether, which generally depends on the shape, surface roughness and the flow Reynolds number.

The equivalent tether drag coefficient can be obtained by normalising the drag with respect to the kite planform area A_k; thus,

$$C_{D_T} = \frac{1}{4}\frac{A_T}{A_k} C_{D_S}. \qquad (2.19)$$

If the tether is cylindrical, then $A_T = d_T L_T$; d_T and L_T being the tether diameter and length, respectively; also, $C_{D_S} = 1$ is normally taken, which is valid for the range of the Reynolds number relevant to CKPSs [67].

2.2.3 Aerodynamic model 1

Aerodynamic model 1 is developed considering the entire kite and the swept area as two whole bodies; in other words, the inflow/loading is assumed to be uniformly distributed over the rotation plane or swept area, and the kite is represented only by its span mid-point. The following assumptions are made in order to build the model:

1. The incidence angle i is high and the side-slip angle β is low, i.e. $\sin i \sim \mathcal{O}(1)$ and $\cos\beta \sim \mathcal{O}(1)$
2. The kite crosswind speed is very large compared to the freestream velocity, i.e. $\lambda_R = (\Omega R/V_\infty) \gg 1$, where R is the gyration radius or the radial distance of the kite mid-span point from the rotation axis
3. The net aerodynamic force acting in the tangential (or rotation) direction is zero, which ensures that the rotation takes place at a constant speed

In this section, the steady-state rotation is assumed to be achieved aerodynamically in two different ways: (i) by adjusting the pitch angle of the kite system, θ^*, or (ii) by adding an air brake that can increase drag of the kite system. The equations are written by assuming that the steady state is achieved in the former way, and the latter is explained in the solution procedure of the model.

Considering the kite at the steady state, one can write

$$C_L \sin\Phi = \widehat{C}_D \cos\Phi \quad \text{or} \quad \tan\Phi = \frac{\widehat{C}_D}{C_L}, \tag{2.20}$$

where Φ is the kite inflow angle taken at the kite mid-span point, and C_L refers to the entire kite lift coefficient and $\widehat{C}_D = C_D + C_{D_T}$, C_D being the drag coefficient of the entire kite.

Equation (2.11) is integrated over the swept area (i.e. $r_i \leq r \leq r_o$; r_i and r_o being the inner and outer radii of the annular swept area); also, considering $(a+e)^2 \approx (a+e)^2 \sin^2 i \cos^2 \beta$ based on assumption 1, one may obtain:[2]

$$T = \frac{1}{2}\rho_\infty A_s V_\infty^2 4a\Big(1-(a+e)\sin i \cos\beta\Big), \tag{2.21}$$

where $A_s = \pi({r_o}^2 - {r_i}^2)$ is the swept area.

On the other hand, the total axial force acting on the kite may be obtained by integrating equation (2.16) over the kite span (i.e. $b = r_o - r_i$) and applying assumptions 1 and 2:

$$F_y = \frac{1}{2}\rho_\infty A_k V_\infty^2 \big(C_L \cos\Phi + \widehat{C}_D \sin\Phi\big)\lambda_R^2, \tag{2.22}$$

where the kite inflow angle, Φ, can easily be found from equation (2.13) as

$$\tan\Phi = \frac{\sin i \cos\beta - a - e}{\lambda_R}. \tag{2.23}$$

According to the BEM theory, the axial load acting on the kite is equal to the thrust generated over the swept area, i.e. $F_y = T$; thus, from equations (2.21) to (2.23) and the fact that the inflow angle Φ is small (refer to assumption 2), one can write:

$$\frac{a\Big(1-(a+e)\sin i\cos\beta\Big)}{(\sin i\cos\beta - a - e)^2} = \frac{1}{4}\sigma C_L(\frac{C_L}{\widehat{C}_D})^2\big[1+(\frac{\widehat{C}_D}{C_L})^2\big], \tag{2.24}$$

where $\sigma = (A_k/A_s)$ may be defined as the kite solidity factor, in similar fashion it is defined for conventional wind turbines.

By letting $\chi = C_L(C_L/\widehat{C}_D)^2$ – which may be called the aerodynamic efficiency – and

---

[2] For $(a+e) \leq 0.5$, equation (2.21) provides a fair approximation of the exact expression given in equation (2.11), and the numerical results for $(a+e) > 0.5$ should be taken with a grain of salt.

neglecting $(\widehat{C}_D/C_L)^2$, a may be obtained from the following quadratic equation:

$$(\mathcal{A}+\sin i\cos\beta)a^2+\big[e\sin i\cos\beta-2\mathcal{A}(\sin i\cos\beta-e)-1\big]a+\mathcal{A}(\sin i\cos\beta-e)^2=0, \quad (2.25)$$

where $\mathcal{A}=(1/4)\sigma\chi$.

For a crosswind kite system with the known solidity factor σ, reel-out ratio e, incidence angle i, side-slip angle β, tether equivalent drag coefficient C_{D_T} and predefined constant values of C_L and (C_L/C_D), equation (2.25) can be solved directly to obtain the induction factor a. Equation (2.8) should then be consulted to find the acceptable root. Once a is found, equation (2.2) may be used to find $\tilde{a}$.

If, however, the aerodynamic coefficients are not known *a priori*, then the solution may be obtained through an iterative process, where values of C_L and C_D versus angle of attack α for the kite should be at hand. Knowing also the equivalent tether drag coefficient C_{D_T}, one can make a table listing values of $(C_L/\widehat{C}_D)$ versus α, for the use in the iterative process. As discussed earlier in this section, one way to achieve the steady-state rotation is by adjusting θ^*. Approach I provides the solution through finding iteratively the value of θ^* such that the net tangential aerodynamic force becomes nil; the pitch angle θ^* cannot then be known beforehand in this approach; see Table 2.1 for the algorithm.

An alternative to approach I, which we call approach II, is to achieve the steady state with the help of a drag device, where the pitch angle θ^* can be given as an input. Thus, in approach II, the kite system drag, that is inclusive of the kite and tether drag, needs to be adjusted such that $\widetilde{C}_D=C_L\tan\Phi$, where $\widetilde{C}_D$ is the adjusted drag coefficient. This also means that $\widehat{C}_D$ in equation (2.25) is replaced with $\widetilde{C}_D$. The algorithm for approach II is outlined in Table 2.2. In most cases, the adjusted drag coefficient is higher than the drag coefficient obtained from data interpolation, i.e. $\widetilde{C}_D>\widehat{C}_D$. In those cases, the required

Table 2.1: Approach I for obtaining the induction factor

Step	Task
1	Consider a guess value for a , i.e. a_{guess}
2	With a_{guess} and knowing e, i, β and λ_R, obtain the inflow angle Φ from equation (2.23)
3	With Φ, obtain $(\widehat{C}_D/C_L)$ from applying assumption 3
4	Obtain the angle of attack α as well as C_L and C_D by doing interpolations within $(\widehat{C}_D/C_L) - \alpha$, $C_L - \alpha$ and $C_D - \alpha$ tables, respectively
5	Obtain the pitch angle θ^* from equation (2.14)
6	Obtain a new value for a (i.e. a_{new}) from equation (2.25) and by considering the condition in equation (2.8)
7	If $\lvert a_{\text{new}} - a_{\text{guess}} \rvert < \varepsilon$ (ε being a small number), then converged values have been obtained; otherwise, $a_{\text{guess}} = a_{\text{new}}$ and go to step 2

Table 2.2: Approach II for obtaining the induction factor

Step	Task
1	Consider a guess value for a , i.e. a_{guess}
2	With a_{guess} and knowing e, i, β and λ_R, obtain the inflow angle Φ from equation (2.23)
3	With Φ and knowing θ^*, obtain the angle of attack α from equation (2.14)
4	Obtain C_L and C_D by doing interpolations within $C_L - \alpha$ and $C_D - \alpha$ tables, respectively
5	Obtain the adjusted drag coefficient from $\widetilde{C}_D = C_L \tan \Phi$
6	Obtain a new value for a (i.e. a_{new}) from equation (2.25) and by considering the condition in equation (2.8) while substituting adjusted drag coefficient $\widetilde{C}_D$ instead of the actual drag coefficient $(\widehat{C}_D)$
7	If $\lvert a_{\text{new}} - a_{\text{guess}} \rvert < \varepsilon$ (ε being a small number), then converged values have been obtained; otherwise, $a_{\text{guess}} = a_{\text{new}}$ and go to step 2

added drag (to maintain the steady-state flight condition) may be thought to be provided, for example, through air brakes; this is, however, with the assumption that air brakes do not have an impact on the lift coefficient. On the other hand, for cases where $\widetilde{C}_D < \widehat{C}_D$ and thus the added drag is negative, one may assume that flow control strategies have been employed to reduce the drag over the kite. Nevertheless, this is only an imaginary solution where the practical implementation could be quite complex.

It should be noted that, for the sake of brevity, only numerical results obtained via approach II are provided in this paper. For all the results presented, so as to obtain a fair comparison, the chosen λ_R is multiplied by $\sin i \cos\beta$ for use in respective incidence and side-slip angle cases as it will keep the ratio of the crosswind speed to wind speed available to the rotational plane constant for all cases. It should also be noted that to ensure accuracy when getting numerical results for a kite of a certain aspect ratio , flying at a certain Reynolds number Re, the $C_L - \alpha$ and $C_D - \alpha$ tables (or 3D polars) for a wing of the same and Re should be used. If polars for a wing with a different aspect ratio is available, they may be 'corrected' for the effect of using, for example, Prandtl's equation [68].

The power harnessed by the kite may be expressed in two different ways depending whether T or F_y is used for power calculation, i.e. $P^{(s)} = TV_d$ and $P^{(k)} = F_y V_d$, the former being the *swept-area-based* power while the latter being the *kite-area-based* power. The power output is usually expressed in the dimensionless form as:

$$C_p^{(s)} = \frac{P^{(s)}}{\frac{1}{2}\rho_\infty A_s V_\infty^3} = 4ae\Big(1 - (a+e)\sin i \cos\beta\Big), \tag{2.26}$$

and

$$C_p^{(k)} = \frac{P^{(k)}}{\frac{1}{2}\rho_\infty A_k V_\infty^3} = C_L\big(\frac{C_L}{\widehat{C}_D}\big)^2(\sin i \cos\beta - a - e)^2 e, \tag{2.27}$$

where $C_p^{(s)}$ and $C_p^{(k)}$ are the swept- and kite-area-normalised power coefficients, respectively.

As discussed in [1], for kite power systems, the kite-area-normalised power coefficient is a more suitable performance metric, compared to the swept-area-normalised power coefficient that is typically used in the literature. Thus, in most cases, the numerical values obtained for $C_p^{(k)}$ will be shown in the present paper. By letting $i = 90°$, $\beta = 0$, $C_{D_T} = 0$ (i.e. the kite is in the straight downwind configuration with no side-slip and negligible tether drag) and replacing a with $\tilde{a}$ (refer to equation (2.2)) and using equation (2.24), equation (2.27) reduces to (the proof is left to the reader)

$$C_p^{(k)} = \frac{\chi}{(1 + \frac{1}{4}\sigma\chi)^2}(1 - e)^2 e, \tag{2.28}$$

which is exactly the same as the equation obtained in Ref. [1] for a CKPS in the straight downwind configuration.

2.2.4 Aerodynamic model 2

Similar assumptions as those made in Section 2.2.3 are also considered here with the exception that the excessive aerodynamic force in the tangential direction is not wasted; instead, it is used to produce additional torque power, which in turn, maintains the steady-state rotation/flight. The torque power may be thought to be produced via on-board turbines (similarly to that for drag mode CKPSs) or via a ground-based mechanism (similarly to that for conventional wind turbines). Thus, model 2 may be considered as the aerodynamic model for the hybrid reel-out-torque (or lift-drag) power generation. Unlike aerodynamic model 1, model 2 is formulated for a non-uniform inflow distribution over the swept area, which can also be adapted for a uniform inflow distribution, if needed.

Let us begin with the derivation for the non-uniform inflow distribution. We extend assumption 2 mentioned in Section 2.2.3 such that it is valid for any point along the kite span, i.e. $\lambda_r \gg 1$; thus, equation (2.16) may be re-written as

$$\mathrm{d}F_y = \frac{1}{2}\rho_\infty V_\infty^2 c \lambda_r^2 (c_l \cos\phi + \widehat{c}_d \sin\phi)\mathrm{d}r. \tag{2.29}$$

Table 2.3: Approach III for obtaining the induction factor

Step	Task
1	Divide the kite span into N number of elements of the length dr and choose the first element to initiate the solution process; repeat the process for all the elements
2	Consider a guess value for a , i.e. a_{guess}
3	With a_{guess} and knowing e, i, β and λ_r, obtain the local inflow angle $\overline{\phi}$ from equation (2.13)
4	With $\overline{\phi}$ and knowing θ^*, obtain the angle of attack α from equation (2.14)
5	Obtain c_l and c_d by doing interpolations within $Re - c_l - \alpha$, and $Re - c_d - \alpha$ tabulated data, respectively; Re represents the sectional Reynolds's number
6	If the condition in equation (2.32) is satisfied, obtain a new value for a (i.e. a_{new}) from equation (2.25) by replacing $\mathcal{A}$ with $\mathcal{A}_r = (1/4)\sigma_r\chi_r$; and by considering the condition in equation (2.8)
7	If $\lvert a_{\text{new}} - a_{\text{guess}}\rvert < \varepsilon$ (ε being a small number), then converged values have been obtained; otherwise, $a_{\text{guess}} = a_{\text{new}}$ and go to step 3

On the other hand, equation (2.11) may be simplified as follows (see to the explanation given for equation(2.21))

$$\mathrm{d}T = \frac{1}{2}\rho_\infty V_\infty^2 8\pi r a\Big(1 - (a+e)\sin i\cos\beta\Big)\mathrm{d}r. \tag{2.30}$$

By letting dF_y = dT, which is the core concept of the BEM theory, we obtain a rational equation for the local induction factor $a = a(r)$ as

$$\frac{a\Big(1 - (a+e)\sin i\cos\beta\Big)}{(\sin i\cos\beta - a - e)^2} = \frac{1}{4}\sigma_r\chi_r, \tag{2.31}$$

where $\sigma_r = (c/2\pi r)$ is the local solidity factor and $\chi_r = (c_l\cos\phi + \widehat{c}_d\sin\phi)/\tan^2\phi$ the local aerodynamic efficiency.

The solution process is slightly different from those discussed in Section 2.2.3. The new solution process (i.e. approach III) is outlined in Table 2.3. An additional condition given in equation (2.32) is used during the solution. This will guarantee solutions for cases with torque available for auto-rotation:

$$(c_l \sin\phi - \widehat{c}_d \cos\phi) \geq 0, \tag{2.32}$$

which is similar to ensuring $\widetilde{C}_D \leq \widehat{C}_D$ in Section 2.2.3 so that only practical solutions are obtained.

The elemental (or local) values of the swept- and kite-area-normalised power coefficients are expressed, respectively, as

$$\mathrm{d}C_p^{(s)} = 4ae\Big(1 - (a+e)\sin i \cos\beta\Big), \tag{2.33}$$

and

$$\mathrm{d}C_p^{(k)} = (c_l \cos\phi + \widehat{c}_d \sin\phi)\lambda_r^2 e. \tag{2.34}$$

It should be noted that for a kite of rectangular planform, the local solidity factor σ_r may be linked to the overall solidity factor of the kite by normalising the redial distance r as $\xi = r/R$; that is

$$\sigma_r = \frac{\sigma}{\xi}, \tag{2.35}$$

where $R = \frac{1}{2}(r_i + r_o)$ is the radius of gyration.

It should be noted that when obtaining the induction factor for the uniform inflow distribution assumption, the solution procedure outlined in Table 2.3 can be used provided that the local values of the solidity factor and aerodynamic efficiency are replaced with the overall solidity factor σ and aerodynamic efficiency χ introduced in Section 2.2.3.

2.3 Results and discussions

Figure 2.4 shows the contours for the variation of the induction factor a as a function of the reel-out ratio, e, and the solidity factor σ, obtained from aerodynamic model 1 for predefined values of $C_L = 1$, and $(C_L/C_D) = 10$ and for different values of the incidence angle:

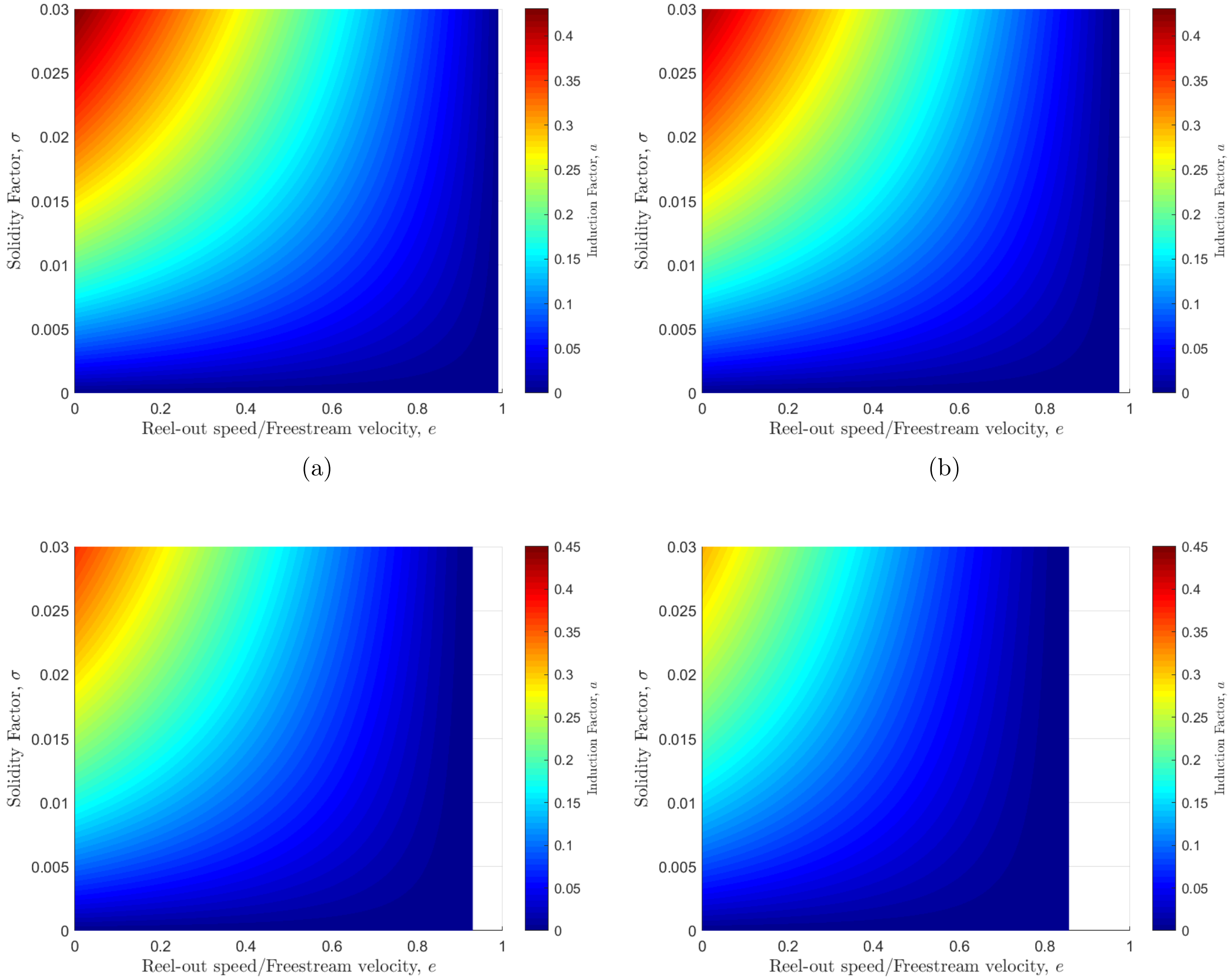

(a) (b)

(c) (d)

Figure 2.4: Contour plots showing the variation of the induction factor a as a function of the ratio of reel-out speed to freestream velocity, e, and solidity factor σ from aerodynamic model 1: (a) $i = 90°$, (b) $i = 80°$, (c) $i = 70°$ and (d) $i = 60°$; predefined values are $C_L = 1$, $(C_L/C_D) = 10$, $C_{D_T} = 0$, and $\beta = \theta^* = 0°$.

(a) $i = 90°$, (b) $i = 80°$, (c) $i = 70°$, and (d) $i = 60°$; also, $C_{D_T} = 0$, and $\beta = \theta^* = 0°$. The upper limit values of σ are typical solidity factors of modern conventional wind turbines (see, e.g., Ref. [54]) whereas the lower limit values seem to be more representative of CKPSs. For example, Makani's M600 kite has the wing span of 25.7 m, the wing area of 32.9 m^2, and it flies in an orbit of the radius of 145 m [69]; these yield to $\sigma \simeq 0.0045$.

As seen from Figure 2.4, as the reel-out ratio e is increased, a decreases. This is because by increasing e, the relative oncoming flow velocity that is available to the kite and thus the induced velocity are reduced. In this case, to keep C_L and (C_L/C_D) and more precisely, the angle of attack, constant, the crosswind speed should be decreased as e is increased. In contrast, as the solidity factor σ is increased, a is also increased, which is because a larger kite (flying over the same swept area) can harness more power from the wind and thus induce more flow retardation. On the other hand, in the limit of $\sigma \to 0$, $a \to 0$ since the kite harness wind energy from an infinitely large swept area and its effect on the freestream is negligible. In addition, as seen from Figure 2.4, by decreasing the incidence angle i from $i = 90°$ to $i = 60°$, a is decreased since the component of the flow velocity normal to the rotation plane is reduced; the acceptable range for e also narrows when i is decreased. It should be noted that since in the derivation of equations it was assumed that $\sin i \sim \mathcal{O}(1)$, numerical results presented here and later, for lower values of i, particularly for $i = 60°$, should be taken with a grain of salt.

In general, similar trends as those observed for a in Figure 2.4 are also observed for $\tilde{a}$ for similar operational parameters (the plots are not presented here for the sake of brevity). One exception is that for $i = 90°$ (i.e. the straight downwind configuration), for any solidity factor σ, $\tilde{a}$ is independent of e – a similar result was obtained by Kheiri et al. [30]. However, as i is decreased, $\tilde{a}$ becomes increasingly dependent on e.

Figure 2.5 shows the variation of the kite-area-normalised power coefficient $C_p^{(k)}$ (refer

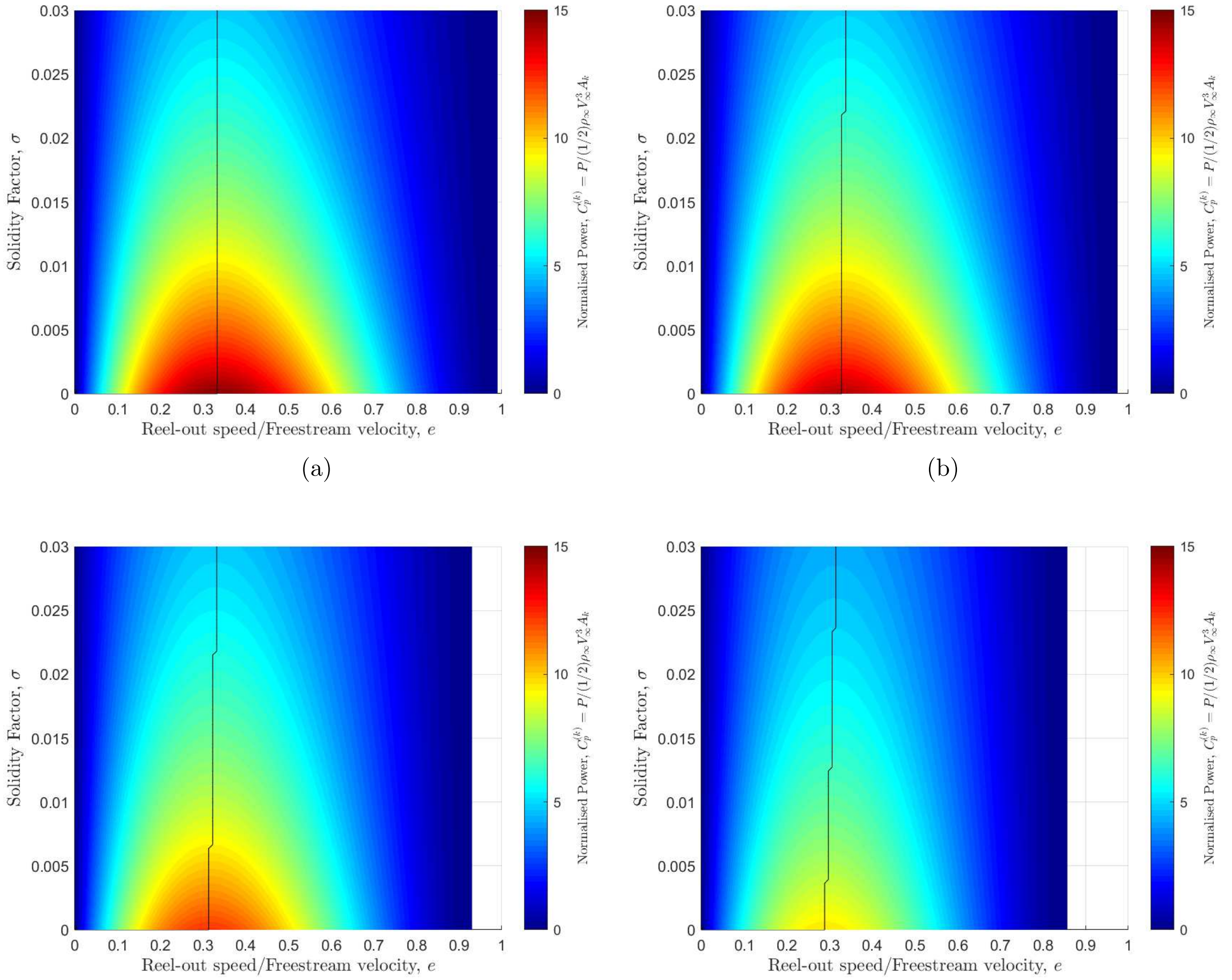

(a)

(b)

(c)

(d)

Figure 2.5: Contour plots showing the variation of the kite-area-normalised power coefficient, $C_p^{(k)} = P/(1/2)\rho_\infty V_\infty^3 A_k$, as a function of the ratio of reel-out speed to freestream velocity, e, and solidity factor σ from aerodynamic model 1: (a) $i = 90°$, (b) $i = 80°$, (c) $i = 70°$ and (d) $i = 60°$; predefined values are $C_L = 1$, $(C_L/C_D) = 10$, $C_{D_T} = 0$, and $\beta = \theta^* = 0°$. The solid line shows the locus of the maximum power coefficient.

to equation (2.27) for the definition) as a function of e and σ, obtained from aerodynamic model 1, for pre-defined values of $C_L = 1$, and $(C_L/C_D) = 10$ and for different values of the incidence angle: (a) $i = 90°$, (b) $i = 80°$, (c) $i = 70°$, and (d) $i = 60°$; also, $C_{D_T} = 0$, and $\beta = \theta^* = 0°$. The solid black line in the plots represents the locus of the optimal power coefficient. As seen from Figure 2.5 (a), the maximum power occurs over the $e = 1/3$ line, independently from the solidity factor. For CKPSs with zero solidity factor, Loyd [10] showed analytically that the maximum power is reached at $e = 1/3$; a similar conclusion was made by Kheiri et al. [30] for straight-downwind (i.e. $i = 90°$) CKPSs of arbitrary solidity factor.

However, as seen from Figure 2.5 (b)-(d), the locus of the optimal power remains no longer a single straight line. As i is decreased from $i = 90°$ to $i = 60°$, the optimal e becomes increasingly dependent on σ, with the optimal points shifting generally towards values lower than $e = 1/3$; this shift is more evident for smaller values of σ. In other words, as the incidence angle is decreased, the kite should be reeled-out at a lower speed to produce maximum power. A conceptually important observation from the power coefficient plots is that the maximum of $C_p^{(k)}$ for an arbitrary e lies on the $\sigma = 0$ line. This means that a kite with given dimensions can harness the maximum power when flying on an infinitely large swept area; this is consistent with the observations made by Loyd [10], Diehl [13], and Kheiri et al. [1].

Figure 2.6 shows similar contour plots as those shown in Figure 2.4 but for kite systems with $C_{D_T} = 0.025$ and $\beta = 15°$. When compared to Figure 2.4 plots, it is seen that a is generally decreased due to the combined effect of a non-zero side-slip angle and a non-zero tether drag coefficient. In addition, the acceptable range for e becomes narrower. Figure 2.7 shows the corresponding $C_p^{(k)}$ plots. Compared to the plots in Figure 2.5, $C_p^{(k)}$ has been diminished over the entire plane since the non-zero β reduces the magnitude of the component of freestream normal to the rotation plane, and the non-zero C_{D_T} reduces the aerodynamic efficiency of the kite.

Figure 2.8 shows the variation of (a,b) a, and (c,d) $C_p^{(k)}$ as a function of e, obtained from

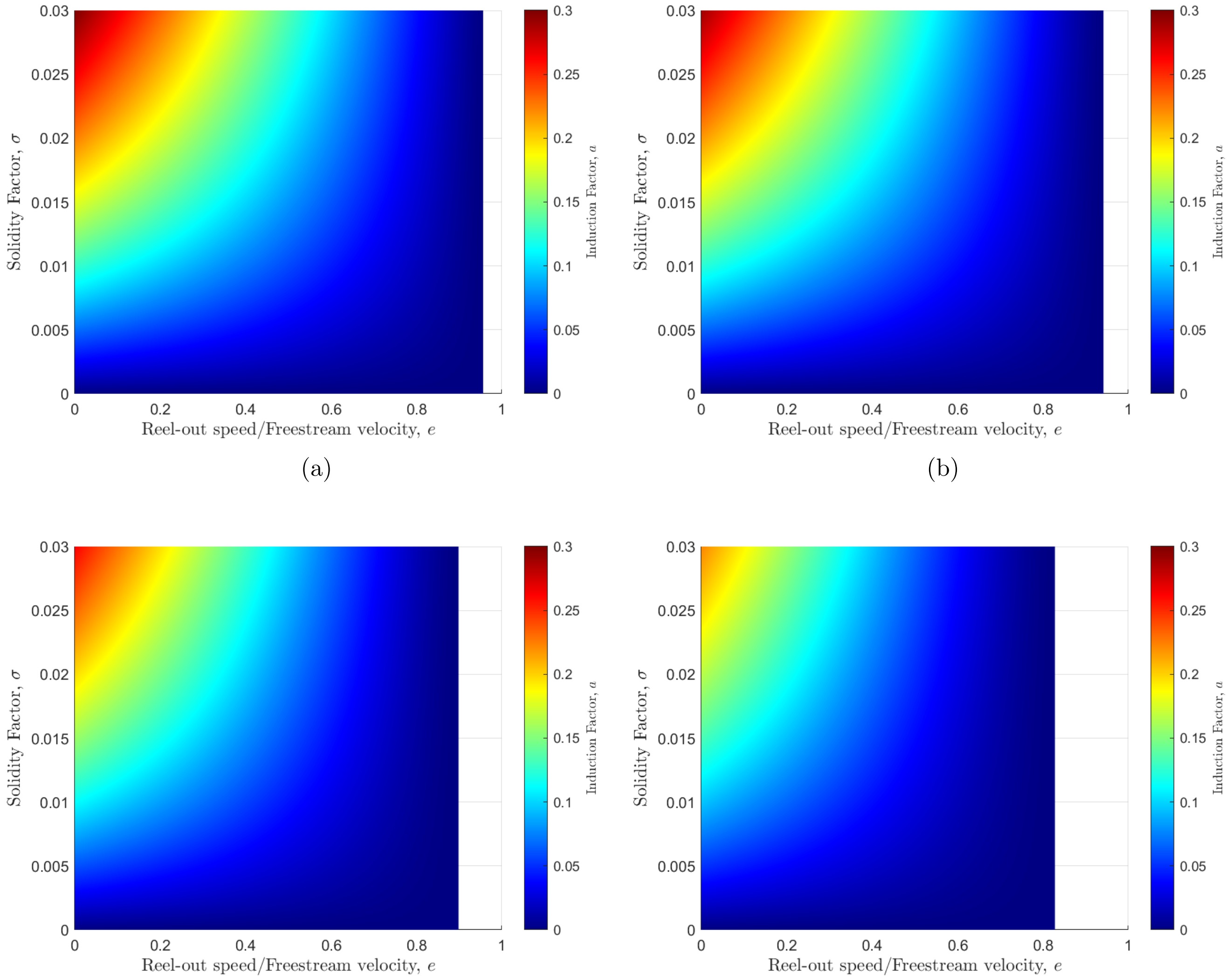

(a) (b) (c) (d)

Figure 2.6: Contour plots showing the variation of the induction factor a as a function of the ratio of reel-out speed to freestream velocity, e, and solidity factor σ from aerodynamic model 1: (a) $i = 90°$, (b) $i = 80°$, (c) $i = 70°$ and (d) $i = 60°$; predefined values are $C_L = 1$, $(C_L/C_D) = 10$, $C_{D_T} = 0.025$, $\beta = 15°$, and $\theta^* = 0°$.

aerodynamic model 1 for a crosswind kite of a rectangular planform with Clark Y airfoil sections and aspect ratio = 14.5; also, $\lambda_R = 7.28$, $C_{D_T} = 0$, and $\beta = \theta^* = 0°$. The plots have been shown for (a,c) $\sigma = 0$, and (b,d) $\sigma = 0.0048$. The results have been obtained for four different incidence angles: $i = 90°$ (solid line), $i = 80°$ (dashed line), $i = 70°$ (dotted line),

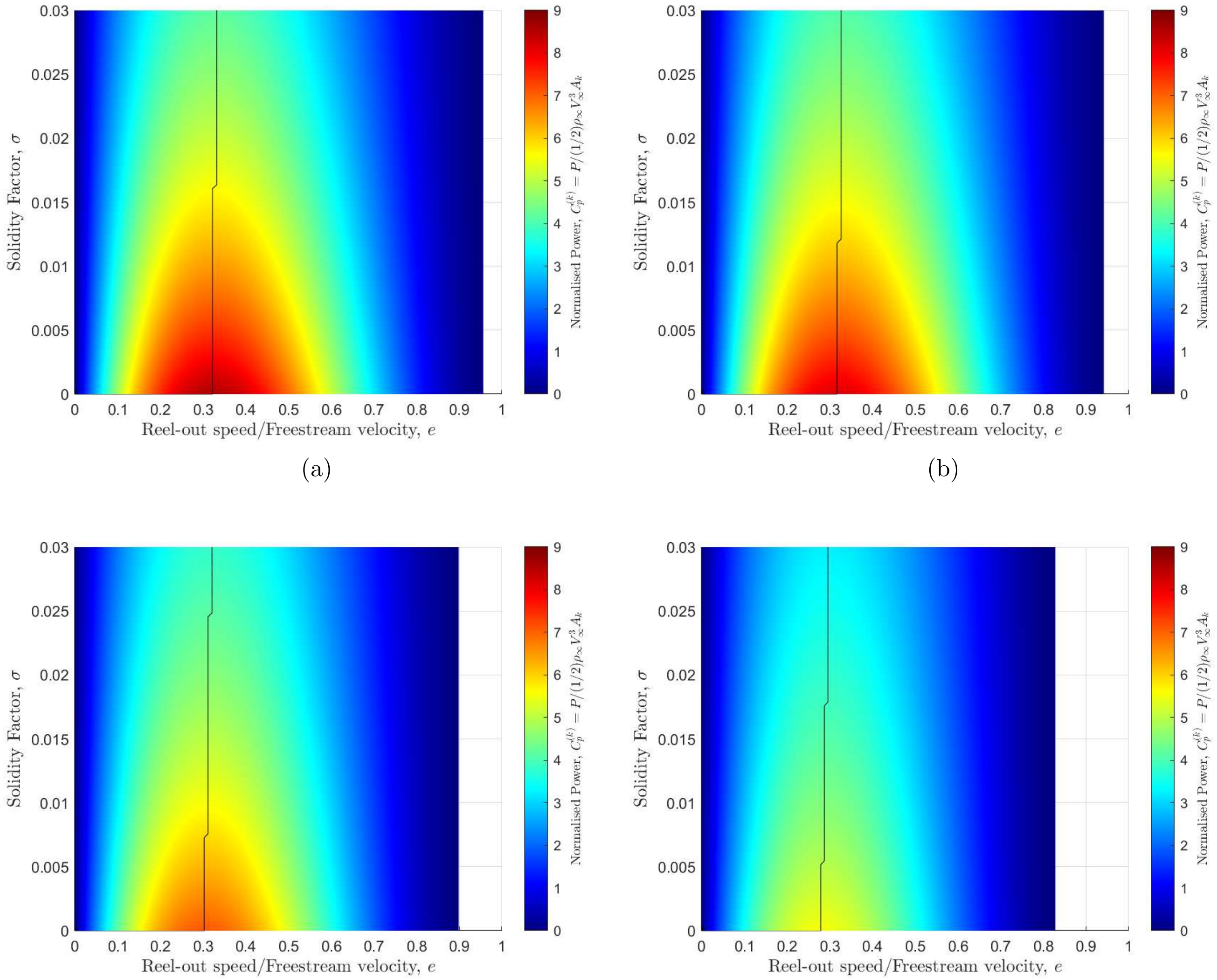

(a) (b)

(c) (d)

Figure 2.7: Contour plots showing the variation of the kite-area-normalised power coefficient, $C_p^{(k)} = P/(1/2)\rho V_\infty^3 A_k$, as a function of the ratio of reel-out speed to freestream velocity, e, and solidity factor σ from aerodynamic model 1: (a) $i = 90°$, (b) $i = 80°$, (c) $i = 70°$ and (d) $i = 60°$; predefined values are $C_L = 1$, $(C_L/C_D) = 10$, $C_{D_T} = 0.025$, $\beta = 15°$, and $\theta^* = 0°$. The solid line shows the locus of the maximum power coefficient.

and $i = 60°$ (dash-dotted line). As discussed in Section 2.2.3, the ratio of the crosswind speed to wind speed available to the rotational plane is kept constant for different incidence and side-slip angles by multiplying λ_R by $\sin i \cos\beta$.

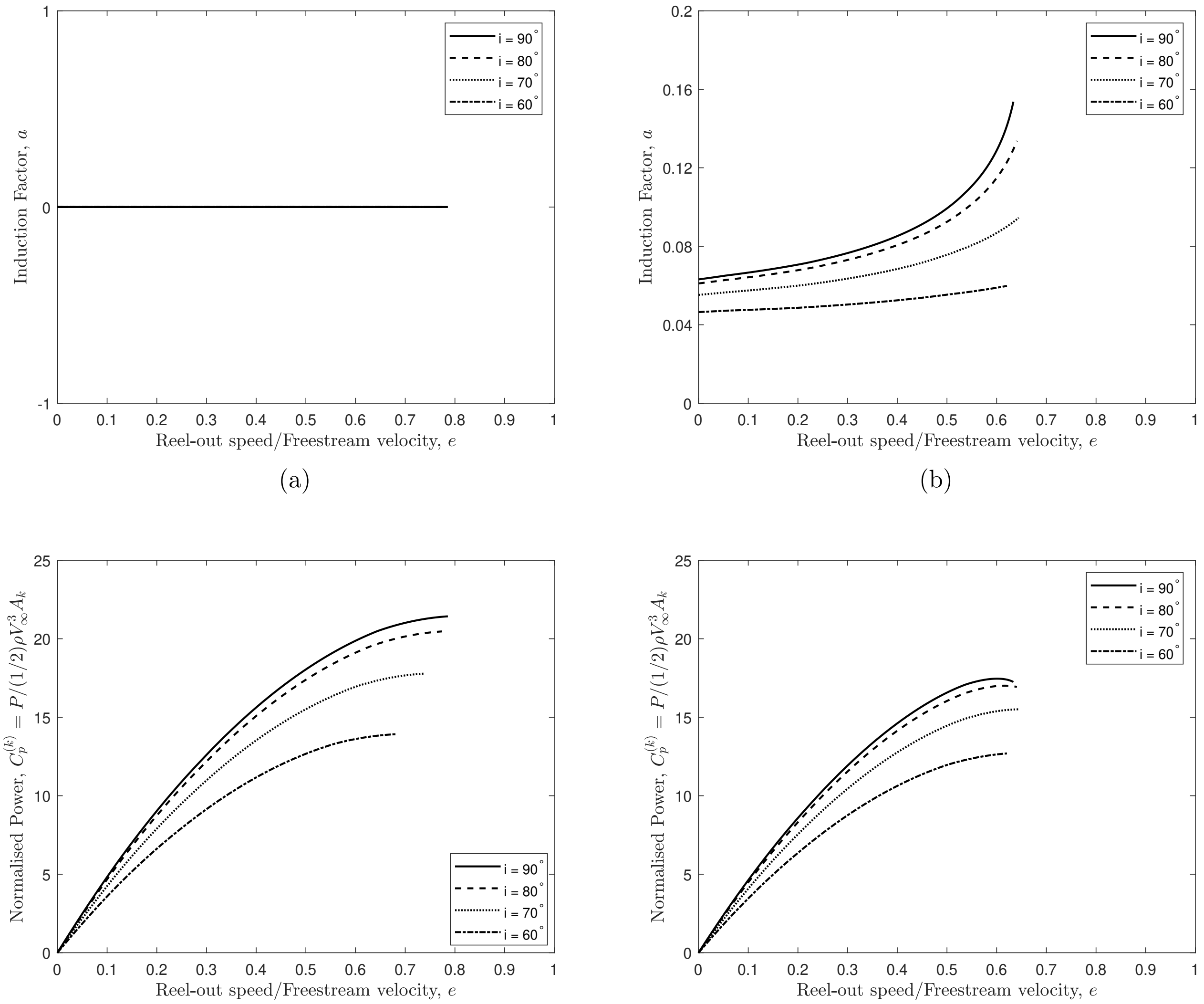

(a) (b)

(c) (d)

Figure 2.8: Plots showing the variation of (a,b) the induction factor a, and (c,d) the kite-area-normalised lift power coefficient, $C_p^{(k)} = P/(1/2)\rho V_\infty^3 A_k$, as a function of the reel-out ratio, e, for different incidence angles i (solid line: $i = 90°$, dashed line: $i = 80°$, dotted line: $i = 70°$, dash-dotted line: $i = 60°$) from aerodynamic model 1: (a,c) $\sigma = 0$, and (b,d) $\sigma = 0.0048$. The kite is a uniform wing of the aspect ratio =14.5 and Clark Y airfoil sections; also, $\lambda_R = 7.28$, $C_{D_T} = 0$, and $\beta = \theta^* = 0°$.

As seen from Figure 2.8 (a), the induction factor for a zero-solidity CKPS is zero for all values of e and for any of the incidence angles, for the same reasons discussed in relation to Figure 2.4. For a CKPS with $\sigma = 0.0048$, Figure 2.8 (b) shows that a is generally dependent on both e and i. In contrast to what was shown in the contour plots for cases with pre-defined aerodynamic coefficients (see Figure 2.4), a generally increases as e is increased and in fact, rapidly at higher values of e; this is more evident for larger values of i, such as $i = 80°$, and $i = 90°$. This may seem at first glance to contradict the results shown in Figure 2.4. The difference between the trends for a shown in Figure 2.8 and Figure 2.4 may be linked to different assumptions used here and there. In contrast to cases shown previously, no assumptions were made here on the value of C_L and (C_L/C_D) for the kite. The value of C_L was found iteratively from the experimental wing data given in [70], which we corrected for the aspect ratio effect; the drag coefficient was adjusted based on the value of C_L and the inflow angle to achieve steady-state rotation aerodynamically, as explained in Section 2.2.3 and Table 2.2. By increasing e, the inflow angle Φ is decreased, which consequently results in a lower angle of attack and thus lower C_L; the adjusted drag coefficient $\widetilde{C}_D$, on the other hand, is reduced more significantly since $\widetilde{C}_D = C_L \tan\Phi$; thus, $(C_L/\widetilde{C}_D)$ and the aerodynamic efficiency χ generally increase, which result in a higher induction factor; see Figure 2.9 which shows the variation of $(C_L/\widetilde{C}_D)$ as a function of e. As also seen from Figures 2.8 and 2.9, the acceptable range for e narrows as i is decreased; this was also seen from the results for the systems with pre-defined aerodynamic coefficients; see Figures 2.4 and 2.6.

Figure 2.8 (c) shows that the maximum acceptable $C_p^{(k)}$ is reached at a lower reel-out ratio as the incidence angle is decreased from $i = 90°$ to $i = 60°$; this is again consistent with observations made on systems with pre-defined aerodynamic coefficients; however, here, the optimal values of e are much larger than $e = 1/3$; see Figures 2.5 and 2.7. It should be reminded to the reader again that the main reason for the marked difference between the optimal reel-out ratio found here and those in the preceding figures is that the aerodynamic coefficients are not kept fixed here as e is varied. This should be kept in mind when comparing the optimal values of e.

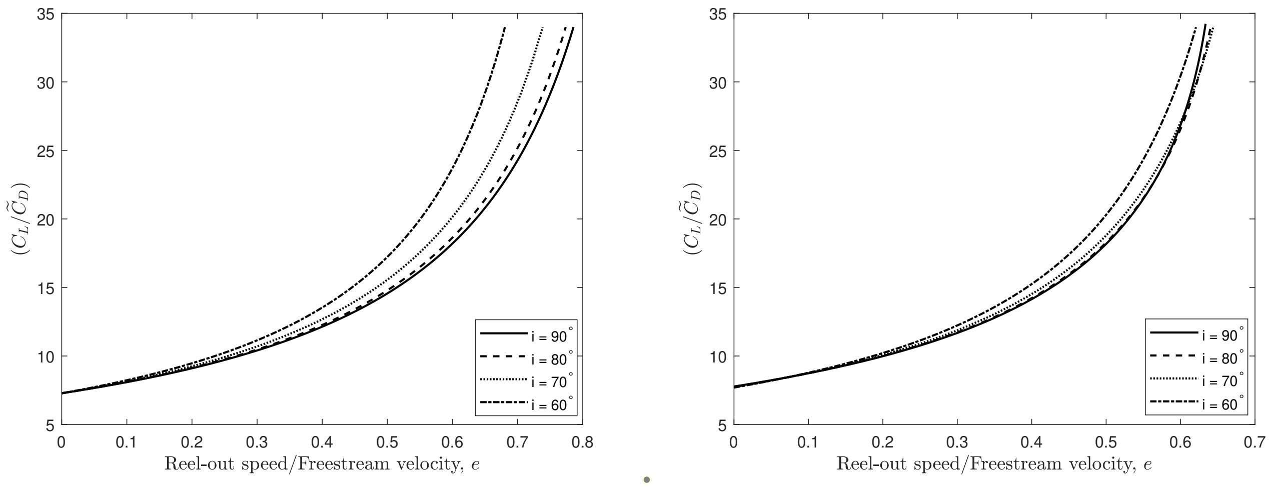

(a) (b)

Figure 2.9: Plots showing the variation of the adjusted lift-to-drag ratio, $(C_L/\widetilde{C}_D)$, as a function of the reel-out ratio, e, for different incidence angles i (solid line: $i = 90°$, dashed line: $i = 80°$, dotted line: $i = 70°$, dash-dotted line: $i = 60°$) from aerodynamic model 1: (a) $\sigma = 0$, and (b) $\sigma = 0.0048$. The kite is a uniform wing of the aspect ratio =14.5 and Clark Y airfoil sections; also, $\lambda_R = 7.28$, $C_{D_T} = 0$, and $\beta = \theta^* = 0°$.

Figure 2.8 (d), on the other hand, shows that for the kite with $\sigma = 0.0048$, the maximum acceptable $C_p^{(k)}$ may be reached at a higher or a lower reel-out ratio as i is decreased from $i = 90°$ to $i = 60°$. An interesting observation is that the optimal values of e for the four different incidence angles are very close to each other. It should be noted that the above observations are strictly valid for the specified configuration, and much more numerical results, particularly for different values of λ_R, are needed to draw some general conclusions. Such numerical studies are, however, beyond the scope of the present paper and are deferred to a future publication.

Figure 2.10 shows similar plots as those in Figure 2.8, but for kite systems with $C_{D_T} = 0.025$, and $\beta = 15°$; the rest of the system parameters remain the same. No major difference in the general trends of the curves is seen in the induction and power coefficient plots. The only noticeable difference is that the acceptable range for e narrows rather significantly for both $\sigma = 0$ and $\sigma = 0.0048$, which in turn limits the maximum achievable power to lower

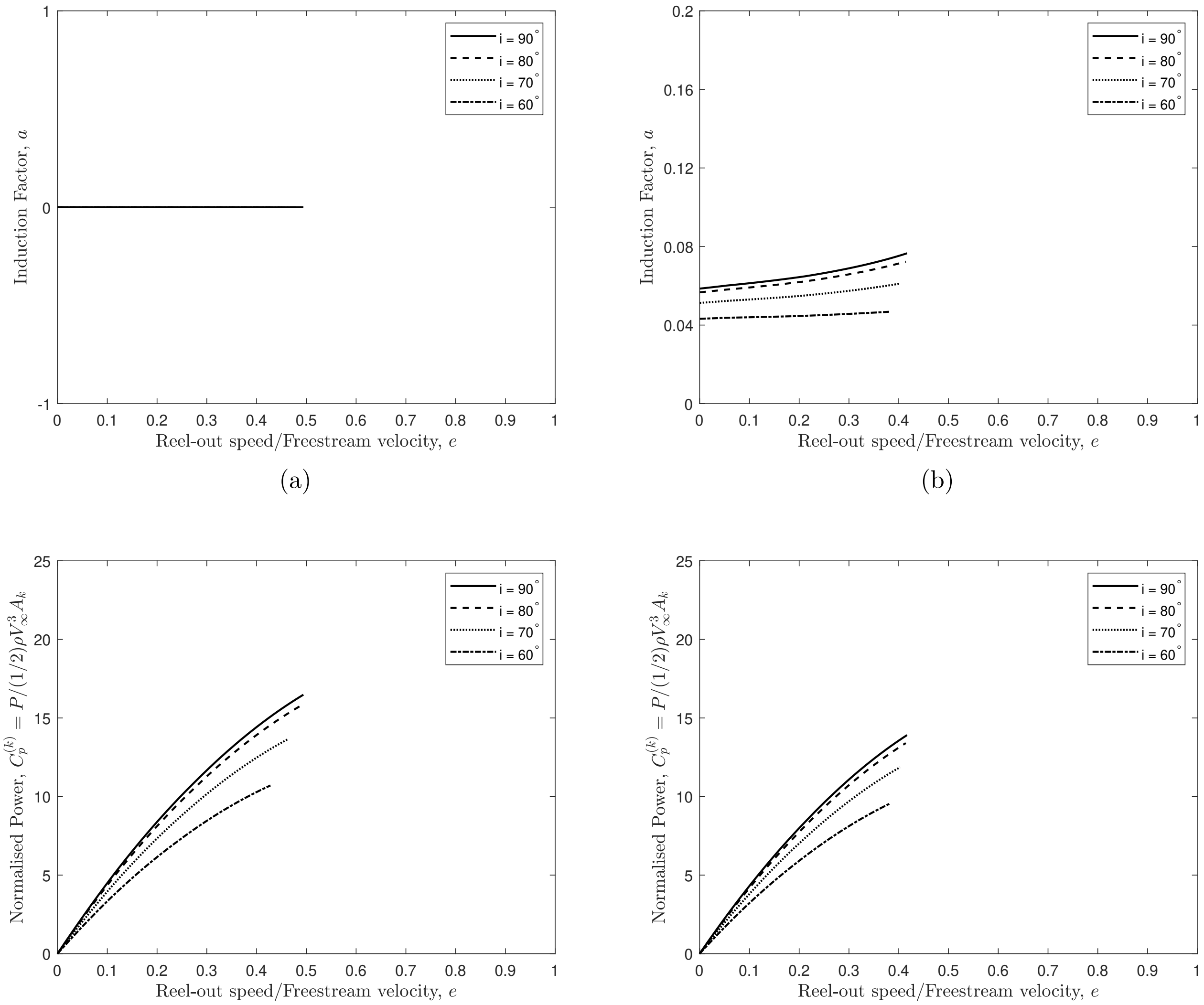

(a) (b)

(c) (d)

Figure 2.10: Plots showing the variation of (a,b) the induction factor a, and (c,d) the kite-area-normalised lift power coefficient, $C_p^{(k)} = P/(1/2)\rho V_\infty^3 A_k$, as a function of the reel-out ratio, e, for different incidence angles i (solid line: $i = 90°$, dashed line: $i = 80°$, dotted line: $i = 70°$, dash-dotted line: $i = 60°$) from aerodynamic model 1: (a,c) $\sigma = 0$, and (b,d) $\sigma = 0.0048$. The kite is a uniform wing of the aspect ratio =14.5 and Clark Y airfoil sections; also, $\lambda_R = 7.28$, $C_{D_T} = 0.025$, $\beta = 15°$, and $\theta^* = 0°$.

values. This is very much expected as the tether drag reduces the overall aerodynamic efficiency, and the side-slip angle reduces the wind flow available to the kite.

Figure 2.11 presents the numerical results for a CKPS with the same system parameters

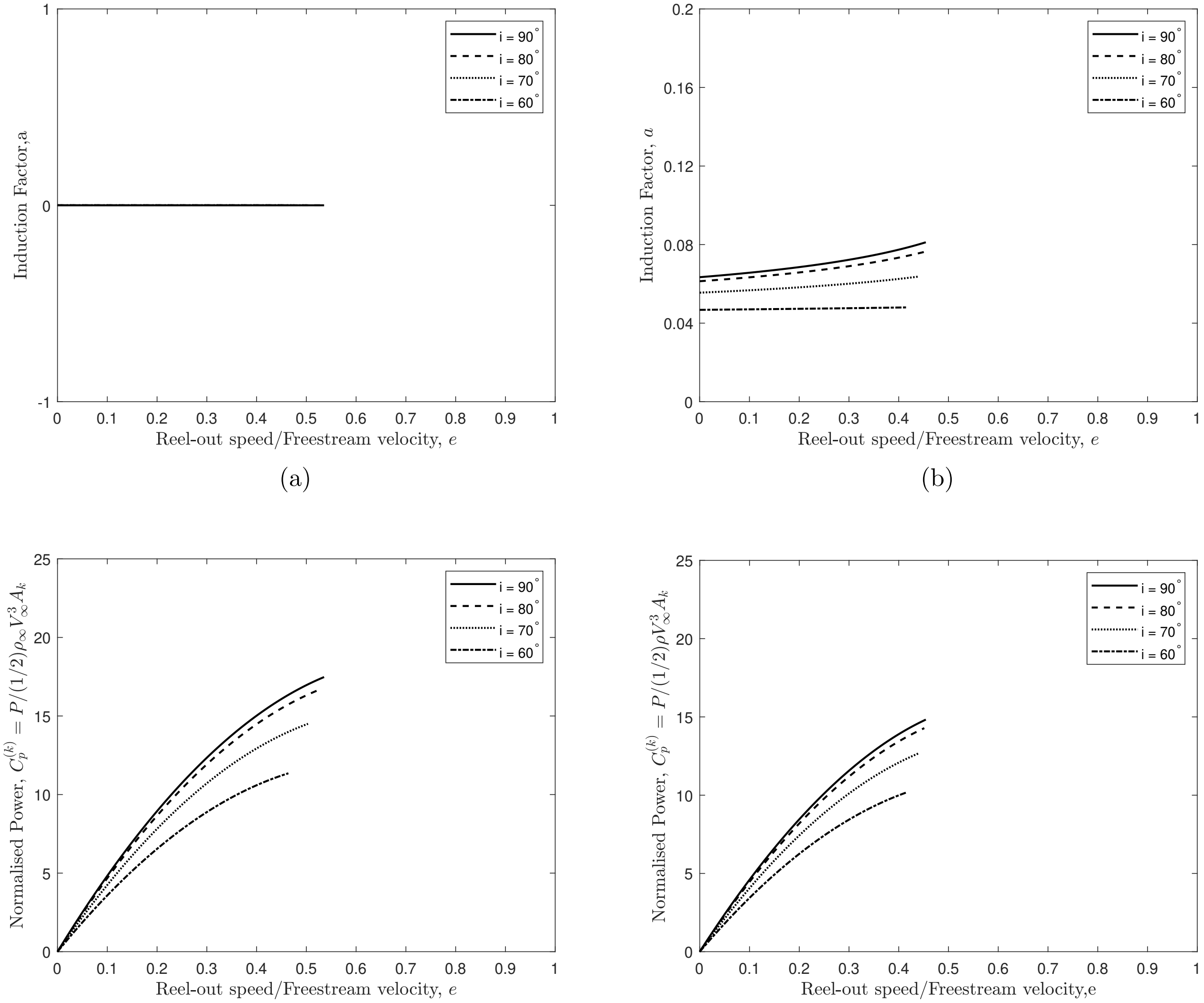

(a) (b)

(c) (d)

Figure 2.11: Plots showing the variation of (a,b) the induction factor a, and (c,d) the kite-area-normalised lift power coefficient, $C_p^{(k)} = P/(1/2)\rho V_\infty^3 A_k$, as a function of the reel-out ratio, e, for different incidence angles i (solid line: $i = 90°$, dashed line: $i = 80°$, dotted line: $i = 70°$, dash-dotted line: $i = 60°$) from aerodynamic model 1: (a,c) $\sigma = 0$, and (b,d) $\sigma = 0.0048$. The kite is a uniform wing of the aspect ratio =14.5 and SD7032 airfoil sections; also, $\lambda_R = 7.28$, $C_{D_T} = 0.025$, $\beta = 15°$, and $\theta^* = 0°$.

as those in Figures 2.8 and 2.10, but with this difference that the kite has the more modern SD7032 airfoil section instead of Clark Y airfoil considered previously.[3] When comparing

---

[3] SD7032 airfoil was designed by Selig and Donovan [71] and is considered as a low-speed airfoil. It is

the induction factor and power coefficient curves shown in Figure 2.11 (for SD7032) with those in Figure 2.10 (for Clark Y), one can see that they follow generally similar trends. Nevertheless, as seen, for the given system parameters, for both zero- and non-zero solidity factors, the kite with SD7032 airfoil could potentially produce slightly more power than the kite with Clark Y airfoil.

Figure 2.12 shows the variation of (a,b) the kite-area-normalised reel-out power $C_p^{(k)}$, and (c,d) the kite-area-normalised total power $C_{PT}^{(k)}$ as a function of e, obtained from aerodynamic model 2 for a kite of a rectangular planform with $= 14.5$ and Clark Y airfoil sections; also, $\lambda_R = 7.28$, $C_{D_T} = 0$, and $\beta = \theta^* = 0°$. The plots have been shown for (a,c) $\sigma = 0$, and (b,d) $\sigma = 0.0048$. As discussed in Section 2.2.4, aerodynamic model 2 assumes that the steady-state motion of the kite is achieved by extracting a torque power due to excessive aerodynamic forces in the flight direction. Thus, the total power will be the sum of the reel-out power and the torque power.

Comparison between the reel-out power coefficients shown in Figure 2.12 (a,b) and those in Figure 2.8 (c,d) indicates only slight differences between predictions of the two models. This appears reasonable as both models were built based on the same steady-state assumption. Figure 2.12 (c,d) shows that the kite-area-normalised total power is maximized at $e = 0$ where the reel-out power is zero and the total power is only due to the torque power. As e is increased above zero, the total power coefficient decays almost linearly with e, in most cases. On the other hand, as e is increased, the contribution of the reel-out power to the total power gradually increases, and it becomes the only contribution to the total power at higher values of e. It is interesting to see from the curves for different values of σ and i that the maximum torque power is almost two times the maximum reel-out power. This is, however, with the assumption that the two systems (i.e. one in the torque power mode and the other

---

commonly used for sailplanes and was also used by TwingTec for one of their crosswind kite prototypes [72].

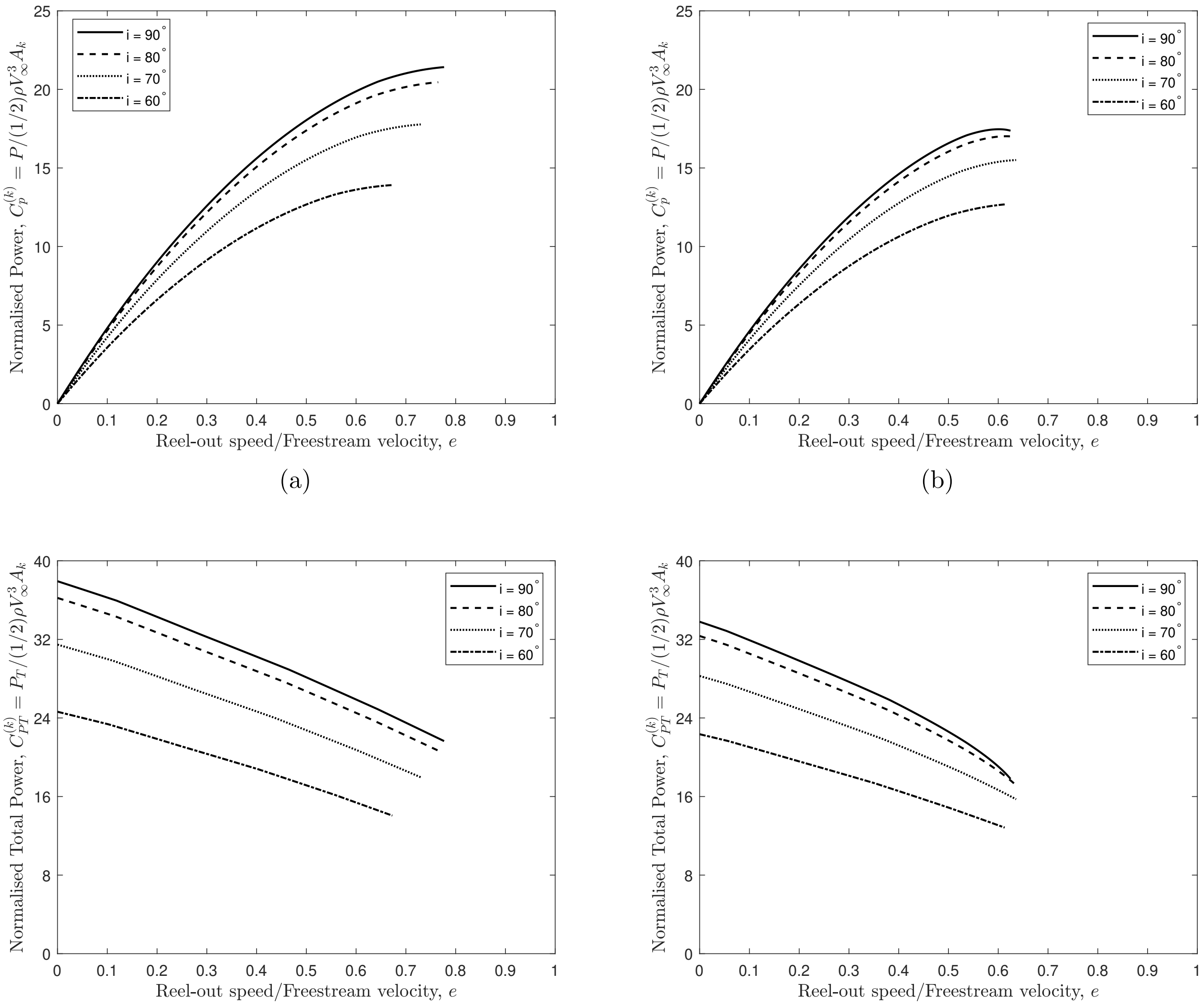

(a) (b)

(c) (d)

Figure 2.12: Plots showing the variation of (a,b) the kite-area-normalised lift (or reel-out) power coefficient, $C_p^{(k)} = P/(1/2)\rho V_\infty^3 A_k$, and (c,d) the kite-area-normalised total power coefficient $C_{PT}^{(k)} = P_T/(1/2)\rho V_\infty^3 A_k$, as a function of the reel-out ratio, e, for different incidence angles i (solid line: $i = 90°$, dashed line: $i = 80°$, dotted line: $i = 70°$, dash-dotted line: $i = 60°$) from aerodynamic model 2: (a,c) $\sigma = 0$, and (b,d) $\sigma = 0.0048$. The kite is a uniform wing of the aspect ratio =14.5 and Clark Y airfoil sections; also, $\lambda_R = 7.32$, $C_{D_T} = 0$, and $\beta = \theta^* = 0°$.

in the reel-out power mode) have the same operational and aerodynamic parameters, such as solidity factor and crosswind speed, which may not be practically feasible or desirable. A similar result was found by Kheiri et al. [1] when comparing the potential for a drag mode

CKPS with that for a lift mode system, but when the two systems have the same pre-defined aerodynamic coefficients.

Figure 2.13 shows the variation of (a) the induction factor a, (b) the induction factor $\tilde{a}$, (c) the kite-area-normalised (reel-out) power $C_p^{(k)}$, and (d) the swept-area-normalised power $C_p^{(s)}$, as a function of the dimensionless radial distance which is defined as r/r_o, r being the local radial distance from the rotation axis and r_o the radial distance of the furthest tip of the kite (see Section 2.2.3). The results are for a kite of the rectangular planform of $= 14.5$ and Clark Y airfoil sections, flying in the $Re \simeq 22 \times 10^6$ flow regime; also, $\sigma = 0.0048$, $e = 1/3$, $i = 90°$, and $\beta = \theta^* = 0°$.

Four different sets of results have been shown in Figure 2.13 plots. The CFD results (solid line) were obtained by post-processing data from a CFD simulation; please refer to Appendix C for details about the CFD simulation. The other three sets of results, i.e. '2D polars' (dashed line), '3D polar (Exp.)' (dotted line), and '3D polars' (dash-dotted line) were obtained using the aerodynamic model 2. The 2D polars results refer to those obtained using the Clark Y airfoil data with no consideration of the kite aspect ratio whereas the 3D polars refer to those from the airfoil data 'corrected' via Prandtl's equation for the finite aspect ratio effects. The airfoil aerodynamic data were obtained for different values of Re using the XFLR5 program.[4] The 3D polar (Exp.) results refer to those obtained using experimental data of Silverstein [70], corrected here for $= 14.5$.

As seen from the plots in Figure 2.13, the induction factor and power coefficient have similar spanwise distributions whether they are obtained computationally or theoretically. In particular, based on the CFD results, the induction factor and the power coefficient increase non-linearly with r/r_o within the inner tip region ($0.66 \leq r/r_o \leq 0.72$) of the kite; the increase becomes nearly linear over the inboard region ($0.72 \leq r/r_o \leq 0.92$); this is followed

---

[4] http://www.xflr5.tech/xflr5.htm

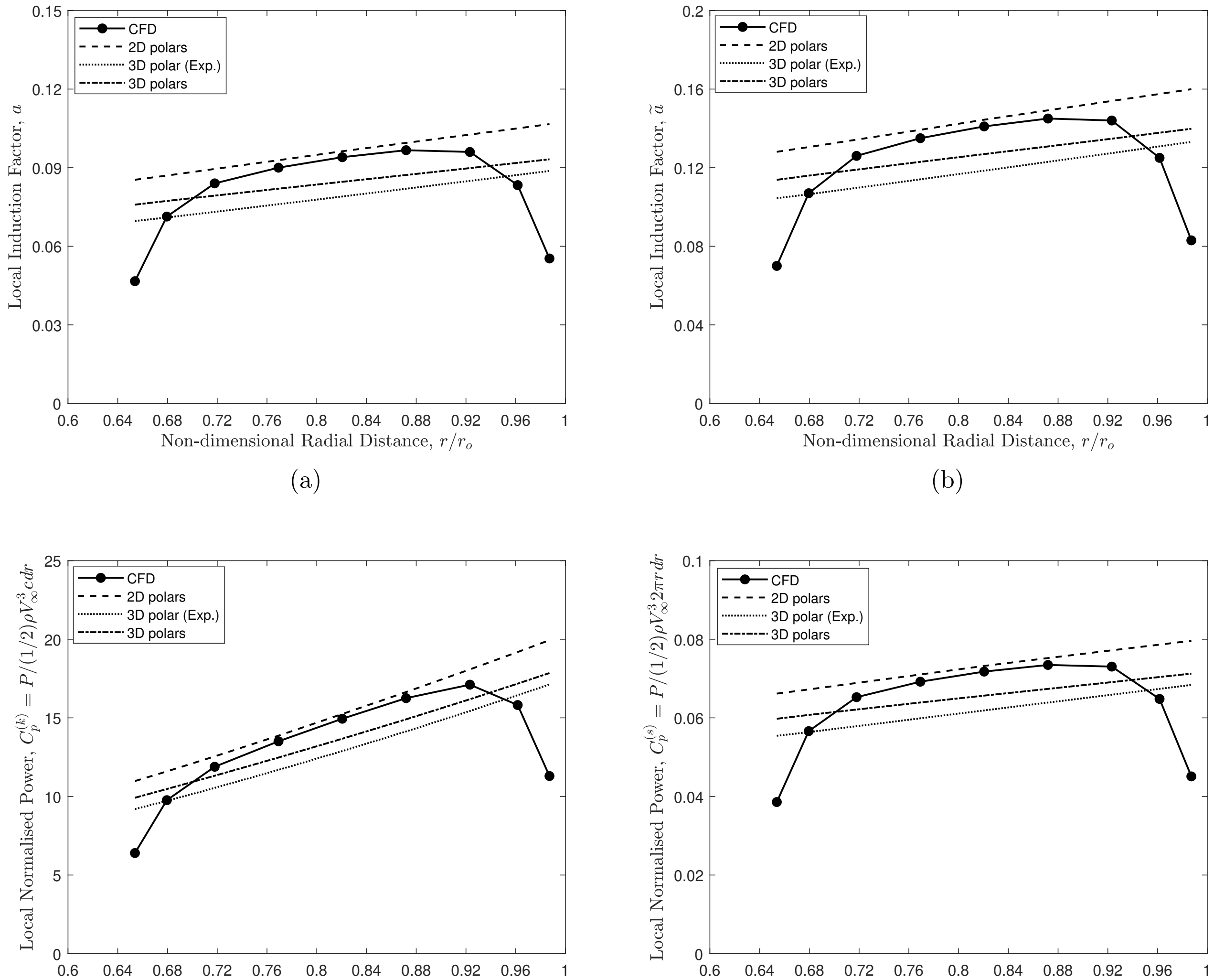

(a)

(b)

(c)

(d)

Figure 2.13: Plots showing the variation of (a) the induction factor a, (b) the induction factor $\tilde{a}$, (c) the local kite-area-normalised lift power coefficient, $C_p^{(k)} = P/(1/2)\rho V_\infty^3 c dr$, and (d) the local swept-area-normalised lift power coefficient, $C_p^{(s)} = P/(1/2)\rho V_\infty^3 2\pi r\, dr$, as a function of the dimensionless radial distance r/r_o, r and r_o being, respectively, the local radial distance and the radial distance of the furthest tip of the kite from the rotation axis. Four sets of results were shown: CFD (solid line with marker), aerodynamic model 2 with 2D polars (dashed line), aerodynamic model 2 with 3D polar (Exp.) (dotted line), and aerodynamic model 2 with 3D polars (dash-dotted line). The kite is a uniform wing of the aspect ratio =14.5 and Clark Y airfoil sections; also, σ = 0.0048, $\lambda_R = 7.32$, $e = 1/3$, $i = 90°$, $C_{D_T} = 0$, and $\beta = \theta^* = 0°$.

Table 2.4: Comparison of the average induction factors (a and $\tilde{a}$), swept-area-normalised power coefficient, $C_p^{(s)}$, kite-area-normalised power coefficient, $C_p^{(k)}$, and the kite-area-normalised thrust coefficient, $C_T^{(k)}$, obtained computationally [8] and from aerodynamic model 2 (i.e. 2D polars, 3D polar (Exp.), and 3D polars) for a kite of a uniform planform and of the aspect ratio = 14.5 and Clark Y airfoil sections; also, $\sigma = 0.0048$, $\lambda_R = 7.28$, $e = 1/3$, $i = 90°$, $C_{D_T} = 0$, and $\beta = \theta^* = 0°$. The values in the parentheses are errors relative to the CFD results.

	CFD [8]	2D polars	3D polar (Exp.)	3D polars
a	0.085	0.097 (14.4%)	0.080 (5.8%)	0.085 (0.6%)
$\tilde{a}$	0.127	0.145 (14.4%)	0.120 (5.8%)	0.128 (0.6%)
$C_p^{(s)}$	0.065	0.074 (12.4%)	0.062 (4.7%)	0.066 (0.9%)
$C_p^{(k)}$	13.623	15.317 (12.4%)	12.989 (4.7%)	13.750 (0.9%)
$C_T^{(k)}$	40.870	45.950 (12.4%)	38.967 (4.7%)	41.250 (0.9%)

by a non-linear drop in the vicinity of the outer tip ($0.92 \leq r/r_o \leq 0.98$) of the kite. Based on the theoretical results, however, both the induction factor and power coefficient increase almost linearly from the inner tip towards the outer tip of the kite. As seen, the slope of the theoretical lines are similar to each other and to that of the computational distribution in the inboard region.

The quantitative agreement between 2D polars and CFD results within the kite inboard region is surprisingly good although it is poor when the values averaged over the entire kite/swept area are compared; the maximum relative error is around 14%. On the other hand, results produced using 3D polars and 3D polar (Exp.) show much better quantitative agreement with CFD results when the average induction factor and power coefficient values are compared; the maximum relative errors are about 1% and 6%, respectively; see Table 2.4 for more details. The superiority of 3D polars over 2D polars for the strip flow load predictions over a finite-aspect-ratio wing has long been known; see, for example, [73, Chapter 8]; also, [74, Chapter 4].

Apart from the quality of the quantitative agreement between theoretical and computational results, one may notice a major discrepancy between the distributions predicted computationally and theoretically within the inner and outer tip regions. The discrepancy may be linked to "tip losses" which arise because, in real wind energy harvesting devices, such as wind turbines, there is always a finite number of lifting surfaces (e.g. blades) that rotate over the swept area. These losses are normally dealt with separately from the losses due to finite aspect-ratio lifting surfaces [75]. These losses are not originally accounted for in the BEM-based models, including the one used in the present paper, in which it is assumed that the actuator disc has infinite number of blades. There have been several attempts to include the effects of tip-losses for wind turbines and propellers; some early works are those by Prandtl [76], Goldstein [77], and Glauert [78]; for more details, see Refs. [54, 55, 79]. The incorporation of the effects of tip-losses into the present paper model is deferred to a future study. Also, further CFD simulations are warranted to be used for comparison purposes to ensure that the analytical model can consistently predict the performance of CKPSs with high accuracy.

2.4 Conclusion

Two novel aerodynamic models were presented, which can be used for predicting the performance of a crosswind kite flying steadily on a circular path. The BEM theory based on Glauert's equation formed the backbone of the equations developed in the present paper. Unlike previous models found in the literature, the new models include the effects of incidence angle, side-slip angle, and tether drag in the formulations for the induction factor and power coefficient. Aerodynamic model 1 was developed for performance prediction of pumping/lift mode kites whereas aerodynamic model 2 is suitable for either pumping mode, drag mode or the combination of the two, which the authors would like to call the hybrid mode. In addition, aerodynamic model 2 can also be used for non-uniform inflow problems.

Numerical results obtained using aerodynamic model 1 for CKPSs with pre-defined aerodynamic coefficients showed that the maximum kite-area-normalised power coefficient is achieved when the solidity factor is zero and decreases as the solidity factor is increased. It was found that the optimal reel-out ratio (i.e. the reel-out ratio corresponding to the maximum power coefficient) shifts towards lower values as the incidence angle is decreased and the side-slip angle is increased. It was also found that the power coefficient generally decreases as the incidence angle is decreased (i.e. the elevation angle is increased) and the side-slip angle is increased. The induction factor, on the other hand, was found to be increasing with the solidity factor and decreasing with the reel-out ratio.

Some numerical results were obtained for CKPSs with Clark Y airfoil sections and for a given crosswind speed ratio, zero side-slip angle and zero tether drag coefficient using aerodynamic model 1. For the kite with non-zero solidity factor, it was shown that the induction factor generally increases as the reel-out ratio and incidence angle are increased. The power coefficient was found to be increasing as the reel-out ratio and the incidence angle were increased; the optimal reel-out ratio was found to be weakly dependent on the incidence angle. On the other hand, for the zero-solidity kite system, the induction factor remained zero for any reel-out ratio and every incidence angle. The optimal reel-out ratio was found to occur at higher values as the incidence angle was increased.

Numerical results for the kite systems with a non-zero side-slip angle and tether drag coefficient were found to follow generally similar trends as those for the systems with zero side-slip and tether drag. The maximum power coefficient, however, was found to decrease in magnitude and to occur at lower values of reel-out ratio when the side-slip angle and tether drag coefficient were non-zero. Similar trends were found for kites with the SD7032 airfoil section although power coefficients were slightly higher compared to those for kites with the Clark Y airfoil section.

Some numerical results were also obtained with aerodynamic model 2, assuming uniform inflow, for the same kite systems analysed with aerodynamic model 1. No key difference was noticed between the reel-out power coefficient variations predicted by the two models. On the other hand, the results suggested that potentially more wind power may be harnessed if the kite operates in purely drag (or torque) mode or alternatively in hybrid lift-drag mode instead of purely lift mode. This is subject to the assumption that some key operational parameters, such as solidity factor and crosswind speed remain the same. This is an important finding, but more in-depth analyses by considering other system configurations are warranted before making a generalization.

Finally, some numerical results were obtained for a kite in the straight downwind configuration with aerodynamic model 2 and with the non-uniform inflow assumption. Three different sets of tabulated aerodynamic data were used in the solution process, and numerical results were compared with CFD results. The results for uncorrected 2D airfoil data were found to be in a very good agreement with CFD results over the inboard region of the kite span while the two sets were noticeably different (both qualitatively and quantitatively) over the outboard regions. The average numerical values obtained via corrected wing data were found to be in a very good agreement with the CFD results. Nevertheless, more CFD results for various kite systems are desirable for further validating the results from aerodynamic model 2.

Chapter 3

Quasi-steady aerodynamic model of an aerostatic power system

This chapter presents a numerical model for predicting the quasi-steady aerodynamic performance of an aerostatic power system (APS), in which the induced velocity is treated as a function of radius and azimuthal angle of the blade. The model is developed based on quasi-steady blade element momentum theory. The wake rotation and the tangential induced velocity are considered. The aerodynamic model is validated against a 3-bladed yawed wind turbine rotor and a 2-bladed autogyro rotor. Results for optimum tip speed ratio, variation of thrust and power during rotation and other performance coefficients are presented. Although the aerodynamic model is developed to predict on-board power generation of an autogyro, it can be extended to yawed turbines and propellers. It could also predict ground based or a combination of on-board and ground based power generation if required.

3.1 Definitions and preliminaries

The aerostatic power system (APS) under consideration is an autogyro consisting of four similar rotors mounted on an airframe tethered to the ground as shown in Figure 3.1. For simplicity, it is assumed that the aerodynamic performance parameters of the system would be equal to the number of rotors, N_r, times the aerodynamic performance parameters of one rotor. The representative rotor is identical to the other rotors but assumed to be fixed at the centre of gravity of APS and will be representative of theory and formulations explained here. The axis about which the rotor rotates is referred to as the rotation axis. The airframe considered for this work is assumed to lie in a plane and the rotation axes of the rotors are perpendicular to it. The area swept by the rotor blades will lie on a plane that is perpendicular to the rotation axis and will be in the shape of a disc, i.e there is no coning in the rotor. The sign convention for the pitch follows wind turbine convention and is positive when pitched down. The wind will be directed to the pressure side of the rotor. The rotor is fixed in space using right handed Cartesian co-ordinate systems. The wind velocity V_∞ is

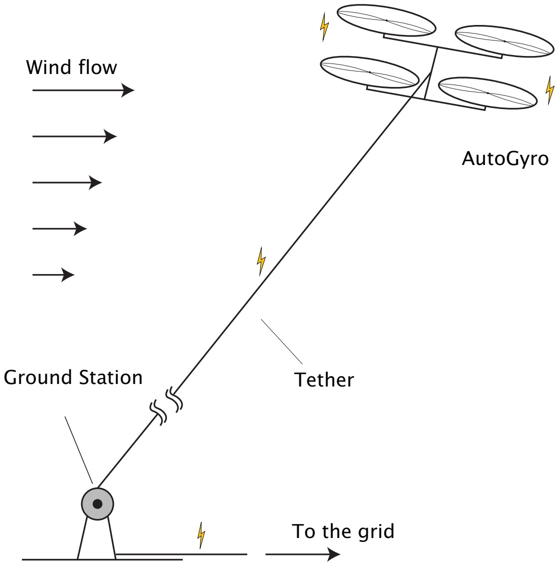

Figure 3.1: Figure showing a tethered aerostatic power system (APS).

assumed to follow a steady shear profile in the X-direction of the inertial co-ordinate system for results presented in this work. However, the wind velocity can be steady, unsteady or uniform depending on the requirement of analysis.

3.2 Dynamics and control

Although the focus of this work is the prediction of aerodynamic performance, to justify the feasibility of the chosen configuration, the control of dynamics is explained in a simplified manner [43]. The APS is capable of pitch, roll and yaw by changing the collective pitch. Even though cyclic pitch allows to smooth the force and torque outputs, it is neglected to simplify the analysis. Hence, in this work pitch refers to the collective pitch. The APS has four rotors; the adjacent rotors rotate in the opposite directions and the opposite rotors rotate in the same direction.

- Thrust can be increased by lowering the pitch and vice versa.
- In general, torque can be increased by increasing pitch and vice versa.
- Roll is controlled by changing pitch of right and left pairs of rotors.
- Pitch is controlled by changing pitch of pair of rotors at front and back.
- Yaw control is by changing pitch on pairs of opposing rotors

3.3 The co-ordinate systems

To apply the aerodynamic equations and to find the position of APS and it's components in space, various co-ordinate systems are defined. All the co-ordinate systems defined in this work are right handed Cartesian co-ordinate systems. The angle of rotation is positive when the rotation of co-ordinate systems are anticlockwise and negative when clockwise. This section discusses various co-ordinate systems used.

3.3.1 Inertial co-ordinate system

The inertial co-ordinate system, $O_e : \hat{i}_e, \hat{j}_e, \hat{k}_e$, shown in Figure 3.2, is fixed to the earth with the Y-axis pointing up. The X-axis and Z-axis are perpendicular to each other and the X-axis points right. The wind velocity is defined in the inertial co-ordinate system along the X-axis.

3.3.2 Body co-ordinate systems

There are multiple body co-ordinate systems defined for the APS. The body co-ordinate system $O_i : \hat{i}_i, \hat{j}_i, \hat{k}_i$, represents the rotor rotation by an angle i about the Z-axis of O_e, as shown in the Figure 3.2 and Figure 3.3(a). The angle i is referred to as the incidence angle and is complementary to the angle tether makes with the horizontal. It defines the inclination of the rotor with respect to the X-axis of O_e. The body co-ordinate system $O_\beta : \hat{i}_\beta, \hat{j}_\beta, \hat{k}_\beta$, is obtained by the rotation of the rotor about the X-axis of O_i, as shown in

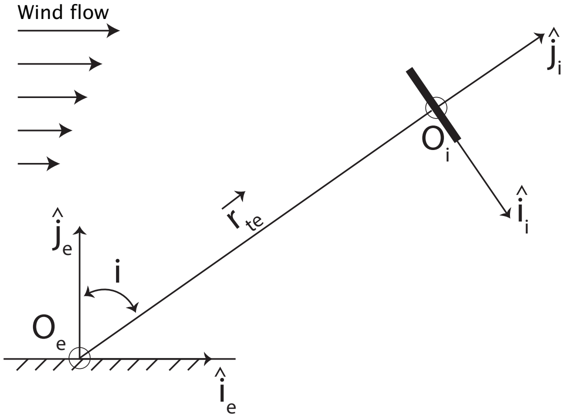

Figure 3.2: Figure showing the inertial co-ordinate system.

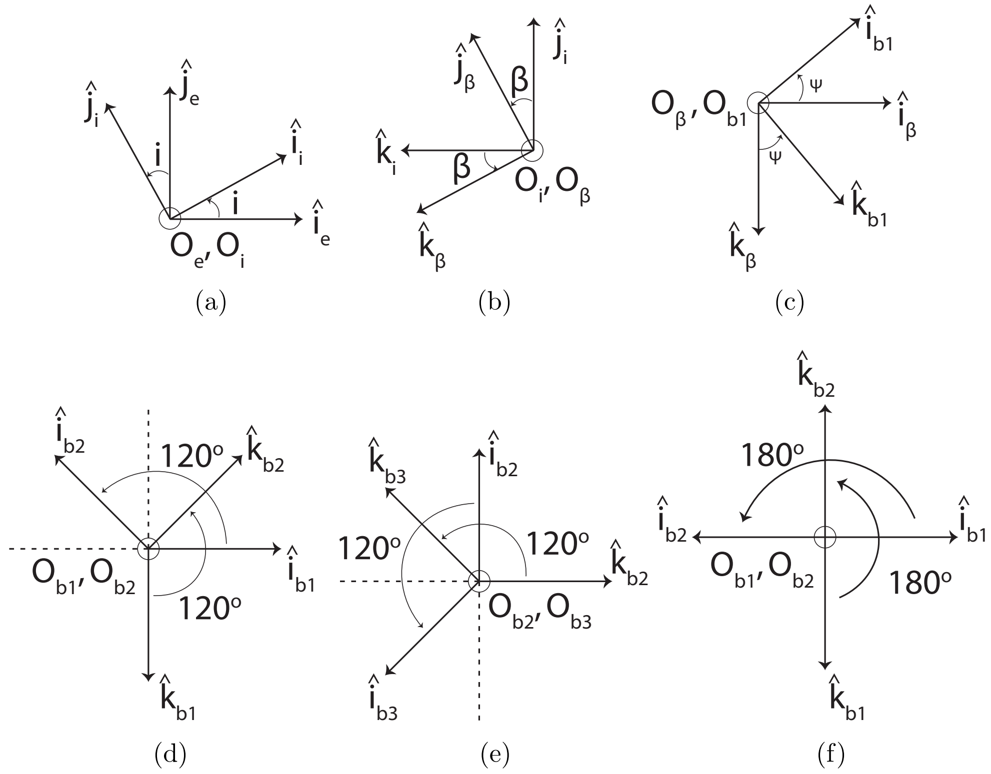

(a) (b) (c)

(d) (e) (f)

Figure 3.3: Figure showing transformation of one co-ordinate system into another by rotation; (a) O_e to O_i rotation, (b) O_i to O_β rotation, (c) O_β to O_{b1} rotation (d) O_{b1} to O_{b2} rotation for a 3-bladed rotor, (e) O_{b2} to O_{b3} rotation for a 3-bladed rotor and (f) O_{b1} to O_{b2} rotation for a 2-bladed rotor.

Figure 3.3(b), by an angle β which is called the side-slip angle. The side-slip angle defines inclination of the rotor with the Z-axis of O_e. Each blade is assigned a body co-ordinate system such that the blades are aligned along the X-axis of the respective systems. Hence, if there are three blades, three body co-ordinate systems $O_{b1} : \hat{i}_{b1}, \hat{j}_{b1}, \hat{k}_{b1}$, $O_{b2} : \hat{i}_{b2}, \hat{j}_{b2}, \hat{k}_{b2}$ and $O_{b3} : \hat{i}_{b3}, \hat{j}_{b3}, \hat{k}_{b3}$ are defined. O_{b1} is set as the reference to define the azimuth angle, Ψ of the blades, which defines rotation of the blades about the Y-axis of O_β as shown in Figure 3.3(c). Each of these co-ordinate systems will have their Y-axis aligned with that of the O_β. If there are three blades, the co-ordinate systems O_{b1}, O_{b2} and O_{b3} are separated by 120°. In the case of a two-bladed rotor, O_{b1} and O_{b2} are separated by 180°.

3.4 Co-ordinate transformations

The calculations are easier if certain vectors are expressed in a particular co-ordinate system. A vector, $\overrightarrow{W_A} = (X_A, Y_A, Z_A)$ in a co-ordinate system O_A, can be represented in another co-ordinate system, O_B as $\overrightarrow{W_B} = (X_B, Y_B, Z_B)$ by using a transformation matrix T_{AB}, where $\overrightarrow{W_B} = T_{AB}\overrightarrow{W_A}$. The transformation matrix from O_B to O_A will simply be T_{AB}^T. The co-ordinate transformations used in this work follows conventions of Schaub et al. [80].

The rotation from O_e to O_i is shown in Figure 3.3(a) and the transformation matrix is given as

$$T_{ei} = \begin{bmatrix} \cos i & \sin i & 0 \\ -\sin i & \cos i & 0 \\ 0 & 0 & 1 \end{bmatrix}. \tag{3.1}$$

The rotation from O_i to O_β is shown in Figure 3.3(b) and the transformation matrix can be given by

$$T_{i\beta} = \begin{bmatrix} 1 & 0 & 0 \\ 0 & \cos\beta & \sin\beta \\ 0 & -\sin\beta & \cos\beta \end{bmatrix}. \tag{3.2}$$

The rotation from O_β to O_{b1} is shown in Figure 3.3(c) and the transformation matrix is given by

$$T_{\beta b_1} = \begin{bmatrix} \cos\Psi & 0 & -\sin\Psi \\ 0 & 1 & 0 \\ \sin\Psi & 0 & \cos\Psi \end{bmatrix}. \tag{3.3}$$

Considering three blades, rotation from O_{b1} to O_{b2} is shown in Figure 3.3(d) and the transformation matrix is given as

$$T_{b_1b_2} = \begin{bmatrix} -\sin 30^\circ & 0 & -\cos 30^\circ \\ 0 & 1 & 0 \\ \cos 30^\circ & 0 & -\sin 30^\circ \end{bmatrix}, \tag{3.4}$$

and the rotation from O_{b2} to O_{b3} is shown in Figure 3.3(e) and the transformation matrix is given by

$$T_{b_2b_3} = \begin{bmatrix} -\sin 30^\circ & 0 & -\cos 30^\circ \\ 0 & 1 & 0 \\ \cos 30^\circ & 0 & -\sin 30^\circ \end{bmatrix}. \tag{3.5}$$

Considering only two blades, rotation from O_{b1} to O_{b2} is shown in Figure 3.3(f) and the transformation matrix from is

$$T_{b_1b_2} = \begin{bmatrix} -1 & 0 & 0 \\ 0 & 1 & 0 \\ 0 & 0 & -1 \end{bmatrix}. \tag{3.6}$$

3.5 Position and velocity vectors

If r is the radial distance of a blade element from the centre of the rotor, then in the respective blade co-ordinate system, the vector is expressed as

$$\overrightarrow{r_b} = \begin{bmatrix} r & 0 & 0 \end{bmatrix}^T. \tag{3.7}$$

Hence a point at a distance of r on blade 3 is expressed in O_e as

$$\overrightarrow{r_{be}} = T_{ei}^T T_{i\beta}^T T_{\beta b_1}^T T_{b_1 b_2}^T T_{b_2 b_3}^T \overrightarrow{r_{b3}}. \tag{3.8}$$

A point at a distance of r on blade 2 is expressed in O_e as

$$\overrightarrow{r_{be}} = T_{ei}^T T_{i\beta}^T T_{\beta b_1}^T T_{b_1 b_2}^T \overrightarrow{r_{b2}}. \tag{3.9}$$

A point at a distance of r on blade 1 is expressed in O_e as

$$\overrightarrow{r_{be}} = T_{ei}^T T_{i\beta}^T T_{\beta b_1}^T \overrightarrow{r_{b1}}. \tag{3.10}$$

If $\overrightarrow{r_{te}}$ is the position vector of the end point of the tether connected to the centre of gravity of the APS (or centre of the equivalent rotor), as shown in Figure 3.2, the position vector of a blade element in O_e is

$$\overrightarrow{r_{pe}} = \overrightarrow{r_{te}} + \overrightarrow{r_{be}}. \tag{3.11}$$

When a non-uniform wind profile is used, the position vector of each blade element, $\overrightarrow{r_{pe}}$ is used in the calculation of the respective wind velocity. Since the wind velocity is defined in O_e, it is to be converted to respective blade co-ordinate system for the calculation of aerodynamic forces. If $\overrightarrow{V_{we}}$ is the wind velocity vector defined in O_e for the blade element, then the wind velocity in body co-ordinate system O_{b3} for blade 3 would be

$$\overrightarrow{V_{wb}} = T_{b_2 b_3} T_{b_1 b_2} T_{\beta b_1} T_{i\beta} T_{ei} \overrightarrow{V_{we}}. \tag{3.12}$$

For blade 2, in O_{b2}, the wind velocity would be

$$\overrightarrow{V_{wb}} = T_{b_1 b_2} T_{\beta b_1} T_{i\beta} T_{ei} \overrightarrow{V_{we}}. \tag{3.13}$$

For blade 1, in O_{b1}, the wind velocity would be

$$\overrightarrow{V_{wb}} = T_{\beta b_1} T_{i\beta} T_{ei} \overrightarrow{V_{we}}. \tag{3.14}$$

3.6 Wind model

The non-uniform wind velocity is modelled using the power law [81]

$$V_Z = V_{Z_r} (\frac{Z}{Z_r})^{\alpha}, \tag{3.15}$$

where V_Z is the wind velocity at height Z above the ground level, Z_r is the reference height and α is the wind shear exponent, which is typically 0.2 [81]. For this study, $Z_r = 10$ m and $V_{Z_r} = 6$ m/s were taken.

The wind velocity vector is given as

$$\vec{V}_w = V_Z \hat{i}_e. \tag{3.16}$$

3.7 Aerodynamic model

The averaged forces and power produced by an APS can be found using the blade element momentum (BEM) theory discussed in Chapter 2. However, an unsteady/quasi-steady BEM is required to accurately predict the aeroelastic behaviour of the APS because of the unsteady nature of wind from atmospheric turbulence, couple dynamics of airborne module with that of tether and wind shear.

The aerodynamic forces on the APS are estimated using the quasi-steady (BEM) theory. Quasi-steady BEM like the conventional BEM theory assumes that the flow takes place in independent stream tubes. In principle, BEM equates axial load and torque predicted by the momentum theory with those predicted by the blade element theory to find the unknown angle of attack and induced velocity.

Momentum theory employs the concept of an actuator disc that represents turbine as a infinitesimally thin disc with infinite number of blades allowing aerodynamic analysis without the requirement of a specific design. The air that passes through the disc experiences a momentum exchange. Since the mass flow rate is constant along the stream tube and since the change in cross sectional area across the disc is negligibly small, the momentum change across the disc is taken into account by superimposing an induced velocity, v, on the freestream velocity. In principle, the momentum theory follows Newton's second law of motion and finds the momentum change for a given loading on the disc. The loading predicted by the blade element theory is based on the strip flow theory. Thus, the two theories combined as the BEM theory give two equations to find the two unknowns, angle of attack and induced velocity. For further details, the reader can refer to chapter 2, Burton et al. [54] and Sorensen et al. [55] for conventional BEM theory and Hansen et al. [82] for unsteady/quasi-steady BEM. If a blade element is considered, it's velocity triangle will be as shown in Figure 3.4. The formulations presented below are in the respective blade co-ordinate system of the element. The relative velocity vector on the element, $\overrightarrow{V_{rel}} = (V_{Xrel}, V_{Yrel}, V_{Zrel})$ is given by

$$\overrightarrow{V_{rel}} = \overrightarrow{V_{wb}} + \overrightarrow{V_{rot}} + \overrightarrow{v}, \tag{3.17}$$

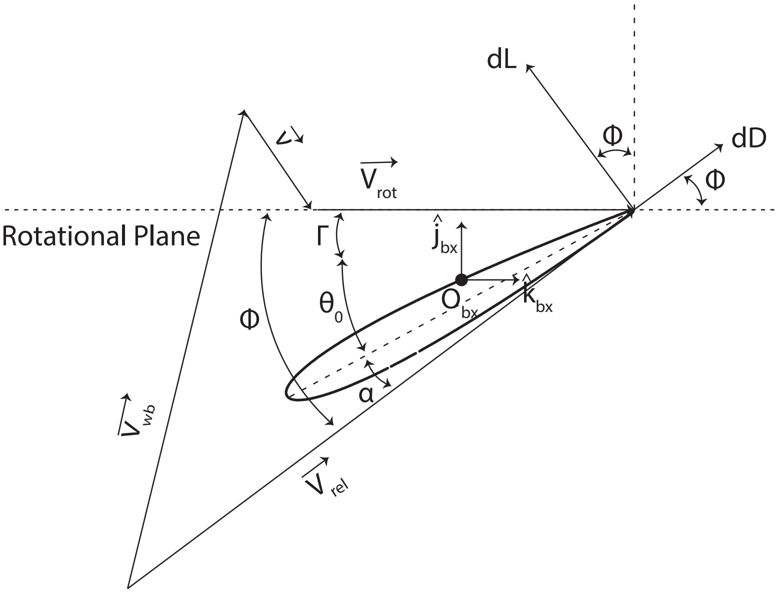

Figure 3.4: Figure showing the velocity triangle for blade element.

where $\overrightarrow{v}$ is the induced velocity, $\overrightarrow{V_{rot}}$ is the rotational velocity given by

$$\overrightarrow{V_{rot}} = \begin{bmatrix} 0 & 0 & r\Omega \end{bmatrix}^T, \tag{3.18}$$

where r is radial distance of the element and Ω, the angular velocity. The spanwise component of the relative velocity vector (i.e., V_{Xrel}) is neglected.

The angle of attack of the element is

$$\alpha = \Phi - (\Gamma + \theta_0 + \alpha_i), \tag{3.19}$$

where Γ is the twist of the blade, θ_0 is the collective pitch, α_i is the induced angle of attack. For simplicity, direct incorporation of α_i is neglected in this work. The inflow angle, Φ, for the element can be found as

$$\Phi = \tan^{-1}\left(\frac{\overrightarrow{V_{Yrel}}}{\overrightarrow{V_{Zrel}}}\right). \tag{3.20}$$

The lift force acting on the element is given by

$$\mathrm{d}L = \frac{1}{2}\rho_\infty|\overrightarrow{V_{rel}}|^2 c\mathrm{d}r c_l, \tag{3.21}$$

where ρ_∞ is the freestream density, c is the chord length of the element, dr is the width of the element and c_l is the coefficient of lift of the element. The drag force acting on the element is

$$\mathrm{d}D = \frac{1}{2}\rho_\infty|\overrightarrow{V_{rel}}|^2 c\mathrm{d}r c_d, \tag{3.22}$$

where c_d is the coefficient of drag of the element.

The unit vector normal to the rotor and in the direction of thrust acting on fluid is give by

$$n = \begin{bmatrix} 0 & -1 & 0 \end{bmatrix}^T . \tag{3.23}$$

The magnitude of the wake velocity for the blade element is given by

$$|\overrightarrow{V'}| = |\overrightarrow{V_{wb}} + n(n.\overrightarrow{v})|. \tag{3.24}$$

The normal component of the induced velocity at the element is

$$v_n = n.\overrightarrow{v}. \tag{3.25}$$

The tangential component of the induced velocity at the element is

$$v_t = \hat{k}_{bx}.\overrightarrow{v}. \tag{3.26}$$

As per [82] the normal component of the induced velocity at the element from momentum theory is

$$v_n = \frac{-N_b \mathrm{d}L\cos(\Phi)}{4\pi\rho r F|\overrightarrow{V'}|}, \tag{3.27}$$

where N_b is the number of blades on the rotor; F is the Prandtl's tip loss factor for the element of blade x, which is given as [54]

$$\begin{aligned} f &= \frac{N_b}{2}\frac{R-r}{r\sin(\Phi)}, \\ F &= \frac{2}{\pi}\cos^{-1}(e^{-f}), \end{aligned} \tag{3.28}$$

where, R is the radius of the rotor. The tangential component of the induced velocity at the element from momentum theory consideration is written as

$$v_t = \frac{N_b \mathrm{d}L\sin(\Phi)}{4\pi\rho r F|\overrightarrow{V'}|}. \tag{3.29}$$

The normal force coefficient from the element is,

$$C_n = c_l\cos(\Phi) + c_d\sin(\Phi). \tag{3.30}$$

The tangential force coefficient from the element is,

$$C_t = c_l\sin(\Phi) - c_d\cos(\Phi). \tag{3.31}$$

The thrust from the element is

$$\mathrm{d}T = \frac{1}{2}\rho_\infty|\overrightarrow{V_{rel}}|^2 c\mathrm{d}r C_n. \tag{3.32}$$

The mechanical power from the element is

$$\mathrm{d}P = \frac{1}{2}\rho_\infty |\overrightarrow{V_{rel}}|^2 c\mathrm{d}r C_t r\Omega. \tag{3.33}$$

Tip speed ratio, λ, defined as

$$\lambda = \frac{R\Omega}{|\overrightarrow{V_w}|}, \tag{3.34}$$

is a non-dimensional parameter important in predicting optimum operational condition.

The solidity of the rotor, σ given as

$$\sigma = \frac{N_b c}{\pi R}, \tag{3.35}$$

is a non-dimensional number that gives an idea about the blade area in rotor area.

The blade is discretised into elements of width dr and the equations of quasi-steady BEM can be solved following the approach mentioned in Table 3.1 to obtain dT and dP at time

Table 3.1: Approach for solving quasi-steady BEM

Step	Task
1	Consider a guess value for induced velocities v_n and v_t, i.e. $v_{n_{guess}}$ and $v_{t_{guess}}$.
2	Find V_{rel} from (3.17) for known λ and $\overrightarrow{V}_w$ and obtain the inflow angle Φ using (3.20).
3	Obtain the angle of attack α from (3.19) for already chosen Γ and θ_0.
4	Find c_l and c_d from $c_l - \alpha$ and $c_d - \alpha$ tables for the corresponding Reynolds number.
5	Obtain dL from (3.21) and dD from (3.22).
6	Find the new v_n from (3.27) and new v_t from (3.29), i.e. $v_{n_{new}}$ and $v_{t_{new}}$
7	If $(\lvert v_{n_{guess}} - v_{n_{new}}\rvert + \lvert v_{t_{guess}} - v_{t_{new}}\rvert) > \kappa$ (κ is a very small number), then $v_{n_{guess}} = v_{n_{new}}$ and $v_{t_{guess}} = v_{t_{new}}$ and go to step 2.
8	If $(\lvert v_{n_{guess}} - v_{n_{new}}\rvert + \lvert v_{t_{guess}} - v_{t_{new}}\rvert) < \kappa$, converged values have been obtained.
9	Find dT from (3.32) and dP from (3.33).

t for each element. The summation of the elemental thrust, dT, and the elemental power, dP, along the radius of the blade provides the total thrust, T_{bx}, and power, P_{bx} for blade x. The total thrust, T and power, P of the rotor is found by adding the thrust and power of all the blades.

The coefficient of thrust is given by

$$C_T = \frac{T}{\frac{1}{2}\rho_\infty \pi R^2 |\overrightarrow{V_w}|^2}. \tag{3.36}$$

The coefficient of power is given by

$$C_P = \frac{P}{\frac{1}{2}\rho_\infty \pi R^2 |\overrightarrow{V_w}|^3}. \tag{3.37}$$

3.8 Validation

Since APS operates in windmilling mode while extracting energy, the theory presented is also applicable to a yawed wind turbine. Hence, for the validation of the theory and equations, experimental results published by Bastankhah et al. [9] on yawed wind turbines and experimental results published by Roberts et al. [7] for a potential rotor for APS are considered.

Bastankhah et al. [9] presents a study on the design and performance of miniature three-bladed horizontal-axis wind (HAWT) with a rotor diameter of 0.15 m. The study is a good candidate for validation since the thrust coefficient, C_T and power coefficient, C_P of the turbines reach 0.8 and 0.4, respectively, which are close to large scale turbines. The design details of the HAWT and the velocity profile are mentioned in [9] and [83]; the blade as well as airfoil characteristics are also given in [84] and [85]. Table 3.2 lists the values of C_T and C_P obtained experimentally and numerically for different values of the tip-speed ratio, λ, and incidence angle, i. As seen from Table 3.2, the agreement between present numerical

Table 3.2: Table showing coefficient of power, C_P, and coefficient of thrust, C_T, for different values of the tip-speed ratio, λ, and incidence angle, i; 'Exp' refers to experimental values reported in [9] while 'Num' refers to numerical values obtained using the present quasi-steady BEM.

λ	i	C_P (Exp.)	C_P (Num.)	Error (%)	C_T (Exp.)	C_T (Num.)	Error (%)
3.0	-90	0.32	0.32	0.0	0.78	0.76	2.6
	-100	0.32	0.30	6.7	0.77	0.72	6.9
	-110	0.29	0.27	7.4	0.73	0.69	5.8
	-120	0.23	0.22	4.5	0.64	0.62	3.2
3.5	-90	0.38	0.35	8.6	0.85	0.81	4.9
	-100	0.37	0.34	8.8	0.84	0.77	9.1
	-110	0.32	0.30	6.7	0.77	0.73	5.5
	-120	0.25	0.24	4.2	0.65	0.65	0.0
4.0	-90	0.37	0.35	5.7	0.88	0.83	6.0
	-100	0.35	0.34	2.9	0.85	0.79	7.6
	-110	0.29	0.30	3.3	0.73	0.75	2.7
	-120	0.22	0.23	4.3	0.61	0.67	9.0
4.5	-90	0.30	0.32	6.3	0.82	0.84	2.4
	-100	0.25	0.31	19.4	0.72	0.80	10.0
	-110	0.22	0.26	15.4	0.64	0.76	15.8
	-120	0.17	0.19	10.5	0.55	0.67	17.9

values and experimental values is quite well for $\lambda \leq 4$, where the maximum relative error is less than 10%. However, for $\lambda = 4.5$, the relative error becomes large. As mentioned by Bastankhah et al. [84], the output power measurement of the miniature turbine is difficult and the range of error bar reported for the experiment increases with increasing λ and could be the major reason for the discrepancy at higher λ.

Roberts et al. [7] provides experimental results on a twin rotor gyromill which is the system under consideration in this work. The rotor had a tip radius of 1.26 m with a solidity of 0.06 [19]. The blade was made of NACA 0012 airfoil sections with a chord length of 0.13 m. The twist of the blade is linear and is given as

$$\Gamma = \theta_1 \frac{r}{R}, \tag{3.38}$$

where θ_1 is -8°.

The results presented in this work has continued to use (3.38) for defining the blade twist. The NACA 0012 aerodynamic data from [86] was used. The collective pitch was 8°. A comparison is made by plotting the dimensionless torque as a function of the dimensionless velocity $V_\infty \cos(i)/(\Omega R)$, obtained experimentally [7] against those obtained numerically via the present quasi-steady BEM model; see Figure 3.5. As seen from the figure, the numerical results from the quasi-steady BEM model are in the best agreement with the experimental results, compared to the other models. At higher values of $V_\infty \cos(i)/(\Omega R)$ (i.e. near stall) the present numerical results predict a similar trend as the experimental results while other models show an obvious deviation. Nevertheless, there is a discrepancy between quasi-steady BEM and experimental results. One reason for such a discrepancy may be the fact that the

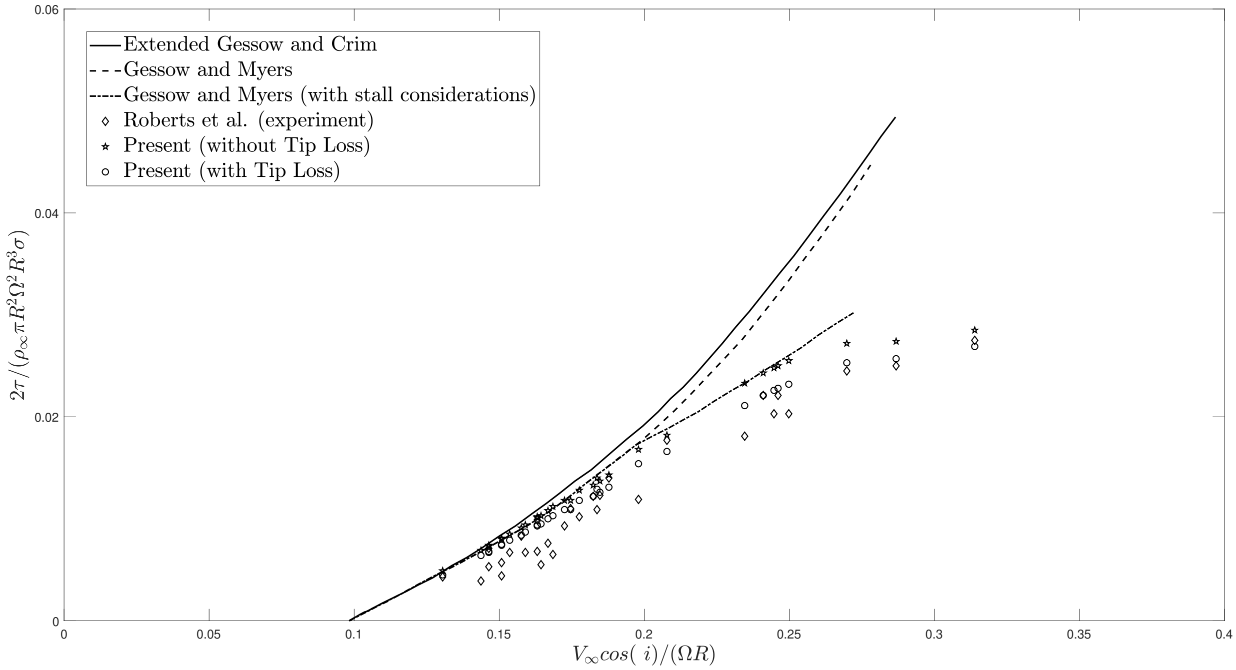

Figure 3.5: The variation of non-dimensional torque against non-dimensional wind velocity. The results from existing theories, such as Extended Gessow and Crim [5], Gessow and Myers [6], and Gessow and Myers with allowance for stall [6] along with the results from the present study are shown against the experimental results of Roberts et al's [7].

accuracy of the present model's results is considerably dependent on the accuracy of the input aerodynamic data.

3.9 Results and discussion

Since the primary objective of this work was the development of a quasi-steady aerodynamic model, a detailed parametric study is not performed. The geometric and operational parameters of the autogyro given in Table 3.3 are chosen based on the information given in [19] and [21]. The parameters of the equivalent rotor mentioned in the Table 3.3 is to study the thrust and power variations shown in Figure 3.6, variation of angle of attack, inflow angle,

Table 3.3: APS rotor parameters

Parameter	Value	Parameter	Value
N_r	1	θ_1	-8°
N_b	2	θ_0	8°
c	0.8 m	i	-40°
R	10 m	β	0°
Z	766 m	λ	6

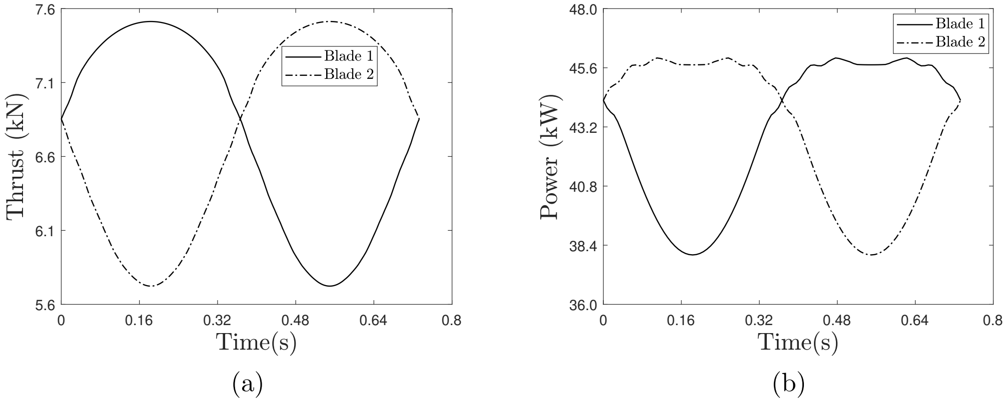

(a) (b)

Figure 3.6: Plots showing the variation of (a) thrust from the blades (kN), and (b) power from the blades (kW) for one cycle of rotation of the rotor as predicted by the quasi-steady BEM theory for parameters mentioned in Table 3.3.

coefficient of lift and coefficient of drag of an airfoil on blade 1 shown in Figure 3.7 and the optimum tip speed ratio shown in Figure 3.8.

Figure 3.6(a) shows the variation of thrust produced and Figure 3.6(b) shows the variation of power produced by each blade in one cycle of rotation of the rotor. As seen, the thrust on the blades cyclically changes between 7.5 kN and 5.7 kN. The power produced by the blades cyclically varies between 46 kW and and 38 kW. Since the blades are 180° apart, so is the

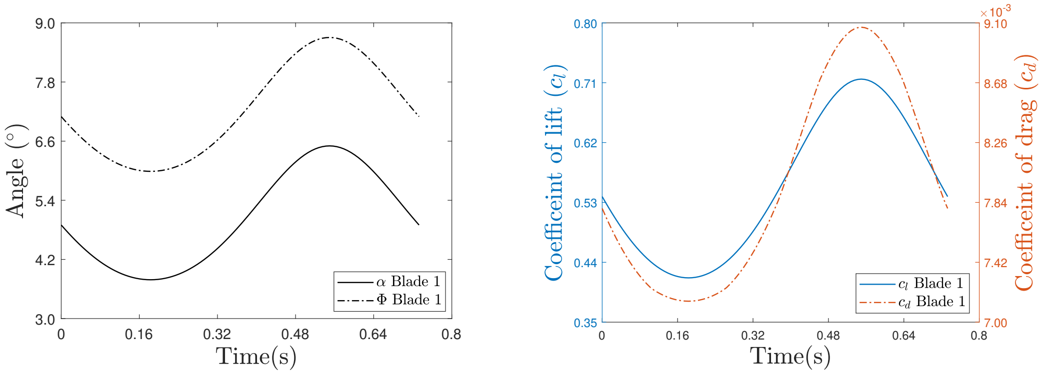

(a) (b)

Figure 3.7: Plots showing the variation of (a) angle of attack, α in (°) and inflow angle, Φ in (°), and (b) coefficient of lift, c_l, and coefficient of drag, c_d, at $r = 0.7R$ on Blade 1 for one cycle of rotation of the rotor.

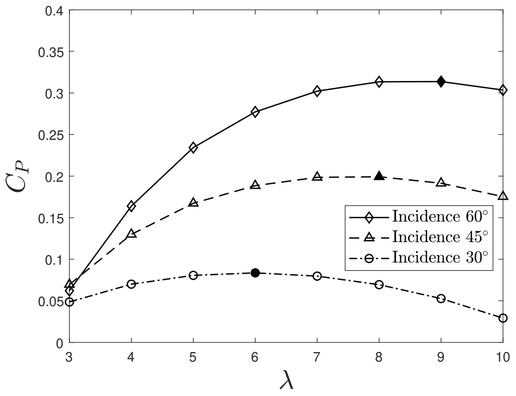

Figure 3.8: Figure showing variation of coefficient of power, C_P with respect to tip speed ratio, λ for different incidence angles i = -30°, -45° and -60°. The filled markers show optimum λ for the respective i.

phase difference in thrust and power produced by the respective blades. The variation of the resultant velocity due to the wind profile and the inclination of rotor is the reason why thrust and power varies during the rotation of blades.

Figure 3.7(a) shows the variation of the angle of attack, α, and inflow angle, Φ, in (°) and Figure 3.7(b) shows the change in coefficient of lift, c_l and coefficient of drag, c_d at $r = 0.7R$ on Blade 1 for one cycle of rotation of the rotor. The angle of attack varies between approximately 6.0° and 8.7° and the inflow angle between approximately 3.8° and 6.5°. The minimum value for c_l is 0.41 and the maximum value attained is 0.71. The c_d varies between 0.007 and 0.009; c_l, c_d and Φ are in phase with α since it is a quasi-steady aerodynamic model.

The variation of C_p with respect to λ for incidence angles of $-30°$, $-45°$ and $-60°$ is shown in Figure 3.8. As seen, for every incidence angle, C_p increases with λ, reaches a maximum value and then drops. A similar behaviour is observed for horizontal- and vertical-axis wind turbines. This may be attributed to the increase in the relative velocity at the blade due to increasing λ; however, eventually at higher values of λ, the rotor blocks the flow and thus C_p decreases. At a given λ (except very low values), C_p increases with the incidence angle. This could be due to the availability for higher freestream velocity component to the rotor. The optimum tip speed ratios are shown by filled markers and are 6, 8 and 9 for incidence angles of $-30°$, $-45°$ and $-60°$, respectively.

3.10 Conclusion

This work presents the aerodynamic modelling of an APS using a quasi-steady BEM theory. The APS with four rotors is fixed in space by knowing the tether length, incidence angle and side slip angle. The aerodynamics presented is that of an equivalent rotor placed at the center of the APS, that is assumed to represent any rotor on the system. For the calculation of unknown induced velocity and angle of attack, the presence of the blades is assumed to affect momentum of flow through only a part of the disc. Unlike most existing models in the literature, which are either time-averaged or unsteady models, the proposed model is quasi-steady. This means that it is more accurate than the time-averaged models and is solved faster than the unsteady models. Such an aerodynamic model can conveniently be coupled to the structural dynamic model of the tether for examining the dynamics of the whole system.

The quasi-steady BEM model for APS was validated against a yawed wind turbine rotor with three blades and an autogyro rotor with two blades. It was found that the quasi-steady BEM is more accurate than the time-averaged models, particularly in the stalled region. However, the quality of the predictions was found to be heavily dependent on the accuracy of the input aerodynamic data.

It was found that the total thrust and power of the rotor, as well as the angle of attack, inflow angle, coefficient of lift and coefficient of drag of airfoil sections of a blade vary with the azimuth angle. The phase difference between the thrust and power of each blades is equal to the angle between the blades. While rotating, the advancing blades on the rotor produce higher thrust and power than the retracting blades. The highest thrust for blade 1 is observed at an azimuth of 45° and lowest at 275°. The angle of attack, inflow angle, coefficient of lift and coefficient of drag on any airfoil on blade is found to be in phase. The lowest value of these parameters are observed at azimuth angle of 45° and the highest at 275° for an airfoil on blade 1. This is observed due to the variation of component of wind which is parallel to the rotor which is maximum and opposite to the rotational velocity at azimuth angle 45°. It was also found that the coefficient of power increases with the incidence angle. It increases with increasing the tip speed ratio, reaches a maxima and decreases with further increase in the tip speed ratio. The optimum tip speed ratio increases with the increase in incidence.

The model can further be improved by the incorporation of a dynamic wake inflow model to make the model dynamic, dynamic stall to take care of rapid change of the angle of attack, yaw model that takes restoring yaw moment into consideration, turbulence and gust models for the wind model to predict more realistic operational characteristics, among others.

Chapter 4

Dynamics of tethered airborne wind energy systems

Almost all airborne wind energy (AWE) systems are tethered and thus the reliability and efficiency of the system are affected by the tension fluctuations in the tether and flow induced vibrations. This chapter presents the numerical results of the dynamics of a tethered aerostatic power system (APS) and a tethered kite power system (KPS). The APS is an autogyro which works on the principle of autorotation whose aerodynamics is predicted by an unsteady BEM model. The KPS considered for the study is a traction kite connected to a winch generator via a tether. Due to aerodynamic forces from the kite, the tether reels in and out to cyclically drive the winch-generator to generate electricity. To understand the effect of elasticity, a rigid tether model as well as an elastic tether model are developed. The tether is modelled as interconnected links with lumped masses having negligible rotary inertia in either case. The (longitudinal) elasticity of the tether is accounted for by linear springs and the structural damping is modelled by viscous dampers. The wind profile following the power law is used for the study, and the aerodynamic forces acting on the tether are predicted using the independence principle. The airborne modules of the systems are modelled as point masses. The verification results of the tether models are indicative of its accuracy.

4.1 Definitions and preliminaries

4.1.1 System definition

The tethered aerostatic power system (APS) has an autogyro that is statically suspended in the air and connected to the ground via a tether. The wind rotates the rotor of the autogyro which can be explained by the principle of auto-rotation and the mechanical energy thus produced is converted to the electrical energy by means of electrical generators coupled to the rotor. The construction and aerodynamics of the autogyro is explained in chapter 3. The electricity produced on-board of the autogyro is transmitted to the ground via conductors

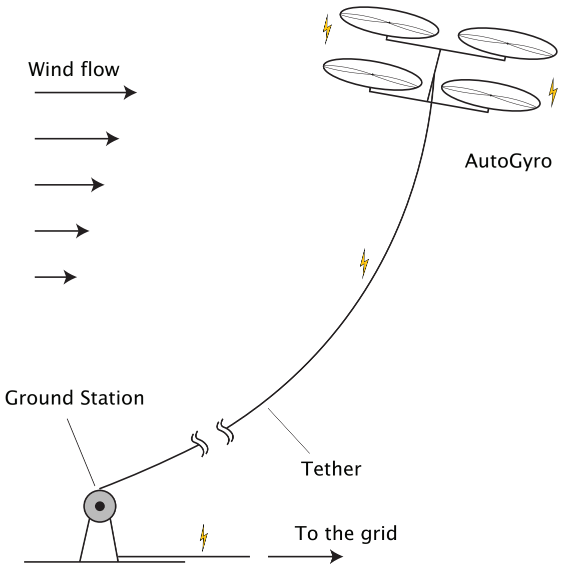

Figure 4.1: Schematic of the autogyro producing electric power on board which is then transmitted to the ground via a tether in APS.

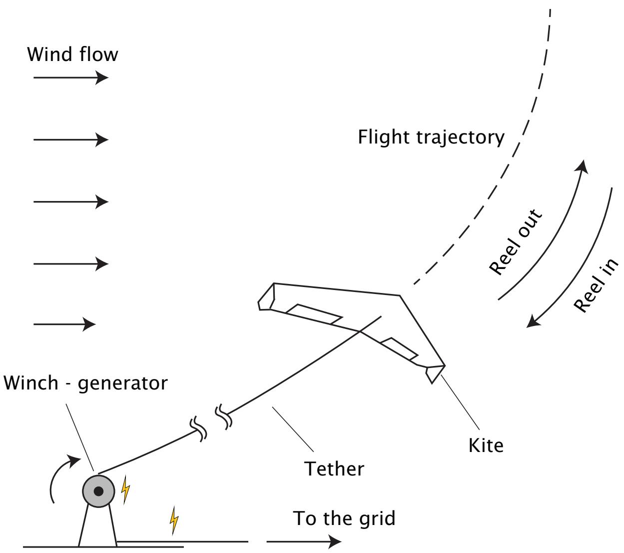

Figure 4.2: Schematic of KPS in which the kite executing reel-in/reel-out motion drives the winch-generator via a tether generating electricity at the ground.

encapsulated by insulator which are structurally supported. The construction and mass modelling of the tethered APS closely follows [21]. The schematic of APS is shown in Figure 4.1.

The kite power system (KPS) consists of a kite that can reel-in/reel-out in the air while being connected to a winch-generator at the ground by a tether. The aerodynamics of the kite is controlled so as to cyclically drive the winch coupled to the electrical generator. The tether reels-out from winch generating electricity and reels-in at the expense of energy. Thus tether is a medium to mechanically transmit power from kite to ground and is simply a structural member. The mechanism of power generation is similar to that of the crosswind kite power system operating in pumping mode as explained in chapter 2. Figure 4.2 shows the schematic of power generation using KPS.

4.1.2 Wind model

A power law wind profile is adopted here [81]:

$$V_Z = V_{Z_r}(\frac{Z}{Z_r})^{\alpha}, \tag{4.1}$$

where V_Z is the wind velocity at height Z above the ground level, Z_r is the reference height and α is the wind shear exponent, which is typically taken as 0.2 [81]. For this study, $Z_r = 10$ m and $V_{Z_r} = 6$ m/s are taken.

The wind velocity vector is written as

$$\overrightarrow{V}_w = V_Z \hat{i}, \tag{4.2}$$

where $\hat{i}$ is the unit vector along the x-axis of the inertial coordinate system.

4.2 Tether modelling

4.2.1 Framework

The equations of motion are formed within the Lagrangian framework expressed as [87]

$$\frac{d}{dt}(\frac{\partial \mathcal{L}}{\partial \dot{q}_i}) - \frac{\partial \mathcal{L}}{\partial q_i} + \frac{\partial \mathcal{R}}{\partial \dot{q}_i} = \mathcal{F}_{nc_i}, \quad i = 1, ..., N \tag{4.3}$$

$$\delta \mathcal{W} = \sum_{i=1}^{N} \mathcal{F}_{nc_i} \delta q_i, \tag{4.4}$$

where q_i are the generalised coordinates, $\mathcal{L} = \mathcal{T} - \mathcal{V}$ is the Lagrangian of the system, $\mathcal{T}$ being the kinetic energy of the system and $\mathcal{V}$ being the potential energy of the system; $\mathcal{R}$ is Rayleigh's dissipation function; also, $\delta \mathcal{W}$ is the virtual work due to non-conservative forces, $\mathcal{F}_{nc_i}$ are the non-conservative generalised forces, and δq_i are the corresponding virtual displacements.

4.2.2 Rigid tether model

See Figure 4.3 which shows the discretization scheme. The inertial coordinate system is a Cartesian system in the two-dimensional space and is denoted by $O : \hat{\imath}, \hat{k}$. The tether is assumed to be uniform and homogeneous. The tether is discretized into N number of rigid links with negligible rotary inertia, and the mass of each link is concentrated at its centre as shown in Figure 4.3. In comparison to the analytical solution for catenary, the model with mass concentrated at the center has the advantage of predicting better static shape for the same N, when compared to mass concentrated at the node model. The ith lumped mass, m_i, is quantified as

$$m_i = \frac{\rho A L_t}{N}, \quad i = 1, ..., N \tag{4.5}$$

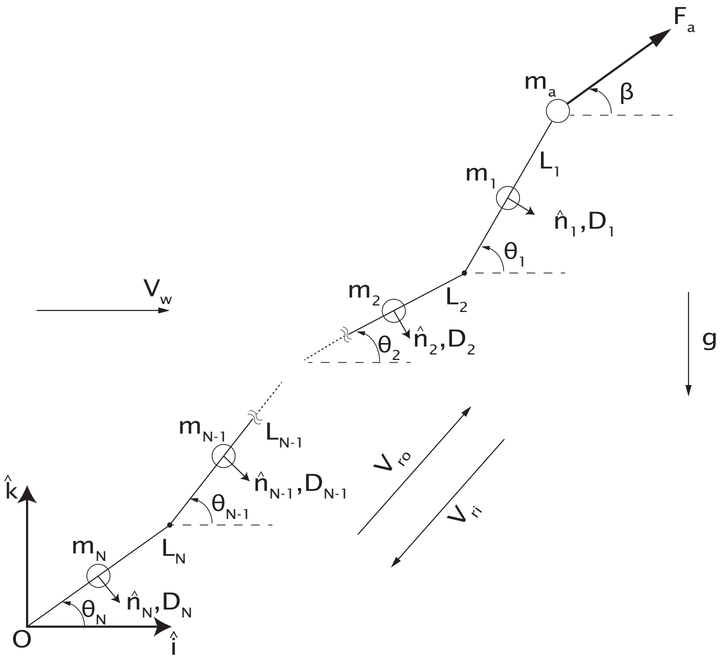

Figure 4.3: Schematic of the rigid tether model showing the inertial frame $O : \hat{\imath}, \hat{k}$, the wind velocity, V_w, lumped masses $m_1, m_2, ..., m_N$, rigid links of length $L_1, L_2, ..., L_N$, generalised coordinates $\theta_1, \theta_2, ..., \theta_N$, aerodynamic drag on tether element $D_1, D_2, ..., D_N$, unit vectors normal to the tether element $\hat{n}_1, \hat{n}_2, ..., \hat{n}_N$, reel-out velocity V_{ro}, reel-in velocity V_{ri}, kite mass m_a, external force of magnitude F_a at the angle β and the direction of gravity.

where ρ is the density of tether, A is the cross-sectional area of the tether and L_t is the unstretched length of the tether.

The airborne module is modelled as a point mass, with mass m_a at the farthest end of the tether. The generalised coordinates of the rigid tether model are in the polar coordinate system. A body axes frame is defined on each lumped mass to calculate the aerodynamic drag acting on the tether element.

The position vector of the airborne module is given by

$$\overrightarrow{R}_a = \sum_{j=1}^{N} L_j[\cos(\theta_j)\hat{\imath} + \sin(\theta_j)\hat{k}], \tag{4.6}$$

where

$$L_j = \frac{L_t}{N}, \tag{4.7}$$

is the length of the jth rigid tether element and θ_j is the corresponding generalised coordinate.

The velocity vector of the airborne module thus becomes

$$\overrightarrow{V}_a = \frac{d\overrightarrow{R}_a}{dt} = \sum_{j=1}^{N} L_j\dot{\theta}_j[-\sin(\theta_j)\hat{\imath} + \cos(\theta_j)\hat{k}]. \tag{4.8}$$

The position vector of the centre of the ith tether element is given by

$$\overrightarrow{R}_i = \sum_{j=i}^{N} P_j L_j[\cos(\theta_j)\hat{\imath} + \sin(\theta_j)\hat{k}], \tag{4.9}$$

where $P_j = 1/2$ if $i = j$, else $P_j = 1$; thus its velocity vector is obtained as

$$\overrightarrow{V}_i = \frac{d\overrightarrow{R}_i}{dt} = \sum_{j=i}^{N} P_j L_j\dot{\theta}_j[-\sin(\theta_j)\hat{\imath} + \cos(\theta_j)\hat{k}], \tag{4.10}$$

where the *overdot* represents a time-derivative.

The kinetic energy of the system can be obtained as

$$\mathcal{T} = \frac{1}{2} m_a \overrightarrow{V}_a . \overrightarrow{V}_a + \sum_{i=1}^{N} \frac{1}{2} m_i \overrightarrow{V}_i . \overrightarrow{V}_i, \tag{4.11}$$

which can be extended as follows

$$\mathcal{T} = \frac{1}{2} \sum_{i=1}^{N} \sum_{j=i}^{N} P_j^2 m_i L_j^2 \dot{\theta}_j^2 + \frac{m_a}{2} \sum_{j=1}^{N} L_j^2 \dot{\theta}_j^2 + \frac{1}{2} \sum_{i=1}^{N} \sum_{j=1}^{N} \sum_{k=j+1}^{N} 2 P_j m_i L_j L_k \dot{\theta}_j \dot{\theta}_k \cos(\theta_k - \theta_j) \tag{4.12}$$

$$+ \frac{m_a}{2} \sum_{j=1}^{N} \sum_{k=j+1}^{N} 2 L_j L_k \dot{\theta}_j \dot{\theta}_k \cos(\theta_k - \theta_j). \tag{4.13}$$

On the other hand, the expression of the potential energy of the system is given as

$$\mathcal{V} = m_a g \sum_{j=1}^{N} L_j \sin(\theta_j) + \sum_{i=1}^{N} m_i g \sum_{j=i}^{N} P_j L_j \sin(\theta_j), \tag{4.14}$$

in which g is the gravitational acceleration.

The virtual work due to non-conservative forces can also be written as

$$\delta\mathcal{W} = \overrightarrow{F}_a . \delta \overrightarrow{R}_a + \sum_{i=1}^{N} D_i . \delta \overrightarrow{R}_i, \tag{4.15}$$

where $\overrightarrow{F}_a$ is the force exerted by the airborne module on the tether, and $\overrightarrow{D}_j$ is the aerodynamic drag acting on the $j$the element of the tether; the virtual displacement of the airborne module, $\delta \overrightarrow{R}_a$, and that at the jth element (or lumped mass), $\delta \overrightarrow{R}_j$, are given by

$$\delta \overrightarrow{R}_a = \sum_{j=1}^{N} L_j \delta\theta_j (-\sin(\theta_j)\hat{i} + \cos(\theta_j)\hat{k}), \tag{4.16}$$

and

$$\delta \overrightarrow{R}_i = \sum_{j=i}^{N} P_j L_j \delta\theta_j (-\sin(\theta_j)\hat{\imath} + \cos(\theta_j)\hat{k}), \tag{4.17}$$

respectively.

Following the independence principle [67], D_i can be written as

$$\overrightarrow{D}_i = \frac{1}{2}\rho_\infty |\overrightarrow{V}_{Reli} \cdot \hat{n}_i| (\overrightarrow{V}_{Reli} \cdot \hat{n}_i) L_j d C_d \hat{n}_i, \tag{4.18}$$

where ρ_∞ is the free-stream density, d is the diameter of the tether, and C_d is the normal drag coefficient of the tether; also, $\overrightarrow{V}_{Reli}$ and $\hat{n}_i$ are the relative flow velocity and the unit normal vector at the ith element given by

$$\overrightarrow{V}_{Reli} = \overrightarrow{V}_w - \overrightarrow{V}_i, \tag{4.19}$$

and

$$\hat{n}_i = \sin(\theta_i)\hat{\imath} - \cos(\theta_i)\hat{k}, \tag{4.20}$$

respectively.

The ith generalised force is give by

$$\mathcal{F}_{nc_i} = L_i(-\sin(\theta_i)\ \hat{\imath} + \cos(\theta_i)\ \hat{k}) \cdot [\overrightarrow{F}_a + \sum_{j=1}^{i} P_j \overrightarrow{D}_j]. \tag{4.21}$$

The final equation of motion in the first-order (or state space) form for the ith mass (or element) may be written as

$$[\sum_{j=1}^{i} P_j^2 m_j + m_a] L_i^2 \ddot{\theta}_i + \sum_{j=1}^{i} \sum_{k=j,k\neq i}^{N} A_i m_j [L_i L_k \ddot{\theta}_k \cos(\theta_k - \theta_i) - L_i L_k \dot{\theta}_k^{\,2} \sin(\theta_k - \theta_i)]$$
$$+ \sum_{k=1,k\neq i}^{N} m_a [L_i L_k \ddot{\theta}_k \cos(\theta_k - \theta_i) - L_i L_k \dot{\theta}_k^{\,2} \sin(\theta_k - \theta_i)] + g L_i \cos(\theta_i) [\sum_{j=1}^{i} P_j m_j + m_a]$$
$$= L_i(-\sin(\theta_i)\ \hat{i} + \cos(\theta_i)\ \hat{k}) \cdot [\overrightarrow{F}_a + \sum_{j=1}^{i} P_j \overrightarrow{D}_j], \quad i = 1, ..., N \tag{4.22}$$

where $A_i = \frac{1}{2}$ if $j = r$ or $j = i,$ else $A_i = 1.$

The numerical results are obtained by solving the system of ordinary differential equations in time.

To derive the equations of tension in tether, it is assumed that the the value of tension between any two adjacent lumped masses is the same. Tension in the first tether element (i.e., between the first lumped mass and the airborne module) is given by

$$T_1 = \sqrt{\Big(|\overrightarrow{F}_a| \cos(\beta) - m_a \ddot{x}_a\Big)^2 + \Big(|\overrightarrow{F}_a| \sin(\beta) - m_a g - m_a \ddot{z}_a\Big)^2}, \tag{4.23}$$

where $\ddot{x}_a$ and $\ddot{z}_a$ are given by

$$\ddot{x}_a = -\sum_{i=1}^{N} L_i \ddot{\theta}_i \sin(\theta_i) - \sum_{i=1}^{N} L_i \dot{\theta}_i^2 \cos(\theta_i), \tag{4.24}$$

$$\ddot{z}_a = \sum_{i=1}^{N} L_i \ddot{\theta}_i \cos(\theta_i) - \sum_{i=1}^{N} L_i \dot{\theta}_i^2 \sin(\theta_i). \tag{4.25}$$

Tension in the last tether element (i.e., between the ground and the lumped mass closest to the ground) is given by

$$T_N = \tag{4.26}$$

$$\sqrt{\left(T_1\sin(\theta_1)+\sum_{i=1}^{N}D_i\cdot\hat{k}-\sum_{i=1}^{N}m_i\ddot{z}_i-\sum_{i=1}^{N}m_ig\right)^2+\left(T_1\cos(\theta_1)+\sum_{i=1}^{N}D_i\cdot\hat{\imath}-\sum_{i=1}^{N}m_i\ddot{x}_i\right)^2},$$

where $\ddot{x}_i$ and $\ddot{z}_i$ are written as

$$\ddot{x}_i = -\sum_{j=i}^{N}P_jL_j\ddot{\theta}_j\sin(\theta_j)-\sum_{j=i}^{N}P_jL_j\dot{\theta}_j^2\cos(\theta_j), \tag{4.27}$$

and

$$\ddot{z}_i = \sum_{j=i}^{N}P_jL_j\ddot{\theta}_j\cos(\theta_j)-\sum_{j=i}^{N}P_jL_j\dot{\theta}_j^2\sin(\theta_j), \tag{4.28}$$

respectively.

4.2.3 Elastic tether model

Figure 4.4 shows the discretization scheme for the elastic tether. Here, the inertial coordinate system is denoted by $O : \hat{\imath}, \hat{\jmath}$. Unlike the rigid tether, the position of the first lumped mass is representative of the position of the airborne module. The tether is modelled as N interconnected links of the same length. The mass of each link is concentrated at the respective node, as shown in the Figure 4.4. Except for m_1, which is inclusive of the airborne module mass and half of the tether element mass, the ith lumped mass, m_i, is the average of the mass of adjacent elements

$$m_1 = m_a + \frac{\rho AL_t}{2N}, \qquad m_i = \frac{\rho AL_t}{N}, \;\; i = 2, ..., N. \tag{4.29}$$

The combination of a linear spring and a viscous damper in each element accounts for

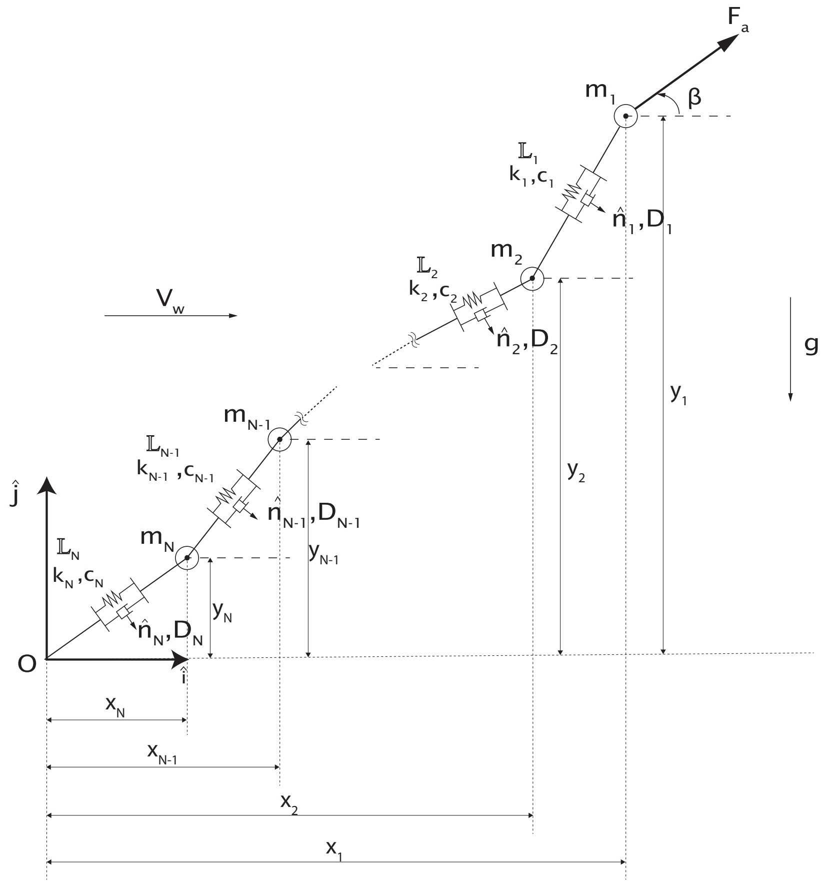

Figure 4.4: Schematic of the elastic tether model showing the inertial frame $O : \hat{\imath}, \hat{\jmath}$, the wind velocity, V_w, lumped masses $m_1, m_2, ..., m_N$, extensible links of length $\mathbb{L}_1, \mathbb{L}_2, ..., \mathbb{L}_N$, stiffness of tether elements $k_1, k_2, ..., k_N$, damping coefficient of tether elements $c_1, c_2, ..., c_N$, generalised coordinates $x_1, x_2, ..., x_N$ and $y_1, y_2, ..., y_N$, aerodynamic drag on tether element $D_1, D_2, ..., D_N$, unit vectors normal to the tether element $\hat{n}_1, \hat{n}_2, ..., \hat{n}_N$, reel-out velocity V_{ro}, reel-in velocityV_{ri}, external force of magnitude F_a at the angle β and the direction of gravity.

elasticity and structural damping of the tether, respectively. In contrast to Section 4.2.3, the Cartesian coordinates are chosen as the generalised coordinates in the elastic tether model. As seen in the following, this considerably simplifies the derivations since the coordinates of each lumped mass, and thus their velocities and virtual displacements, can be expressed independently from other lumped masses.

The position vector of the ith lumped mass is given by

$$\overrightarrow{R}_i = x_i\hat{\imath} + y_i\hat{\jmath}, \tag{4.30}$$

and thus, the velocity vector becomes

$$\overrightarrow{V}_i = \frac{d\overrightarrow{R}_i}{dt} = \dot{x}_i\hat{\imath} + \dot{y}_i\hat{\jmath}. \tag{4.31}$$

The expressions of the kinetic and potential energies of the system are given as

$$\mathcal{T} = \frac{1}{2}\sum_{i=1}^{N} m_i[\dot{x}_i^2 + \dot{y}_i^2], \tag{4.32}$$

and

$$\mathcal{V} = \sum_{i=1}^{N}[m_i g y_i + \frac{1}{2}k_i s_i^2], \tag{4.33}$$

respectively; k_i and s_i are the stiffness and extension of the ith tether element, respectively.

Assuming the tether is made of a linear-elastic material, k_i may be written as

$$k_i = N\frac{EA}{L_t}, \tag{4.34}$$

in which E is the Young's modulus of elasticity of the material.

The longitudinal extension of the elements can be obtained as follows

$$\begin{aligned} s_i &= \mathbb{L}_i - L_i, \;\; i = 1, 2..., N-1 \\ s_N &= \mathbb{L}_N - L_N, \;\; i = N, \end{aligned} \tag{4.35}$$

where L_i is the length of the elastic element given by

$$\begin{aligned}
\mathbb{L}_i &= \sqrt{(x_i - x_{i+1})^2 + (y_i - y_{i+1})^2}, \ \ i = 1, 2..., N-1 \\
\mathbb{L}_N &= \sqrt{x_N^2 + y_N^2}, \ \ i = N.
\end{aligned} \tag{4.36}$$

The damping due to viscous dampers can be included using the Rayleigh's dissipation function (see equation (4.3))

$$\mathcal{R} = \sum_{i=1}^{N} \frac{1}{2} c_i \dot{s}_i^2, \tag{4.37}$$

where c_i is the damping coefficient of the ith element, which can be obtained as

$$c_i = 2\zeta\sqrt{k_i m_i}, \tag{4.38}$$

in which ζ is the damping ratio.

It should be noted that in the present model, c_i remains constant as the tether length (and thus the length of each element) varies, for the reasons given in Appendix D. A similar approach can also be found in the work of Milutinović et al. [46] while some other studies (e.g., Ref. [47]) apparently considered variable damping coefficients.

The virtual work due to non-conservative forces can be obtained as

$$\delta \mathcal{W} = \overrightarrow{F}_a . \delta \overrightarrow{R}_1 + \sum_{i=1}^{N} \overrightarrow{D}_i . \delta \overrightarrow{R}_i, \tag{4.39}$$

where the virtual displacement vector $\delta \overrightarrow{R}_i$ can be written as

$$\delta \overrightarrow{R}_i = \delta x_i \hat{i} + \delta y_i \hat{j}. \tag{4.40}$$

The drag forces are estimated at the centre of the elements, and the average of forces acting on two adjacent elements is placed on the ith node, that is given by

$$\begin{aligned}
\overrightarrow{D}_1 &= \frac{\frac{1}{2}\rho_\infty|\overrightarrow{V}_{Rel1}\cdot\hat{n}_1|(\overrightarrow{V}_{Rel1}\cdot\hat{n}_1)\mathbb{L}_1 dC_d\hat{n}_1}{2}, \ \ i=1 \\
\overrightarrow{D}_i &= \frac{\frac{1}{2}\rho_\infty|\overrightarrow{V}_{Reli}\cdot\hat{n}_i|(\overrightarrow{V}_{Reli}\cdot\hat{n}_i)\mathbb{L}_i dC_d\hat{n}_i}{2}+ \\
&\frac{\frac{1}{2}\rho_\infty|\overrightarrow{V}_{Reli-1}\cdot\hat{n}_{i-1}|(\overrightarrow{V}_{Reli-1}\cdot\hat{n}_{i-1})\mathbb{L}_{i-1} dC_d\hat{n}_{i-1}}{2}, \ \ i=2,3...,N,
\end{aligned} \tag{4.41}$$

in which $\overrightarrow{V}_{Reli}$ is the relative velocity at the ith tether element given by

$$\overrightarrow{V}_{Reli} = \overrightarrow{V}_w - \overrightarrow{V}_{ci}, \tag{4.42}$$

where $\overrightarrow{V}_{ci}$ is the velocity vector of the centre of the ith element:

$$\begin{aligned}
\overrightarrow{V}_{ci} &= (\dot{x}_i - \frac{\dot{x}_i-\dot{x}_{i+1}}{2})\hat{\imath} + (\dot{y}_i - \frac{\dot{y}_i-\dot{y}_{i+1}}{2})\hat{\jmath}, \ \ i=1,2,...,N-1 \\
\overrightarrow{V}_{cN} &= (\frac{\dot{x}_N}{2})\hat{\imath} + (\frac{\dot{y}_N}{2})\hat{\jmath}, \ \ i=N.
\end{aligned} \tag{4.43}$$

The unit vector normal to the ith tether element, $\hat{n}_i$, can be obtained as

$$\hat{n}_i = \sin(\theta_i)\hat{\imath} - \cos(\theta_i)\hat{\jmath}, \tag{4.44}$$

where

$$\begin{aligned}
\theta_i &= tan^{-1}\left(\frac{y_i-y_{i+1}}{x_i-x_{i+1}}\right), \ \ i=1,2,...,N-1 \\
\theta_N &= tan^{-1}\left(\frac{y_N}{x_N}\right). \ \ i=N.
\end{aligned} \tag{4.45}$$

The final equations of motion in the first-order (or state space) for when $N>1$ can be written as

$$
\begin{aligned}
& m_1\ddot{x}_1 + k_1(x_1 - x_2)\left(1 - \frac{L_1}{\sqrt{(x_1 - x_2)^2 + (y_1 - y_2)^2}}\right) + \\
& c_1(x_1 - x_2)\left(\frac{(x_1 - x_2)(\dot{x}_1 - \dot{x}_2) + (y_1 - y_2)(\dot{y}_1 - \dot{y}_2)}{(x_1 - x_2)^2 + (y_1 - y_2)^2}\right) = (\overrightarrow{F}_a + \overrightarrow{D}_1) \cdot \hat{i}, \;\; i = 1 \qquad (4.46)
\end{aligned}
$$

$$
\begin{aligned}
& m_i\ddot{x}_i + k_i(x_i - x_{i+1})\left(1 - \frac{L_i}{\sqrt{(x_i - x_{i+1})^2 + (y_i - y_{i+1})^2}}\right) - \\
& k_{i-1}(x_{i-1} - x_i)\left(1 - \frac{L_{i-1}}{\sqrt{(x_{i-1} - x_i)^2 + (y_{i-1} - y_i)^2}}\right) + \\
& c_i(x_i - x_{i+1})\left(\frac{(x_i - x_{i+1})(\dot{x}_i - \dot{x}_{i+1}) + (y_i - y_{i+1})(\dot{y}_i - \dot{y}_{i+1})}{(x_i - x_{i+1})^2 + (y_i - y_{i+1})^2}\right) - \\
& c_{i-1}(x_{i-1} - x_i)\left(\frac{(x_{i-1} - x_i)(\dot{x}_{i-1} - \dot{x}_i) + (y_{i-1} - y_i)(\dot{y}_{i-1} - \dot{y}_i)}{(x_{i-1} - x_i)^2 + (y_{i-1} - y_i)^2}\right) \\
& = \overrightarrow{D}_i \cdot \hat{i}, \;\; i = 2, 3, ..., N-1 \qquad (4.47)
\end{aligned}
$$

$$
\begin{aligned}
& m_N\ddot{x}_N + k_N x_N\left(1 - \frac{L_N}{\sqrt{x_N^2 + y_N^2)}}\right) - \\
& k_{N-1}(x_{N-1} - x_N)\left(1 - \frac{L_{N-1}}{\sqrt{(x_{N-1} - x_N)^2 + (y_{N-1} - y_N)^2}}\right) + c_N x_N\left(\frac{x_N\dot{x}_N + y_N\dot{y}_N}{x_N^2 + y_N^2}\right) - \\
& c_{N-1}(x_{N-1} - x_N)\left(\frac{(x_{N-1} - x_N)(\dot{x}_{N-1} - \dot{x}_N) + (y_{N-1} - y_N)(\dot{y}_{N-1} - \dot{y}_N)}{(x_{N-1} - x_N)^2 + (y_{N-1} - y_N)^2}\right) = \overrightarrow{D}_N \cdot \hat{i}, \;\; i = N \\
& \qquad (4.48)
\end{aligned}
$$

in the x-direction, and

$$
\begin{aligned}
&m_1\ddot{y}_1 + m_1 g + k_1(y_1 - y_2)\left(1 - \frac{L_1}{\sqrt{(x_1 - x_2)^2 + (y_1 - y_2)^2}}\right) + \\
&c_1(y_1 - y_2)\left(\frac{(x_1 - x_2)(\dot{x}_1 - \dot{x}_2) + (y_1 - y_2)(\dot{y}_1 - \dot{y}_2)}{(x_1 - x_2)^2 + (y_1 - y_2^2)}\right) = (\overrightarrow{F}_a + \overrightarrow{D}_1)\cdot\hat{j},\ \ i = 1 \qquad (4.49)
\end{aligned}
$$

$$
\begin{aligned}
&m_i\ddot{y}_i + m_i g + k_i(y_i - y_{i+1})\left(1 - \frac{L_i}{\sqrt{(x_i - x_{i+1})^2 + (y_i - y_{i+1})^2}}\right) - \\
&k_{i-1}(y_{i-1} - y_i)\left(1 - \frac{L_{i-1}}{\sqrt{(x_{i-1} - x_i)^2 + (y_{i-1} - y_i)^2}}\right) \\
&+ c_i(y_i - y_{i+1})\left(\frac{(x_i - x_{i+1})(\dot{x}_i - \dot{x}_{i+1}) + (y_i - y_{i+1})(\dot{y}_i - \dot{y}_{i+1})}{(x_i - x_{i+1})^2 + (y_i - y_{i+1})^2}\right) \\
&- c_{i-1}(y_{i-1} - y_i)\left(\frac{(x_{i-1} - x_i)(\dot{x}_{i-1} - \dot{x}_i) + (y_{i-1} - y_i)(\dot{y}_{i-1} - \dot{y}_i)}{(x_{i-1} - x_i)^2 + (y_{i-1} - y_i)^2}\right) \\
&= \overrightarrow{D}_i\cdot\hat{j},\ \ i = 2, 3, ..., N - 1 \qquad (4.50)
\end{aligned}
$$

$$
\begin{aligned}
&m_N\ddot{y}_N + m_N g + k_N y_N\left(1 - \frac{L_N}{\sqrt{x_N^2 + y_N^2)}}\right) - \\
&k_{N-1}(y_{N-1} - y_N)\left(1 - \frac{L_{N-1}}{\sqrt{(x_{N-1} - x_N)^2 + (y_{N-1} - y_N)^2}}\right) + c_N y_N\left(\frac{x_N\dot{x}_N + y_N\dot{y}_N}{x_N^2 + y_N^2}\right) - \\
&c_{N-1}(y_{N-1} - y_N)\left(\frac{(x_{N-1} - x_N)(\dot{x}_{N-1} - \dot{x}_N) + (y_{N-1} - y_N)(\dot{y}_{N-1} - \dot{y}_N)}{(x_{N-1} - x_N)^2 + (y_{N-1} - y_N)^2}\right) = \overrightarrow{D}_N\cdot\hat{j},\ \ i = N \\
&\qquad (4.51)
\end{aligned}
$$

in the y-direction.

If $N = 1$, the equations of motion become

$$
m_1\ddot{x}_1 + k_1 x_1\left(1 - \frac{L_1}{\sqrt{x_1^2 + y_1^2}}\right) + c_1 x_1\left(\frac{x_1\dot{x}_1 + y_1\dot{y}_1}{\sqrt{x_1^2 + y_1^2}}\right) = (\overrightarrow{F}_a + \overrightarrow{D}_1)\cdot\hat{i}, \qquad (4.52)
$$

$$
m_1\ddot{y}_1 + m_1 g + k_1 y_1\left(1 - \frac{L_1}{\sqrt{x_1^2 + y_1^2}}\right) + c_1 y_1\left(\frac{x_1\dot{x}_1 + y_1\dot{y}_1}{\sqrt{x_1^2 + y_1^2}}\right) = (\overrightarrow{F}_a + \overrightarrow{D}_1)\cdot\hat{j}. \qquad (4.53)
$$

The numerical results are obtained by solving the system of ordinary differential equations in time. After obtaining the time history of $x_i,\ y_i,\ (i = 1\cdots N)$ and $\dot{x}_i,\ \dot{y}_i,\ (i = 1\cdots N)$, equations (4.35) and (4.36) can be used to obtain the longitudinal extension of each element and its time derivatives, from which tension can be obtained:

$$T_i = k_i s_i + c_i \dot{s}_i. \tag{4.54}$$

It is worth noting that, in the elastic tether model, even though the damping coefficient remains the same irrespective of the tether length, the stiffness of each element is N times the stiffness of the full-length tether.

4.2.4 Reel-in/reel-out model

The two widely used approaches to implement reel-in/reel-out were developed by Williams et al. [50] and Fechner et al. [47]. In the Williams et al.'s approach, the length of each element is kept constant and a new element of variable length is added to account for the reel-out or removed to implement the reel-in. If the existing tether had N elements, this newly added variable length element becomes the $(N+1)$th element and is treated as rest of the elements upon reaching a critical length. The reel-in/reel-out is dynamically treated by this method. However, introduction of new elements might create unrealistic perturbations in the elastic tether model and removal of elements might effect position and velocities of remaining elements if not treated carefully. The number of elements is variable and thus the algorithm to implement this method will require a state space vector of variable dimensions. Interested readers are referred to Williams et. al. [50] for further reading.

In contrast to the above mentioned approach, Fechner et al.'s method employs a fixed number of elements which vary equally in their unstretched length during reel-in/reel-out. The reel-in/reel-out creates a variation in the overall unstretched length of the tether, L_t. The dynamics is predicted by re-discretising the tether of the new length into N elements at every

Table 4.1: reel-in/reel-out algorithm for rigid tether model

Step	Task
1	For time t, initialize θ_i and $\dot{\theta}_i$ from $t - \Delta t$ (For $t = 0$, initial conditions can be the static solution).
2	Find L_t and $\overrightarrow{F}_a$ for time t from the known variations.
3	Update m_i as per equation (4.5), and L_j by equation (4.7), knowing N.
4	Find the new $\overrightarrow{V}_w$ from equations (4.2) and (4.1) by using the updated $\overrightarrow{R}_i$ from equation (4.9).
5	Update $\overrightarrow{V}_i$ in equation (4.10) and find $\overrightarrow{V}_{Reli}$ from equation (4.19).
6	Find $\hat{n}_i$ using equation (4.20) and update $\overrightarrow{D}_i$ in equation (4.18).
7	Solve equations of motion (4.22) for time t.

instant. This method has the the advantage of having a state space vector with constant dimension and a stable algorithm which does not complicate the dynamical calculations associated with adding or removing elements. However, this approach may be called quasi static since it includes the effects of tether reel-in/reel-out only through the instantaneous tether length.

Fechner et al.'s approach is followed in this study. Since the mass of airborne module is typically 30 to 40 times the tether mass, the author assumes that the kinetic energy deficit due to the quasi static modelling of tether reel-in/reel-out can be neglected. The variation of tether length, L_t and the variation of external force/thrust, $\overrightarrow{F}_a$ are assumed to be known *a priori*. Such an input cycle is shown in Figure 4.10. The equations of motion of rigid tether given by (4.22) and elastic tether by (4.46) to (4.51) are then solved in time for a new tether with constant N at each time step.

The algorithm mentioned in Table 4.1 is followed to implement reel-in/reel-out for the rigid tether model for an instant of time. On the other hand, the algorithm for the reel-in/reel-out of the elastic tether can be found in Table 4.2. When compared to the rigid

Table 4.2: reel-in/reel-out algorithm for elastic tether model

Step	Task
1	For time t, initialize x_i, y_i, $\dot{x}_i$ and $\dot{y}_i$ from $t - \Delta t$ (For $t = 0$, initial conditions can be the static solution).
2	Find L_t and $\overrightarrow{F}_a$ for time t from the known variations.
3	Update m_i as per (4.29), L_j by (4.7) and k_i in (4.34) knowing N.
4	Find how much L_j changed by marching from the previous instance and add it with (4.36) to obtain the new $\mathbb{L}_i$.
5	Find the new $\overrightarrow{V}_w$ from equations (4.2) and (4.1) by using the updated $\overrightarrow{R}_i$ from equation (4.30).
6	Update $\overrightarrow{V}_{ci}$ in (4.43) and find $\overrightarrow{V}_{Reli}$ from (4.42).
7	Update θ_i from (4.45) to find the $\hat{n}_i$ using (4.44).
8	Update the $\overrightarrow{D}_i$ in (4.41).
9	Solve the elastic tether model equations of motion (4.46) to (4.51) for time t.

tether model, the elastic tether model needs more sophisticated algorithm. The tether drag found at the nodal points is the average of tether drag of adjacent elements, the stiffness values of elements needs to be updated, tether angles need to be calculated and the variation of tether length during reel-in/reel-out velocity is calculated based on the rigid length.

4.3 Verification of the model

To the best of the author's knowledge, no studies exist that experimentally study the dynamics of tethers in AWE applications. Due to lack of such experimental data, some comparisons are made against analytical results from similar applications as to verify the tether models. The analytical equation for a catenary cable is used to verify the static shape and for verifying the effect of aerodynamics on the tether. The dynamic equation for plucked string vibration is used to verify the dynamics as well as the distribution of the damping coefficient.

Throughout this work, the tether material is chosen to be dyneema [88]. In the case of APS, the structural support will be provided by dyneema. Dyneema is assumed to have a density of 970 kg/m^3, Young's modulus of elasticity of 109 GPa and an ultimate tensile strength of 3.9 GPa [89]. A safety factor of 3 is used for diameter calculations [88].

4.3.1 Verification of the statics

The analytical solution for the shape of an elastic catenary in static equilibrium [90] is used for the verification of the statics of the tether model:

$$a_T = \frac{F_x}{\gamma_e g}, \tag{4.55}$$

$$x = a_T \sinh^{-1}\left(\frac{s}{a_T}\right) + a_T \frac{\gamma_e g}{EA} s, \tag{4.56}$$

$$z = \sqrt{a_T^2 + s^2} + \frac{\gamma_e g}{2EA} s^2 - a_T, \tag{4.57}$$

where F_x is the horizontal component of tension (or end-force); s is the curvilinear coordinate along the catenary, and γ_e is the mass per unit length.

By assuming numerical values for EA, γ_e, and F_x and considering s in the range of $0 \leq s \leq L_t$, x and z can be found from equations (4.56) and (4.57), respectively. The vertical component of tension (or end-force) can then be obtained from the analytical solution as

$$F_y = \left(\frac{z_1 - z_2}{x_1 - x_2}\right) F_x + m_1 g. \tag{4.58}$$

The same inputs used in the analytical equations are used in the tether model to predict the static shape numerically. It should be noted that F_x and F_y define F_a in the equations of motion of the tether. The equations governing the statics of the rigid and elastic tether are

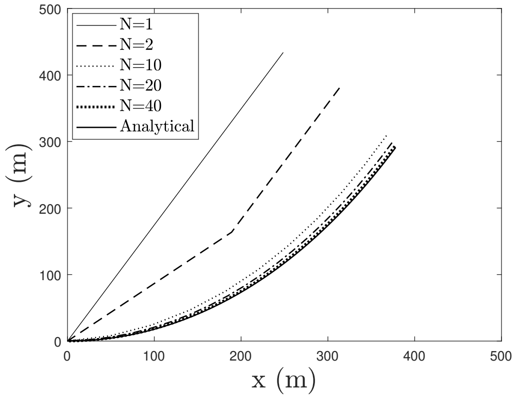

Figure 4.5: Figure showing verification of numerically predicted shape of catenary against analytical solution of catenary for $N = 1, 2, 10, 20, 40$ and $L_t = 500m$.

obtained by letting the time-dependent terms to zero in equation (4.22) for the rigid tether and in (4.46) to (4.51) for the elastic tether. Also, note that the aerodynamic drag is put to zero in the tether models.

Figure 4.5 shows the results from the verification study of the static shape of the elastic tether for different values of N. It is observed that with $N = 20$, the tether model predicts the shape very close to that of the catenary from the analytical solution. Studies were also conducted to ensure that the rigid and elastic tether models predict the static shape in agreement with the analytical solution for different N, L_t, E, A, and $\overrightarrow{F}_a$. In order to verify the effect of wind on the tether shape, the aerodynamic forces were also taken into account. It was observed that depending on the wind direction, the tether moved to the either side of the horizontal axis. It was also observed that even though the analytical solution could only predict the catenary in the first quadrant, by varying $\overrightarrow{F}_a$, the numerical model could predict shape in all four quadrants.

4.3.2 Verification of the dynamics

The analytical solution for the dynamics of a plucked string is used for the verification of the tether model. This is done by reducing the tether model to a numerical model for the plucked string. Consider an elastic string of the unstretched length L_t, which is fixed at the two ends and initially pulled from the middle by h in the transverse direction. The string is then let free to vibrate. The time-dependent displacement of the string in the transverse direction, $z(x,t)$, can be obtained analytically, as follows [74]

$$z(x,t) = \frac{8h}{\pi^2} \sum_{i=1,3,\ldots}^{\infty} \frac{(-1)^{\frac{i-1}{2}}}{i^2} \sin\left(\frac{i\pi x}{L_t}\right) \cos(\omega_i t), \tag{4.59}$$

where ω_i is the angular frequency of the ith mode shape given by

$$\omega_i = \frac{i\pi}{L_t}\sqrt{\frac{T}{\gamma_e}}, \tag{4.60}$$

in which γ_e is the mass of the tether per unit length, and T is the tension in the tether, which is obtained from

$$T = EA\epsilon, \tag{4.61}$$

where ϵ the axial strain in the tether:

$$\epsilon = \sqrt{1 + (\frac{2h}{L_t})^2} - 1. \tag{4.62}$$

Equations (4.46) to (4.51) which govern the dynamics of the elastic tether can be reduced to the equation of the plucked string by defining the farthermost end coordinates (x_1, y_1) as $(L_t, 0)$ and by substituting time derivatives of (x_1, y_1) with zero. Also, m_a and m_1 are given negligibly small values (e.g. 10^{-6}) while setting V_w, F_a, D_i and g to zero for the analysis.

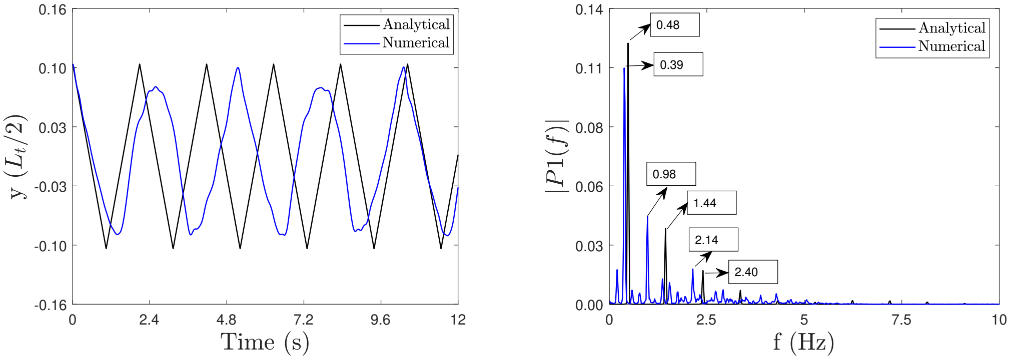

(a) (b)

Figure 4.6: Plots showing the variation of (a) amplitude of centre of string in (m), and (b) frequency as predicted by the analytical equation and numerical model for $N = 20$.

For comparison of results, a string of the length $L_t = 1$ m and axial rigidity $EA = 25$ N is used; also, $h = 0.1$ m is taken. In the analytical solution given by equation (4.59), the first 15 odd (i.e. symmetric) modes were used. The numerical plucked string model is solved for $N = 2,\ 10,\ 20,\ 40,$ and 80.

Figure 4.6(a) shows the variation of the amplitude of the mid-point of the string as a function of time, obtained both analytically and numerically. Figure 4.6(b) shows the corresponding frequency contents obtained from a fast Fourier transformation (FFT) analysis. The tension fluctuations of the last tether element, T_N, is a function of the last tether angle, θ_N, for both elastic and rigid tether models. Hence, θ_N is an ideal candidate for convergence studies. The fundamental frequency predicted by FFT analysis of θ_N showed that it converged to 0.40 for a $N = 40$ and remains unchanged for further values of N while analytical results predicted 0.48 as shown in Figure 4.6(b). However, since $N = 20$ predicted a fundamental frequency of 0.39 which is close to 0.40, considering the computational expense and accuracy, $N = 20$ is considered for further studies. The results remained the same irrespective of varying the stiffness of the tether for different values of E and A.

4.4 Results and discussions

We present numerical results for two different systems: (i) a tethered autogyro, which we call an APS (aerostatic power system), and (ii) a tethered kite power system (KPS). It is assumed that the tether movement is not affecting the aerodynamics of either the autogyro or the kite. The APS and KPS considered in this work are capable of producing 300 kW and 13 kW, respectively.

4.4.1 Numerical results for the APS

Table 4.3 gives the design parameters of the APS. The thrust calculated from the unsteady blade element momentum (BEM) model (see Chapter 3) is used as the force applied at the farthest end of the tether. See Figures 4.7(a) and 4.7(b) for the variation of the thrust and the corresponding nominal power output of the APS over a cycle. Since the aerodynamic model for APS does not account for cyclic pitch or other corrections for smoothing the thrust and power outputs, they vary cyclically, as shown in Figure 4.7.

Figures 4.8(a) and 4.8(b) show the variation of T_N and θ_N as a function of time, respectively, obtained by the elastic and rigid tether models. Note that in the case of elastic tether model the time history of T_N also includes the longitudinal dynamics, i.e. s_N, in addition to θ_N. Thus, Figure 4.8 also represents the dynamic response of the two generalised coordinates of $\mathbb{L}_N$.

Table 4.3: Tethered APS parameters

L_t	1000 m	d_t	7.5 mm
k_{eq}	4600 N/m	m_t	42 kg
$\beta = 90° - i$	50°	m_k	1350 kg
$V(z_r = 10m)$	6 m/s	α	0.2

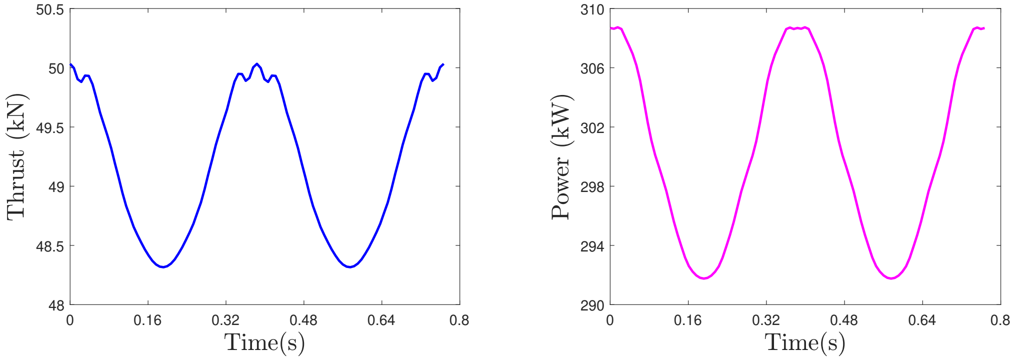

(a) (b)

Figure 4.7: Plots showing the variation of (a) thrust output of APS in (kN), and (b) power output in (kW) as predicted by the unsteady blade element momentum theory.

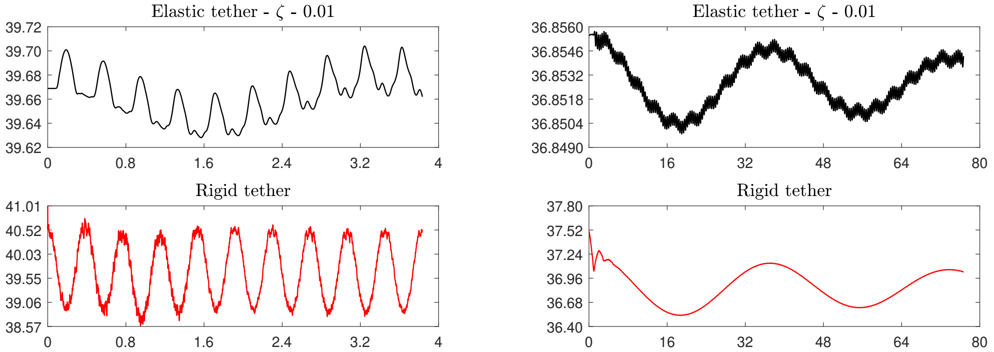

(a) (b)

Figure 4.8: Plots showing the variation of (a) tension in the last tether element, T_N (kN), and (b) tether angle close to ground θ_N in $(^\circ)$ as predicted by the numerical elastic tether model with $\zeta = 0.01$ and rigid tether model for inputs from APS shown in Figure (4.7).

Figure 4.8(a) shows that the rigid tether model predicts slightly higher values of T_N. This could be attributed to the additional degree of freedom of the elastic tether model. While the tension predicted by the rigid tether model fluctuates approximately by 1.5 kN which is in a similar range of the thrust fluctuation, the tension output from the elastic tether model fluctuates approximately by 0.1 kN. As seen, the tension predicted by the elastic tether model is out of phase with respect to the thrust input while the rigid tether model predicts an in-phase response.

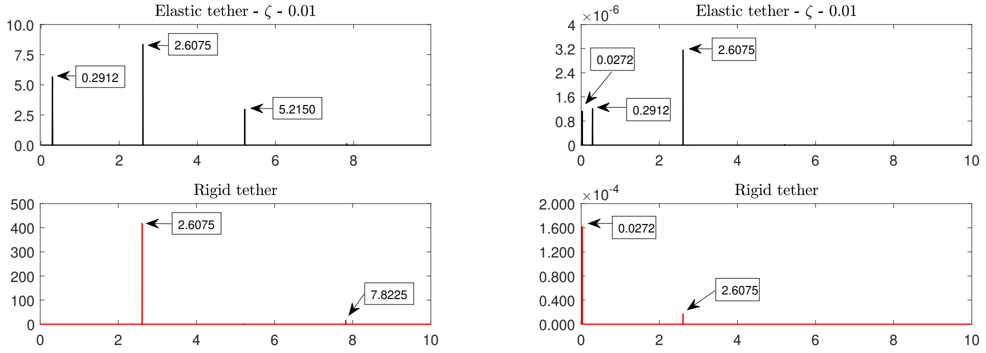

(a) (b)

Figure 4.9: Plots showing FFT results based on (a) Tension in the last tether element, T_N and (b) Tether angle close to ground θ_N as predicted by the numerical elastic tether model with $\zeta = 0.01$ and rigid tether model for inputs from APS shown in Figure (4.7).

Figure 4.8(b) shows that, except for the high frequency contribution superimposed on the lower frequency wave, the responses predicted by the rigid and elastic tether models are reasonably similar. While the response of θ_N from the rigid tether fluctuates approximately by 0.5°, the response from the elastic tether varies by 0.01° only.

Figure 4.9(a) shows the results from FFT analysis of T_N and Figure 4.9(b) shows that of θ_N obtained from the rigid and elastic tether models. As seen from Figure 4.9(a), both tether models predict the same fundamental frequency, i.e. 2.6075 Hz, which is equal to the frequency of the thrust and is the expected behaviour of a system undergoing forced vibrations. The elastic tether model also predicts a lower frequency 0.2912 Hz whose presence is also evident in Figure 4.9(a). This lower frequency appears to be a subharmonic frequency, i.e. $0.2912/2.6075 \approx 1/9$. The higher frequency 5.2150 Hz seen from the FFT results of the elastic tether model also corresponds to a superharmonic of the fundamental frequency. Similarly is 7.8225 Hz, which is observed in the FFT results of the rigid tether model. As seen from the FFT analysis of θ_N presented in 4.9(b), the elastic tether model still predicts the frequency of the thrust input, 2.6075 Hz, as the fundamental frequency while the rigid tether model predicts 0.0272 Hz as the fundamental frequency, which is evident from the response shown in Figure 4.8(b).

4.4.2 Numerical results for the KPS

The thrust and power cycles shown in Figure 4.10(a), the tether length and reel-in/reel-out velocity variation shown in Figure 4.10(b) and the parameters mentioned in Table 4.4 are the inputs for the tethered KPS. The thrust and power cycles shown are hypothetical and not based on an aerodynamic model for the KPS.

The time history of T_N is shown in Figure 4.11(a) and that of θ_N is shown in Figure 4.11(b), obtained from the elastic and rigid tether models. Unlike the response from the APS model, the tension predicted by both tether models are in phase with the external force input. As seen, tension fluctuations due to sudden changes in acceleration caused by

Table 4.4: Tethered KPS parameters

L_t	200 m	d_t	1.8 mm
k_{eq}	1425 N/m	m_t	0.5 kg
β	30°	m_k	20 kg
$V(z_r = 10m)$	6 m/s	α	0.2

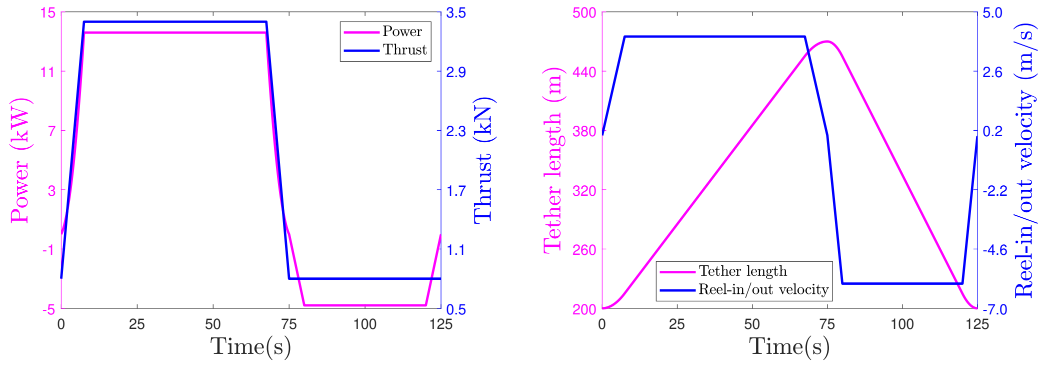

(a) (b)

Figure 4.10: Plots showing the variation of (a) Power (kW) and Thrust (kN), and (b) Tether length (m) and reel-in/reel-out velocity (m/s) used as inputs in tethered KPS.

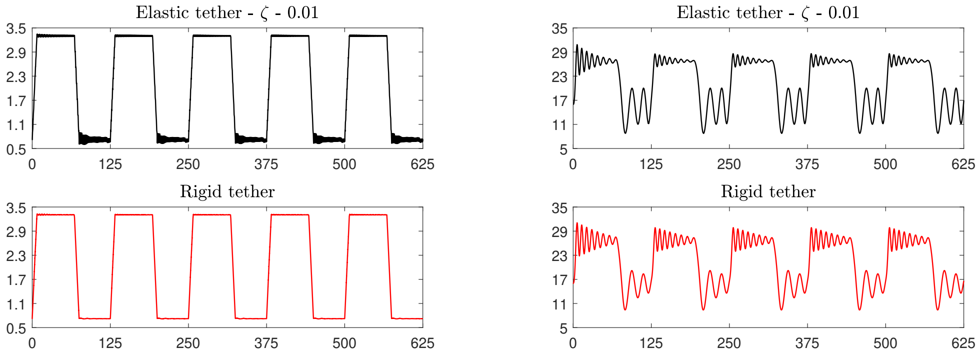

(a) (b)

Figure 4.11: Plots showing the variation of (a) Tension in the last tether element, T_N in (kN), and (b) Tether angle close to ground θ_N in $(^\circ)$ as predicted by the elastic tether model with $\zeta = 0.01$ and rigid tether model for inputs for KPS as shown in Figure (4.10).

the reel-in/reel-out are captured by the elastic but not by the rigid tether model. These fluctuations tend to decrease in amplitude over the period mainly because of the structural damping. The capability of predicting these high frequency fluctuations is crucial for tether life estimation studies as well as for designing proper control systems for the winch system on the ground. It appears that since the weight of the airborne module of the KPS is smaller compared to the APS, the value of tension predicted by the tether models closely follows that of the external force input. It is observed from Figure 4.11(b) that θ_N values predicted by the two tether models are in phase and their mean values are approximately the same. Interestingly, when the tether is under a low tension, the elastic tether model predicts larger amplitude oscillations compared to the rigid tether model whereas the opposite happens when the tether is pulled by a high force. This means that although the rigid tether model provides a conservative estimation of oscillations at high tensions, it underestimates those when the tension is low.

Figure 4.12 shows the variation of actual power available at the ground as predicted by the elastic and rigid tether models. Due to the proportionality of the power output to

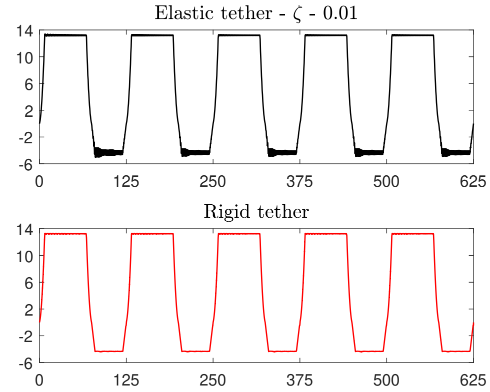

Figure 4.12: Figure showing the variation of Power in (kW) predicted as the output of the KPS based on the actual variation of tension shown in Figure (4.11a) .

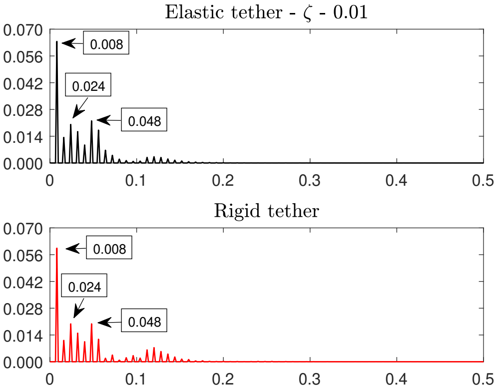

Figure 4.13: Figure showing FFT results based on tether angle close to ground, θ_N as predicted by the elastic tether model with $\zeta = 0.01$ and rigid tether model for inputs for KPS as shown in Figure(4.10).

the reel-in/reel-out velocity, its trend is similar to that of the reel-in/reel-out velocity. The fluctuations of tension from the elastic tether model are reflected in its power output while the rigid tether lacks this capability.

Figure 4.13 shows the FFT of T_N obtained from the elastic and rigid tether models. Both tether models predict the same fundamental frequency of 0.008 Hz which is the same as the frequency of the external force. Even though both tether models have captured the predominant frequencies (which are superharmonics of the fundamental frequency), the rigid tether model fails to capture the high-frequency oscillations observed in the tension fluctuations. However, this observation is not very obvious in Figure 4.13 because of the scale of graph but can easily seen in Figure 4.11(a).

4.5 Conclusion

This research work presents the numerical modelling and analysis of the dynamics of the tethered AWE systems in two dimensions. The modelling was done in the Lagrangian framework using generalised coordinates. The lumped mass model facilitated faster solutions and adding or removing sophisticated aspects to the model. The model can account for fixed and variable tether length, thus proving its merit in a variety of other applications like kites/balloons/drones that are statically suspended or reel-in/reel-out. The airborne module was modelled as a point mass, reducing its degrees of freedom into two. The results presented from the study are only for one-way coupling implying that the aerodynamics of the airborne module remains unaffected by the tether dynamics. A continuous system can be approached by increasing N at the expense of computational requirements. The rigid tether model had N degrees of freedom while the elastic tether model had $2N$. The mechanics of the tether models was successfully verified against the analytical solutions for the equilibrium of a catenary cable and the dynamics of a plucked string.

The aerodynamic force from the airborne module was treated as an input in the tethered APS. On the other hand, the inputs for tethered KPS were the external force/thrust, reel-in/reel-out velocity and the length variation. The reel-in/reel-out algorithm implemented followed a quasi-static approach as it assumed a new tether of different lengths each time. Hence, the kinetic energy of the tether predicted is less than the true value. This difference is small and assumed to not had affected the overall dynamics.

The tension at the ground and power output were in phase with the aerodynamic force input and closely followed it for rigid and elastic tether models of the KPS and the rigid tether model of the APS. However, the tension at the ground predicted by the elastic tether model of APS was out of phase with that of the thrust input and did not fluctuate as much as the input thrust. The elastic tether model could predict the high-frequency fluctuations in tension due to reel-in/reel-out for the KPS but the rigid tether model failed to. For the elastic tether, tension incorporated the longitudinal displacement of the tether element. A step change in thrust would introduce infinite tension in the tether.

The tether angle of the last element predicted by either model was in phase. In the case of the tethered APS, the rigid tether model predicted a slightly higher value of tether angle and its variation, when compared to the elastic model which predicted a negligibly small variation of the angle. Even though the response for the first cycle showed similar amplitudes predicted by both models in KPS, higher damping was observed for the tether angle in the elastic model. The elastic model showed high-frequency oscillations which were not captured by the rigid model.

Since the results presented are for one-way coupling, the tether dynamics was not affecting the power output of APS. However, since tension times the reel-in/reel-out velocity is the power in the KPS cycle, its power cycle closely followed the trend of reel-in/reel-out velocity while including the fluctuations in tension.

Fourier transform of tension response and the response of the last tether angle gave the frequency distribution from elastic and rigid tether models for APS. For the FFT of tension variation, both models predicted the same fundamental frequency which is the frequency of external aerodynamic force input. Elastic tether predicted frequencies higher and lower than the fundamental frequency. For the FFT of tether angle, the elastic model predicted the same frequency as the thrust input as the fundamental frequency while the rigid tether model did not. The fundamental frequency and the harmonics predicted by the Fourier transform of tension in the last tether element were the same in both tether models for KPS. Higher frequencies were observed in the response from the elastic tether models for both APS and KPS.

Future works may include the extension of the tether dynamics formulation to three dimensions, the inclusion of a 3-DOF or a 6-DOF flight dynamic model for the flying airborne module, the inclusion of a dynamic model for the ground station, and adopting of a dynamic reel-in/reel-out algorithm, among others. These extensions will permit fully-coupled simulations of the dynamics of more promising AWE systems like crosswind kite power systems.

Chapter 5

Conclusion and future work

The idea of harvesting wind energy from high altitudes using tethered airborne modules constitutes the domain of airborne wind energy (AWE) and such systems are called airborne wind energy systems (AWESs). AWESs typically consist of a tether connecting the airborne module to the ground. This research work was focused on three of these systems: (i) crosswind kite power system (CKPS), (ii) aerostatic power system (APS), and (iii) kite power system (KPS). The CKPS consists of a kite harvesting wind energy through crosswind motion and is capable of on-board generation or ground-based generation; the APS comprises an autogyro generating electricity on-board via windmilling, and the KPS contains a traction kite generating electricity at the ground by periodically reeling in and out. In this research work, the aerodynamic and dynamic modelling and analysis of the above-mentioned systems were presented. Two steady-state aerodynamic theories were developed for CKPSs in Chapter 2, a quasi-steady aerodynamic theory was developed for the APS in Chapter 3, and the rigid and elastic tether models developed for statically suspended systems and systems involving reel-in/reel-out were presented in Chapter 4.

Chapter 2: Generalized aerodynamic models for crosswind kite power systems

Chapter 2 presents two steady-state aerodynamic models based on Glauert's equations for CKPSs executing circular trajectories. Aerodynamic model 1 assumes uniform inflow and can be used only for kites in pumping/lift mode; however, aerodynamic model 2 is capable of non-uniform inflow considerations and in addition to the lift mode, it can predict the performance of kites in drag mode or a combination of both. Unlike the existing literature, the effects of incidence angle and side-slip angle and tether drag were included in the formulation of the induction factor and power coefficient. Performance variables of the kite like coefficient of power, reel-out ratio and induction factor were predicted using predefined aerodynamic coefficients, and they show a different trend than when predicted with airfoil data for a chosen airfoil. For example, the former model predicted a decreasing induction factor with reel-out ratio while the latter predicted an increasing trend. The choice of type of airfoil affects the performance of the kite but does not make a difference in the trends of performance coefficients. In general, the analysis suggested that a larger swept area for the kite means more wind power produced and less induction. The inclination of the rotor plane to the wind flow reduces the power output and the value of optimum reel-out ratio. Assuming the operational parameters remain the same, the analysis suggested that the drag mode or hybrid lift-drag mode kite can harvest more wind energy than the lift-mode kite. Even though this is an important finding, a system-level study is required to validate the finding. Results from aerodynamic model 2 using corrected wing data were found to be in good agreement with computational fluid dynamics (CFD) results.

Chapter 3: Quasi-steady aerodynamic model of an aerostatic power system

Chapter 3 presents the aerodynamic modelling of an APS by means of the quasi-steady BEM theory. The induced velocity and angle of attack are found by equating forces predicted by momentum and blade element theory separately. This model is more accurate than the time-averaged models and gives solutions faster than the dynamic models, which make it ideal for coupling with the tether model. Like other BEM models, the quality of the results is very sensitive to the input aerodynamic data. The performance parameters from each blade (e.g., thrust and power) have a phase equal to the angle between the blades. The maximum thrust from blade 1 is observed at an azimuth angle of 45° and the lowest at 275°. The angle of attack, inflow angle, coefficient of lift and coefficient of drag of any airfoil are in phase and is at a 180° phase difference with the thrust and power from the respective blade. The inclination of the rotor to the wind reduces its performance. The aerodynamic model was validated against experimental data on a yawed wind turbine and an autogyro rotor.

Chapter 4: Dynamics of tethered airborne wind energy systems

Chapter 4 presents the mathematical modelling and analysis of the dynamics of a tethered APS and KPS. An inelastic rigid tether model and an elastic tether model were developed following the lumped mass model approach. The tether dynamics and the aerodynamics of the airborne module were one-way (or weakly) coupled. The reel-in/reel-out was implemented by dynamically changing the tether element length. The kinetic energy of the tether predicted this way is slightly less than the true value. However, this method accurately captures the kinetic energy of the airborne module and since the mass of the airborne module is considerably larger than the tether, the numerical error caused by the kinetic energy deficit can be neglected. The model follows general characteristics of a forced oscillation; for example, tension at the ground is in phase with that of the aerodynamic force input at the end point of the tether. The drag caused by the motion of tether in air is observed to dampen the high-frequency oscillations in the system. The equations of motion in the elastic tether model have two different time scales associated with longitudinal and transverse waves, resulting in a numerically stiffer problem than the rigid tether model with only transverse waves. The rigid tether model captures the flexible effects like sagging but does not take comparatively high-frequency longitudinal oscillations resulting from elasticity into account. This, however, results in faster numerical solutions. The tether models were verified statically and dynamically, using the analytical solution of a hanging catenary and that of a vibrating plucked string, respectively. Since the the tether models developed in this research work can handle tethers with dynamically changing lengths, their worthiness extends to kites/balloons/drones that are statically suspended or do reel-in/reel-out.

Future works

The models and tools developed in this thesis can further be improved in terms of accuracy and completeness. More extensive verification/validation studies can also be performed. The following actions are suggested for future studies:

- To perform verification of the steady-state aerodynamic models presented in Chapter 2, using CFD simulations that incorporate inclined rotor planes and wind shear
- To conduct a system-level study to determine the potential of various power generation

modes

- To develop an unsteady version of the BEM model presented in Chapter 3, by incorporating a dynamic inflow model and a dynamic stall model for rapidly changing angles of attack
- To include gust and turbulence models into the aerodynamic model of Chapter 3, which will help in obtaining more realistic values of power output
- To extend the tether models presented in Chapter 4 to three dimensions and to include a flight dynamic model (for the airborne module) for real-world applications
- To incorporate the ground station dynamics and dynamic reel-in/reel-out models to provide much more accurate solutions for AWESs like CKPSs

References

[1] M. Kheiri, V. S. Nasrabad, and F. Bourgault, “A new perspective on the aerodynamic performance and power limit of crosswind kite systems,” *Journal of Wind Engineering and Industrial Aerodynamics*, vol. 190, pp. 190–199, 2019.

[2] “Makani - x, the moonshot factory,” https://x.company/projects/makani, accessed: 2022-10-30.

[3] “Nordics’ first airborne wind energy farm on track ’for 2021’ after takeover,” https://www.rechargenews.com/wind/nordics-first-airborne-wind-energy-farm-on-track-for-2021-after-takeover/2-1-764097, accessed: 2022-10-30.

[4] “Sky windpower,” https://www.skywindpower.com, accessed: 2022-10-30.

[5] A. Gessow and A. D. Crim, “An extension of lifting rotor theory to cover operation at large angles of attack and high inflow conditions,” Tech. Rep., 1952.

[6] A. Gessow and G. C. Myers, *Aerodynamics of the Helicopter.* Burns & Oates, 1952.

[7] R. Schmehl, Ed., *Airborne Wind Energy.* Singapore: Springer, 2018.

[8] M. Kheiri, S. Victor, and F. Bourgault, “Advances in aerodynamic modelling of crosswind kite power systems,” in *Book of Abstracts of the 8th Airborne Wind Energy Conference (AWEC) 2019, Glasgow, UK, October 15-16*, 2019.

[9] M. Bastankhah and F. Porté-Agel, “Experimental and theoretical study of wind turbine wakes in yawed conditions,” *Journal of Fluid Mechanics*, vol. 806, pp. 506–541, 2016.

[10] M. L. Loyd, “Crosswind kite power,” *Journal of Energy (AIAA)*, vol. 4, no. 3, pp. 106–111, 1980, article No. 80-4075.

[11] M. Kheiri, “Airborne wind energy: A game changer in wind energy,” *Feature Article in the Canadian Society for Mechanical Engineering (CSME) Bulletin, Special Issue on Energy, Spring 2019*, 2019.

[12] P. Warnke, K. Cuhls, U. Schmoch, L. Daniel, L. Andreescu, B. Dragomir, R. Gheorghiu, C. Baboschi, A. Curaj, M. Parkkinen, and O. Kuusi, “100 Radical Innovation Breakthroughs for the Future, Directorate-General for Research and Innovation, Luxembourg: Publications Office of the European Union,” Tech. Rep., 2019.

[13] M. Diehl, “Airborne wind energy: Basic concepts and physical foundations,” in *Airborne wind energy*, 2013, pp. 3–22.

[14] European Commission, “Study on challenges in the commercialisation of airborne wind energy systems, Directorate-General for Research and Innovation, Luxembourg: Publications Office of the European Union,” Tech. Rep., 2018.

[15] E. Lunney, M. Ban, N. Duic, and A. Foley, “A state-of-the-art review and feasibility analysis of high altitude wind power in northern ireland,” *Renewable and Sustainable Energy Reviews*, vol. 68, pp. 899–911, 2017.

[16] A. Cherubini, A. Papini, R. Vertechy, and M. Fontana, “Airborne wind energy systems: A review of the technologies,” *Renewable and Sustainable Energy Reviews*, vol. 51, pp. 1461–1476, 2015.

[17] "A new wind blowing in the wind energy industry," https://www.pv.eu/articles/a-new-wind-blowing-in-the-wind-energy-industry/, accessed: 2022-12-02.

[18] M. De Lellis, R. Reginatto, R. Saraiva, and A. Trofino, "The Betz limit applied to airborne wind energy," *Renewable Energy*, vol. 127, pp. 32–40, 2018.

[19] B. Roberts and J. Blackler, "Various systems for generation of electricity using upper atmospheric winds," in *2nd Wind Energy Innovation Systems Conf., Solar Energy Res. Institute, Colorado Springs*, 1980, pp. 67–80.

[20] A. J. Khoei, "The optimum twist for windmilling operation of a tethered rotorcraft," 1993.

[21] D. Rancourt, F. Bolduc-Teasdale, E. D. Bouchard, M. J. Anderson, and D. N. Mavris, "Design space exploration of gyrocopter-type airborne wind turbines," *Wind Energy*, vol. 19, pp. 895–909, 5 2016.

[22] A. Walsh and J. R. Forbes, "Modeling and control of a wind energy harvesting kite with flexible cables," in *2015 American Control Conference (ACC)*. IEEE, 2015, pp. 2383–2388.

[23] N. Zero, "Energy high in the sky: expert perspectives on airborne wind energy systems," *Mason Inman, editor*, 2012.

[24] P. Williams, B. Lansdorp, and W. Ockesl, "Optimal crosswind towing and power generation with tethered kites," *Journal of Guidance, Control, and Dynamics*, vol. 31, no. 1, pp. 81–93, 2008.

[25] I. Argatov and R. Silvennoinen, "Energy conversion efficiency of the pumping kite wind generator," *Renewable Energy*, vol. 35, no. 5, pp. 1052–1060, 2010.

[26] L. Fagiano, A. U. Zgraggen, M. Morari, and M. Khammash, “Automatic crosswind flight of tethered wings for airborne wind energy: Modeling, control design, and experimental results,” *IEEE Transactions on Control Systems Technology*, vol. 22, no. 4, pp. 1433–1447, 2013.

[27] M. Erhard and H. Strauch, “Flight control of tethered kites in autonomous pumping cycles for airborne wind energy,” *Control Engineering Practice*, vol. 40, pp. 13–26, 2015.

[28] S. Costello, G. François, and D. Bonvin, “Crosswind kite control–a benchmark problem for advanced control and dynamic optimization,” *European Journal of Control*, vol. 35, pp. 1–10, 2017.

[29] G. Sánchez-Arriaga, A. Pastor-Rodríguez, M. Sanjurjo-Rivo, and R. Schmehl, “A lagrangian flight simulator for airborne wind energy systems,” *Applied Mathematical Modelling*, vol. 69, pp. 665–684, 2019.

[30] M. Kheiri, F. Bourgault, V. S. Nasrabad, and S. Victor, “On the aerodynamic performance of crosswind kite power systems,” *Journal of Wind Engineering and Industrial Aerodynamics*, vol. 181, pp. 1–13, 2018.

[31] M. Zanon, S. Gros, J. Meyers, and M. Diehl, “Airborne wind energy: Airfoil-airmass interaction,” *IFAC Proceedings Volumes*, vol. 47, no. 3, pp. 5814–5819, 2014.

[32] R. Leuthold, S. Gros, and M. Diehl, “Induction in optimal control of multiple-kite airborne wind energy systems,” *IFAC-PapersOnLine*, vol. 50, no. 1, pp. 153–158, 2017.

[33] T. Haas, J. De Schutter, M. Diehl, and J. Meyers, “Wake characteristics of pumping mode airborne wind energy systems,” in *Journal of Physics: Conference Series*, vol. 1256, no. 1. IOP Publishing, 2019, p. 012016.

[34] R. Leuthold, C. Crawford, S. Gros, and M. Diehl, "Engineering wake induction model for axisymmetric multi-kite systems," in *Journal of Physics: Conference Series*, vol. 1256, no. 1. IOP Publishing, 2019, p. 012009.

[35] J.-L. Pfister and F. Blondel, "Comparing blade-element theory and vortex computations intended for modelling of yaw aerodynamics of a tethered rotorcraft," in *Journal of Physics: Conference Series*, vol. 1618, no. 3. IOP Publishing, 2020, p. 032012.

[36] M. Gaunaa, A. M. Forsting, and F. Trevisi, "An engineering model for the induction of crosswind kite power systems," in *Journal of Physics: Conference Series*, vol. 1618, no. 3. IOP Publishing, 2020, p. 032010.

[37] T. Haas and J. Meyers, "Comparison study between wind turbine and power kite wakes," in *Journal of Physics: Conference Series*, vol. 854, no. 1. IOP Publishing, 2017, p. 012019.

[38] M. Kheiri, V. S. Nasrabad, S. Victor, and F. Bourgault, "A wake model for crosswind kite systems," in *Book of Abstracts of Airborne Wind Energy Conference (AWEC) 2017, Germany, October 5-6*, 2017b.

[39] M. Kheiri, S. Victor, S. Rangriz, M. M. Karakouzian, and F. Bourgault, "Aerodynamic performance and wake flow of crosswind kite power systems," *Energies*, vol. 15, no. 7, p. 2449, 2022.

[40] T. Haas, J. De Schutter, M. Diehl, and J. Meyers, "Large-eddy simulation of airborne wind energy farms," *Wind Energy Science*, vol. 7, no. 3, pp. 1093–1135, 2022.

[41] S. Kaufman-Martin, N. Naclerio, P. May, and P. Luzzatto-Fegiz, "An entrainment-based model for annular wakes, with applications to airborne wind energy," *Wind Energy*, vol. 25, no. 3, pp. 419–431, 2022.

[42] M. M. Karakouzian, M. Kheiri, and F. Bourgault, “A survey of two analytical wake models for crosswind kite power systems,” *Physics of Fluids*, vol. 34, no. 9, p. 097111, 2022.

[43] B. W. Roberts, D. H. Shepard, K. Caldeira, M. E. Cannon, D. G. Eccles, A. J. Grenier, and J. F. Freidin, “Harnessing high-altitude wind power,” *IEEE Transactions on Energy Conversion*, vol. 22, no. 1, pp. 136–144, 2007.

[44] X. Rong, D. Peters, and Z. Fei, “Optimum pitch settings and rpm for tethered, yawed wind turbines,” in *50th AIAA Aerospace Sciences Meeting including the New Horizons Forum and Aerospace Exposition*, 2012, p. 1071.

[45] M. Zanon, S. Gros, J. Andersson, and M. Diehl, “Airborne wind energy based on dual airfoils,” *IEEE Transactions on Control Systems Technology*, vol. 21, no. 4, pp. 1215–1222, 2013.

[46] M. Milutinović, N. Kranjčević, and J. Deur, “Multi-mass dynamic model of a variable-length tether used in a high altitude wind energy system,” *Energy conversion and management*, vol. 87, pp. 1141–1150, 2014.

[47] U. Fechner, R. van der Vlugt, E. Schreuder, and R. Schmehl, “Dynamic model of a pumping kite power system,” *Renewable Energy*, vol. 83, pp. 705–716, 2015.

[48] P. Williams, “Dynamic multibody modeling for tethered space elevators,” *Acta Astronautica*, vol. 65, no. 3-4, pp. 399–422, 2009.

[49] S. Dunker, “Tether and bridle line drag in airborne wind energy applications,” in *Airborne Wind Energy*. Springer, 2018, pp. 29–56.

[50] P. Williams, B. Lansdorp, and W. Ockesl, “Modeling and control of a kite on a variable length flexible inelastic tether,” *AIAA Modeling and Simulation Technologies Conference and Exhibit*, 2007.

[51] U. Fechner, “A methodology for the design of kite-power control systems,” *Unpublished PhD Thesis, Delft University of Technology, Delft, the Netherlands*, 2016.

[52] A. Pastor-Rodríguez, G. Sanchez-Arriaga, and M. Sanjurjo-Rivo, “Modeling and stability analysis of tethered kites at high altitudes,” *Journal of Guidance, Control, and Dynamics*, vol. 40, no. 8, pp. 1892–1901, 2017.

[53] G. Sánchez-Arriaga, J. A. Serrano-Iglesias, R. Leuthold, and M. Diehl, “Modeling and natural mode analysis of tethered multi-aircraft systems,” *Journal of Guidance, Control, and Dynamics*, vol. 44, no. 6, pp. 1199–1210, 2021.

[54] T. Burton, N. Jenkins, D. Sharpe, and E. Bossanyi, *Wind Energy Handbook.* John Wiley & Sons, 2011.

[55] J. N. Sørensen, *General momentum theory for horizontal axis wind turbines.* Springer, 2016, vol. 4.

[56] S. Gupta and J. Leishman, “Comparison of momentum and vortex methods for the aerodynamic analysis of wind turbines,” in *43rd AIAA aerospace sciences meeting and exhibit*, 2005, p. 594.

[57] D. A. Peters and X. Rong, “Optimum operational parameters for yawed wind turbines,” *International Journal of Aerospace Engineering*, vol. 2011, 2011.

[58] J. Morote, “Angle of attack distribution on wind turbines in yawed flow,” *Wind Energy*, vol. 19, no. 4, pp. 681–702, 2016.

[59] S. Aubrun, S. Loyer, P. Hancock, and P. Hayden, “Wind turbine wake properties: Comparison between a non-rotating simplified wind turbine model and a rotating model,” *Journal of Wind Engineering and Industrial Aerodynamics*, vol. 120, pp. 1–8, 2013.

[60] L. E. M. Lignarolo, D. Ragni, C. J. S. Ferreira, and G. J. W. Van Bussel, “Kinetic energy entrainment in wind turbine and actuator disc wakes: an experimental analysis,” in *Journal of Physics: Conference Series*, vol. 524, no. 1. IOP Publishing, 2014, p. 012163.

[61] W. Yu, V. W. Hong, C. Ferreira, and G. A. M. van Kuik, “Experimental analysis on the dynamic wake of an actuator disc undergoing transient loads,” *Experiments in Fluids*, vol. 58, no. 10, pp. 1–15, 2017.

[62] D. Micallef, C. Ferreira, I. Herráez, L. Höning, W. Yu, and H. Capdevila, “Assessment of actuator disc models in predicting radial flow and wake expansion,” *Journal of Wind Engineering and Industrial Aerodynamics*, vol. 207, p. 104396, 2020.

[63] H. Glauert, “A General Theory of the Autogyro,” *British ARC, No. 1111*, 1926.

[64] R. E. Wilson and P. Lissaman, *Applied Aerodynamics of Wind Power Machines.* Corvallis, Or., Oregon State University, 1974.

[65] I. Argatov, P. Rautakorpi, and R. Silvennoinen, “Estimation of the mechanical energy output of the kite wind generator,” *Renewable Energy*, vol. 34, no. 6, pp. 1525–1532, 2009.

[66] F. Bauer, R. M. Kennel, C. M. Hackl, F. Campagnolo, M. Patt, and R. Schmehl, “Drag power kite with very high lift coefficient,” *Renewable Energy*, vol. 118, pp. 290–305, 2018.

[67] S. F. Hoerner, *Fluid Dynamic Drag*, 2nd ed. Brick Town, NJ: Hoerner Fluid Dynamics, 1965.

[68] J. D. Anderson, *Fundamentals of Aerodynamics*, 6th ed. McGraw-Hill Education, 2017.

[69] P. Echeverri, T. Fricke, G. Homsy, and N. Tucker, *The Energy Kite: Selected Results from the Design, Development, and Testing of Makani's Airborne Wind Turbines, Part I of III.* Makani Technologies LLC, 2020.

[70] A. Silverstein, "Scale Effect on Clark Y Airfoil Characteristics from NACA Full-scale Wind-tunnel Tests." vol. NACA Report No. 502, 1935.

[71] M. S. Selig, J. J. Guglielmo, A. P. Broeren, and P. Giguére, *Summary of Low Speed Airfoil Data.* Virginia: SoarTech Publications, 1995.

[72] F. Gohl and R. H. Luchsinger, "Simulation based wing design for kite power," in *Airborne Wind Energy.* Springer, 2013, pp. 325–338.

[73] R. L. Bisplinghoff, H. Ashley, and R. L. Halfman, *Aeroelasticity.* New York: Dover Publications, Inc., 1996.

[74] D. H. Hodges and G. A. Pierce, *Introduction to Structural Dynamics and Aeroelasticity*, 2nd ed. Cambridge University Press, 2011.

[75] I. Paraschivoiu, P. Desy, and C. Masson, "Blade tip, finite aspect ratio, and dynamic stall effects on the Darrieus rotor," *Journal of Propulsion and Power*, vol. 4, no. 1, pp. 73–80, 1988.

[76] L. Prandtl and A. Betz, *Vier abhandlungen zur hydrodynamik und aerodynamik.* Kaiser Wilhelm-Institut für Strömungsforschung, 1927.

[77] S. Goldstein, "On the vortex theory of screw propellers," *Proceedings of the Royal Society of London. Series A*, vol. 123, no. 792, pp. 440–465, 1929.

[78] H. Glauert, "Airplane Propellers," in *Aerodynamic Theory.* Springer, 1935, pp. 169–360.

[79] W. Z. Shen, R. Mikkelsen, J. N. Sørensen, and C. Bak, "Tip loss corrections for wind turbine computations," *Wind Energy*, vol. 8, no. 4, pp. 457–475, 2005.

[80] H. Schaub and J. L. Junkins, *Analytical mechanics of space systems.* Aiaa, 2003.

[81] C. L. Archer, "An introduction to meteorology for airborne wind energy," in *Airborne wind energy.* Springer, 2013, pp. 81–94.

[82] M. Hansen, *Aerodynamics of wind turbines.* Earthscan, 2008.

[83] M. Lin and F. Porté-Agel, "Large-eddy simulation of yawed wind-turbine wakes: comparisons with wind tunnel measurements and analytical wake models," *Energies*, vol. 12, no. 23, p. 4574, 2019.

[84] M. Bastankhah and F. Porté-Agel, "A new miniature wind turbine for wind tunnel experiments. part i: Design and performance," *Energies*, vol. 10, no. 7, p. 908, 2017.

[85] T. Revaz, M. Lin, and F. Porté-Agel, "Aerodynamic data of wire-01 blade. available online: https: //zenodo.org/record/3460877.xdylmtk-uuk (accessed on 25 september 2019)," 2019.

[86] R. E. Sheldahl and P. C. Klimas, "Aerodynamic characteristics of seven symmetrical airfoil sections through 180-degree angle of attack for use in aerodynamic analysis of vertical axis wind turbines," Sandia National Labs., Albuquerque, NM (USA), Tech. Rep., 1981.

[87] S. S. Rao, *Mechanical Vibrations*, 6th ed. Pearson India education Services Pvt. Ltd, 2022.

[88] U. Ahrens, M. Diehl, and R. Schmehl, Eds., *Airborne Wind Energy.* Berlin: Springer, 2013.

[89] R. Marissen, "Design with ultra strong polyethylene fibers," *Materials Sciences and Applications*, vol. 02, pp. 319–330, 2011.

[90] J. Palm, G. M. Paredes, F. T. Pinto, and L. Bergdahl, "Simulation of mooring cable dynamics using a discontinuous galerkin method," 2013. [Online]. Available: www.chalmers.se

Appendix A

Alternative formulae

Consider the following definitions for the induction factor and crosswind speed ratio

$$\widetilde{a} = \frac{v}{V_\infty \sin i \cos\beta - V_d}, \quad \widetilde{\lambda}_r = \frac{\Omega r}{V_\infty \sin i \cos\beta - V_d}. \tag{A.1}$$

The time-averaged, local inflow angle ϕ may be written as

$$\tan\overline{\phi} = \frac{1 - \widetilde{a}}{\widetilde{\lambda}_r}. \tag{A.2}$$

The thrust acting on the swept area may be written as

$$T = \frac{1}{2}\rho_\infty A_s V_\infty^2 4\widetilde{a}(1 - \widetilde{a})(1 - e \sin i \cos\beta)(\sin i \cos\beta - e). \tag{A.3}$$

The equation for finding the induction factor may be obtained as

$$\frac{\widetilde{a}(1 - e \sin i \cos\beta)}{(1 - \widetilde{a})(\sin i \cos\beta - e)} = \frac{1}{4}\sigma C_L (\frac{C_L}{\widehat{C}_D})^2 [1 + (\frac{\widehat{C}_D}{C_L})^2]. \tag{A.4}$$

The equations for the swept- and kite-area-normalized power coefficients are written as

$$C_p^{(s)} = 4\widetilde{a}(1-\widetilde{a})e(\sin i\cos\beta - e)(1 - e\sin i\cos\beta), \tag{A.5}$$

$$C_p^{(k)} = C_L(\frac{C_L}{\widehat{C}_D})^2(1-\widetilde{a})^2 e(\sin i\cos\beta - e)^2, \tag{A.6}$$

respectively.

For the straight-downwind configuration with no side-slip (i.e. $i = 90^\circ$ and $\beta = 0^\circ$), equations (A.3) to (A.6) will reduce exactly to the equations given in [30].

Appendix B

Finding the time-averaged, local inflow angle $\overline{\phi}$

The local inflow angle ϕ can be averaged over a cycle (i.e. $0 \leq \psi \leq 2\pi$) as:

$$
\begin{aligned}
\overline{\phi} &= \frac{1}{2\pi}\int_0^{2\pi} \tan^{-1}(\frac{V_P}{V_T})\ \mathrm{d}\psi, \\
&= \frac{1}{2\pi}\int_0^{2\pi} \tan^{-1}\left(\frac{V_\infty \sin i \cos\beta - v - V_d}{r\Omega + V_\infty \cos i \cos\beta \sin\psi + V_\infty \sin\beta\cos\psi}\right) \mathrm{d}\psi, \\
&= \frac{1}{2\pi}\int_0^{2\pi} \tan^{-1}\left(\frac{\sin i \cos\beta - a - e}{\lambda_r + \cos i \cos\beta \sin\psi + \sin\beta\cos\psi}\right) \mathrm{d}\psi, \\
&= \frac{1}{2\pi}\int_0^{2\pi} \tan^{-1}\left(\frac{A}{1 + B\sin\psi + C\cos\psi}\right) \mathrm{d}\psi, \\
&= \frac{1}{2\pi}\int_0^{2\pi} \tan^{-1}\left(\frac{A}{1 + X}\right) \mathrm{d}\psi, \qquad \text{(B.1)}
\end{aligned}
$$

where the expressions for V_T and V_P were given in Section 2.2.2; also, $A = (\sin i \cos\beta - a - e)/\lambda_r$, $B = (\cos i \cos\beta)/\lambda_r$, $C = \sin\beta/\lambda_r$, and $X = B\sin\psi + C\cos\psi$.

Since in the present paper the incidence angle i and the side-slip angle β are assumed to be large and small, respectively, even for moderate values of λ_r, B, C and thus X are expected to be small, i.e. $B \sim \mathcal{O}(\epsilon)$, $C \sim \mathcal{O}(\epsilon)$, and $X \sim \mathcal{O}(\epsilon)$. Now, let us define f as $f(X) = \tan^{-1}(A/(1+X)))$. The first and second derivatives of f with respect to X may be obtained as

$$f'(X) = \frac{-A}{(1+X)^2 + A^2}, \; f''(X) = \frac{2A(1+X)}{\left[(1+X)^2 + A^2\right]^2}. \tag{B.2}$$

The Taylor's expansion of $f(X)$ can be written as:

$$\begin{aligned} f(X) &= f(0) + f'(0)X + f''(0)\frac{X^2}{2} + \mathcal{O}(\epsilon^3) \\ &= \tan^{-1} A - \frac{A}{1+A^2}X + \frac{2A}{(1+A^2)^2}\frac{X^2}{2} + \mathcal{O}(\epsilon^3). \end{aligned} \tag{B.3}$$

With this, equation (B.1) may be re-written as

$$\begin{aligned} \overline{\phi} &= \frac{1}{2\pi}\int_0^{2\pi} \left[\tan^{-1} A - \frac{AX}{1+A^2} + \frac{AX^2}{(1+A^2)^2}\right] \mathrm{d}\psi + \mathcal{O}(\epsilon^3) \\ &= \tan^{-1} A - \frac{1}{2\pi}\int_0^{2\pi} \frac{AX}{1+A^2}\, \mathrm{d}\psi + \frac{1}{2\pi}\int_0^{2\pi} \frac{AX^2}{(1+A^2)^2}\, \mathrm{d}\psi + \mathcal{O}(\epsilon^3), \\ &= \tan^{-1} A - \frac{A}{2\pi(1+A^2)}\int_0^{2\pi} (B\sin\psi + C\cos\psi)\, \mathrm{d}\psi \\ &+ \frac{A}{2\pi(1+A^2)^2}\int_0^{2\pi} (B^2\sin^2\psi + C^2\cos^2\psi + BC\sin 2\psi)\, \mathrm{d}\psi + \mathcal{O}(\epsilon^3). \end{aligned} \tag{B.4}$$

The first integral on the r.h.s. of equation (B.4) is zero considering the fact that $\int_0^{2\pi}\sin\psi\,\mathrm{d}\psi = \int_0^{2\pi}\cos\psi\,\mathrm{d}\psi = 0$; also, considering $\int_0^{2\pi}\sin^2\psi\,\mathrm{d}\psi = \int_0^{2\pi}\cos^2\psi\,\mathrm{d}\psi = \pi$, and $\int_0^{2\pi}\sin 2\psi\,\mathrm{d}\psi = 0$, the second integral reduces to $\pi(B^2 + C^2)$; thus,

$$\overline{\phi} = \tan^{-1} A + \frac{A(B^2 + C^2)}{2(1+A^2)^2} + \mathcal{O}(\epsilon^3). \tag{B.5}$$

Now, let us obtain the expression on the r.h.s correct to $\mathcal{O}(\epsilon)$ by neglecting all the terms of the order of $\mathcal{O}(\epsilon^2)$ and higher:

$$\overline{\phi} = \tan^{-1} A + \mathcal{O}(\epsilon^2), \tag{B.6}$$

which can be rewritten as

$$\tan \overline{\phi} = A = \frac{\sin i \cos \beta - a - e}{\lambda_r} + \mathcal{O}(\epsilon^2), \tag{B.7}$$

that is exactly the same expression given in equation (2.13).

Appendix C

Some details about the CFD results presented in Table 2.4 and Figure 2.13

The CFD simulation was performed using Ansys Fluent's (Academic 19.1) unsteady Reynolds-averaged Navier-Stokes (URANS) flow solver closed by the $k-\omega$ SST turbulence model [8]. The dimensional parameters of the crosswind kite system were: $\Omega = 0.738$ rad/s, $V_\infty = 12.5$ m/s, $R = (r_o + r_i)/2 = 123.3$ m (radius of gyration), $b = (r_o - r_i) = 53.94$ m (kite span), $c = 3.72$ m (chord length). The simulation was ran up to 51 cycles to ensure the wake flow is fully developed up to large downstream distances from the rotor. Each cycle of the kite rotation took almost 24 hours of CPU time on a cluster with 12 cores and 192 GB of RAM. The solution time step was considered to be equivalent to 1 degree of rotation (i.e. approximately 0.02 s). The simulation domain was $20 \times 9 \times 9$ Km ($\mathrm{L} \times \mathrm{W} \times \mathrm{H}$) in size, and the blockage ratio was 0.02%. A uniform spatio-temporal flow velocity of $V = (1 - 1/3) \times 12.5 = 8.33$ m/s with the turbulent intensity of 1% was imposed at the inlet (i.e. the velocity inlet condition); the rest of the boundary conditions were: zero gauge pressure at the outlet (i.e. the pressure outlet condition), symmetry over the top, bottom and sides of the domain, and no-slip over all faces of the kite. Also, the SIMPLE algorithm was used for pressure-velocity coupling.

Appendix D

Damping coefficient consideration

As per [87], the equivalent damping, c_{eq}, of N dampers of damping coefficients, $c_1, c_2, ..., c_N$ connected in series like in the numerical tether model is given by

$$\frac{1}{c_{eq}} = \frac{1}{c_1} + \frac{1}{c_2} + ... + \frac{1}{c_N}. \tag{D.1}$$

This equation which is also used in some of the literature on tether modelling suggests that the damping coefficient of each tether element is N times the damping coefficient of the whole tether, c_{eq}. However, equation (4.38) suggests that the damping coefficient of each tether element is in fact the same as that of the entire tether. This is because $k_i = Nk$ while $m_i = m/N$. This analysis agrees well with the notion that the damping is primarily dependent on the material properties. To overcome this dilemma, we performed some numerical analysis on the fundamental frequency and amplitudes of a plucked string, considering no damping, constant damping as N varies, and variable damping as N varies. The idea is that, as N is increased to sufficiently large numbers, the frequency and amplitudes of vibrations should converge to certain values. Also, for lightly damped systems, it is well-known that the damped frequency will be very close to the undamped fundamental frequency [87].

Comparing the fundamental frequencies and amplitudes from string vibrations for different scenarios of damping, the results for the constant damping case are closer to those for the undamped case. Hence, it was concluded that the damping coefficient is to be treated as a constant.